Title

Fission plasmas and their novel application to power producing nuclear reactors in space

Permalink

https://escholarship.org/uc/item/1x52n1gw

Author

Lo, Austin

Publication Date

2020

Peer reviewed|Thesis/dissertation

Fission plasmas and their novel application to power producing nuclear reactors in space

By

Austin Troy Lo

A dissertation submitted in partial satisfaction of

the requirements for the degree of

Doctor of Philosophy

in

Engineering – Nuclear Engineering

in the

Graduate Division

of the

University of California, Berkeley

Committee in charge:

Professor Lee Bernstein, Chair

Professor Massimiliano Fratoni

Professor Michael Lieberman

Fall 2020

Table of Contents

Acknowledgements

This body of work would not have been possible to produce without the inspiration and/or support from: Karl van Bibber, Executive Associate Dean of the College of Engineering, who was the first professor from UC Berkeley to identify a "strong fundamental science streak" in me and take me on as his graduate student...

Captain David E. Fowler, USN, who casted doubt on my ability to commit to any of my endeavors and relieved me from the Naval Nuclear Propulsion Officer training program...

Ian Hamilton, Founder and CEO of Atlas Energy Systems, who opened my eyes to novel ideas in thermionic energy conversion and reinvigorated my "strong fundamental science streak..."

Lee Bernstein, Associate Professor, who trusted my self guided path to producing the scholarly work contained in this thesis and mentored me to successfully completing my dissertation...

Michael Lieberman, Professor Emeritus, who fielded fruitful discussions on low temperature plasma physics...

Massimiliano "Max" Fratoni, Associate Professor, who provided guidance in the nuclear reactor core analysis of this work...

My Father, General Practitioner, whose genuine interest in his patients lead to making a connection with...

Frank Jamerson, Project Supervisor of the Investigations on the Direct Conversion of Nuclear Fission Energy to Electrical Energy in a Plasma Diode (1967), who actively stayed involved with my work and lead me to the original, half-century old "GM Study" papers– at 94 years of age...

Ned Rasor, CEO of Rasor Associates, Inc., who offered key insights into the BaO cathodes used in the "GM Study" and subsequent analysis – at 93 years of age...

Abstract

The specific power (W_e/kg) requirements for high powered space missions greater than $1MW_e$ present a significant design challenge to the nuclear engineering community. Energy conversion, and the temperature at which it occurs, is central to this problem and remains a limiting factor to realizing high specific power systems. This thesis investigates a static, in-core thermionic energy conversion (TEC) cycle that uses kinetic energy from fission fragments and their resulting high energy beta decay to produce both heat for thermionic emission and ionization of an interelectrode low temperature plasma. This novel plasma ionization scheme allows for dramatically increased device efficiency and loosened design constraints; both are needed for TEC to be competitive with the dynamic Brayton cycle – currently the only technology slated for high powered space missions. We develop an electrical power model, called the Heavy Ion Thermionic Energy Conversion (HITEC) model in order to investigate electrical power characteristics of both single cell and nuclear reactor scale devices in order to assess this reactor's performance metrics and its applicability to high powered space missions. HITEC was benchmarked against the only existing experimental data set from a de-classified joint research effort[14], and its power characteristics are in good agreement with this experimental data. The reactor scaling portion of HITEC was used to calculate the electrical performance of a $2.5MW_{th}$ nuclear reactor. Four separate cases were tested on a single core design: we found that in three of the four cases, the HITEC reactor exceeded NASA's specific power limits for the 1-10 MW_e power output range (> $60W_e$/kg). When auxiliary power was implemented for additional plasma ionization, the maximum specific power attained was 348 W_e/kg. This makes HITEC, an attractive static alternative to the dynamic Brayton cycle for power producing nuclear reactors applied to high power mission sets.

Chapter 1: Introduction

1.1 The Case for In-Core Thermionic Nuclear Power in Space

After a 50 year hiatus in the United States' efforts to deploy nuclear reactors in space the first successful space nuclear reactor ground test of this century came to fruition at the Nevada National Security Site (NNSS) on March 21, 2018. The reactor undergoing testing, known as the Kilopower Reactor Using Stirling TechnologY (KRUSTY), is a $4kW_{th}$ heat pipe reactor designed by Los Alamos National Laboratory [1] to be scaled within the $1-10kW_e$ range. The successful ground testing has solidified it as the reactor of choice for first generation space-based missions. These missions will include various orbital space flights starting as early as 2022 and eventually culminate in manned lunar and Martian surface missions, anticipated to come in the late 2020s and early 2030s, respectively. In the case of the latter surface missions, the current opinion is that $40kW_e$ [2] is the minimum power needed to support a crew of 7-9 meaning that multiple Kilopower systems would be required. Though using four Kilopower systems may seem reasonable in the near term, the power requirement to support more than 7-9 people on extraterrestrial bodies will be much higher: likely on the MW_e scale, rendering Kilopower systems inadequate for the task. It is therefore prudent for the space nuclear reactor community to begin turning some of its focus toward developing higher power reactor systems as they may pose design challenges that, if not resolved, will severely constrain our ability to pursue larger-scale space exploration.

KRUSTY's power class is the lowest of four in NASA's most recent Technology Roadmap: the other three classes mentioned are $10-100kW_e$, $1-10MW_e$, and $>10MW_e$. The principle delineation between the $1-10kW_e$ class and any of the higher classes is the required temperature for operation: the former may operate at nearly 1100K while the latter groups must operate at temperatures in excess of 1800K, which will be made apparent in the following discussion. Space missions are most economically sensitive to their launch costs. Since launch cost is based primarily on payload mass, the magnitude of electrical power production in space is fundamentally limited by its specific power (kW_e/kg). It would therefore be desirable, given a space power system, to maximize its electrical power output and while *simultaneously* minimizing its overall mass. Traditionally, total power output is increased by improving thermodynamic efficiency, which in turn requires maximizing ΔT since the Carnot efficiency is given by:

$$\eta = 1 - \frac{T_c}{T_h}$$

where T_h and T_c are the hot and cold temperatures of the heat engine. Either increasing T_h or decreasing T_c will increase the efficiency of the system, η. Varying either T_h or T_c generally has little consequence to terrestrial power systems, economically. However, decreasing T_c on a space power system dramatically increases its overall mass since heat engines in space must employ a thermal radiator. The size (surface area, and therefore mass) scales $\propto T_c^4$, i.e. the Stefan Boltzmann law; thus, in order to maximize specific power, W_e/kg, T_c must be *maximized* during the act of increasing electrical power output and T_h must necessarily increase in the process. Therefore, the feasibility of high power operations in space hinges on high temperature power

1

generation. However, unlike lower power level (1-10kW$_e$) reactors – such as KRUSTY – whose pre-existing technological components will be straightforward to deploy in the near term, higher power reactors have developed neither high temperature fuel nor an energy conversion system capable of sustained operation. Developing both these capabilities in tandem is critical to growing space mission capabilities to include large scale colonization, electric propulsion, etc.

There is an immediate need for high temperature fuel for space nuclear thermal propulsion (NTP), where a nuclear reactor core (T$_{fuel}$>2600K) is used to heat a hydrogen propellant [3, 4]. The high specific impulse and thrust provided by this technology is crucial to reducing manned transit times (down to several months) to Mars. Since NTP is a more near-term solution for NASA's propulsion needs than nuclear electric propulsion [2, 5], it has assumed a higher priority than higher electric power nuclear reactors. This is despite the priorities outlined in NASA's technology roadmaps [2, 5], which clearly planned on high power energy conversion research starting in 2016 with NTP starting in 2020. As a result, high temperature energy conversion for fission powered systems has been largely ignored in the space reactor community with only one paper [6] surfacing from the Nuclear and Emerging Technologies in Space 2019 conference, which was basically a rehash of an early 2000s study [7]. Since humanity needs higher power systems for space, it must make significant leaps in high temperature energy conversion technology. High temperature fuel alone will not allow this goal to come to fruition.

So far, the US is actively researching three technologies for high temperature energy conversion: Thermoelectric energy conversion (solid-state), the Stirling cycle (dynamic) and the Brayton cycle (dynamic). It is planned that thermoelectric power systems and Stirling engines will provide electrical power in the 10-100kW$_e$ range while Brayton engines will target 1-10MW$_e$. Specific power goals for the two categories are >5W$_e$/kg and >60W$_e$/kg, respectively. However, beyond 10MW$_e$, >200W$_e$/kg is desired. Such a specific power demand necessitates an energy conversion cycle peak temperature of ~2000K. Currently, 2000K is >400K hotter than the *maximum* hot operating temperature of state-of-the-art in Brayton technology. One such example, CFM International's Leading Edge Aviation Propulsion (LEAP) jet engine [8], features high temperature SiC-based ceramic matrix composites (CMCs) turbine shroud that allows for its relatively high temperature operation (>200K than traditional nickel based alloys). The current dogma in the space nuclear power community holds that further advancements in CMCs will enable the 400K increase in operating temperature required to realize the 200W$_e$/kg mark. It would not be wise for the space nuclear power community to rely solely upon material advances in Brayton cycle technologies to push such dramatic performance increases, especially when the technology has had no space flight demonstration to date. Consciously hedging all bets on a breakthrough in a single technological solution to enable several mission classes would be irresponsible. The community would benefit by considering at least one alternative concepts for high temperature energy conversion, namely Thermionic Energy Conversion (TEC).

Solid state energy conversion has been the only method of electrical power production for space missions to date, of which there are two types for nuclear power systems: Thermoelectric and Thermionic. The US has only flown thermoelectric systems. Successful missions have used exclusively radioisotope power systems, while SNAP 10A, the only space nuclear reactor attempted by the US (600W$_e$ in 1965), flew for 48 days before a non-nuclear electric failure shut down the reactor [10]. Russia, on the other hand, has flown over 35 nuclear reactors: all except two were thermoelectric based (500-800W$_e$). The other two derived their electric power via TEC [11] and both flew successfully for their entire planned mission durations of 6 months and 1 year, respectively in 1987. These in-core thermionic nuclear reactors, called

TOPAZ-I and TOPAZ-II (ThermiOnic Power from the Active Zone) operated at >5.5kW$_e$ at peak energy conversion temperatures of 1875K and specific power of 5W$_e$/kg. In 2001, the National Academy Press summarized in one of their key findings [12]:

Key Finding: Thermionic systems are unique for three reasons: (1) the inherently high power density of the conversion mechanism itself, (2) the systems' high heat rejection temperature, typically 1000 K, which allows thermionic systems to use compact radiators with relatively low masses, and (3) the systems' potential to operate in a higher power "surge mode" for sustained periods over a small fraction of their programmed life. The combination of these three advantages could allow for potentially significant advances in system power level density (kilowatts per kilogram).

Given a general scientific optimism for TEC's scalability, its established precedence for space nuclear power (over 30 years ago), and performance metrics that already fit in several NASA mission sets [2] it is time for the US nuclear power community to restart TEC research.

There are two main types of TECs: vacuum diode and plasma diode. The former is potentially applicable to small scale, non-nuclear devices. The latter has demonstrated its direct applicability to large scale, nuclear devices. The vacuum-diode TEC requires very low work function electrodes, with the emitter around 1.8 eV and the collector around 1.5 eV with emitter and collector temperatures of ~1200K and ~700K respectively. This method requires small emitter-collector gaps of 1-10 μm to mitigate the space charge effect since the repulsion of electrons in the interelectrode gap limits the device's output current. The vacuum-type TEC is the main focus of current US R&D thermionic academic and industrial efforts as these devices have potential applications to small-scale, non-nuclear devices, e.g. waste heat to power production in electronics. However, the prospect of vacuum-type TECs being applicable to in-core nuclear devices is dismal on two accounts. First, when scaling to larger devices, thermal gradients or any misalignment within macro-sized electrodes would immediately causes contact between them, which shorts the circuit. Second, high radiation environments will easily perturb (if not destroy) the nano-scale microstructures required to mediate vacuum-mode thermionic energy conversion.

The plasma diode-type TEC mitigates the space charge effect by injecting the interelectrode space with a low-pressure vapor. Electrons transiting the gap partially ionize the gas into a low-temperature plasma. Being electrically neutral, the plasma serves as a buffer to eliminate the space charge effect between transiting electrons. Thus, without the space charge effect, typical plasma diode TEC gap sizes range from 100μm-1mm.

The most common approach uses a low pressure cesium vapor (1-10 torr) due to its low ionization potential and its ability to favorably lower refractory metal (e.g. tungsten, molybdenum, niobium) work functions, thereby raising emission current. The most common electrode materials are tungsten (emitter) and molybdenum (collector); adsorption of cesium onto their surfaces drives down the effective emitter work function to around 1.8 eV and the effective collector work function to around 1.5 eV. These systems in the laboratory have been demonstrated with efficiencies of 25-35 % at emitter and collector temperatures of 2000 K and 1000 K, respectively [40]. However, practical devices, such as the TOPAZ nuclear reactors (I and II) have thus far only achieved 5.5 % efficiency. Thus, plasma diode thermionic converters are not without their design challenges. The physical drawback of the device is that up to 50% of the emitted electron energy is lost generating the cesium plasma: this drives down electrical

output and thermodynamic efficiency limits current Cs vapor based TEC designs to spacings under 0.5mm [13]. At such spacings, nuclear TEC devices have a lifetime of just under 12,000 hours due to irradiation swelling [12].

In this thesis, we are proposing an alternative plasma ionization source for in-core nuclear reactor TECs which utilizes heavy ion fission fragments and their subsequent beta decay from un-cladded nuclear fuel elements. Fission fragment deposition (50-100MeV) and high energy beta decays (2-8MeV) are a vastly more energetic and higher power density deposition process than thermionic electron deposition (~1eV). This would greatly improve the device two-fold. First, it would increase the plasma electron temperature, thus enhancing device efficiency by more than 30%, and second, it would relax design constraints, allowing for noble gas conduction and spacings in excess of 5mm. This concept was explored briefly by General Motors and the Office of Naval Research in the 1960s which yielded promising results with electron densities (n_e) of (2-3)x10^{12} cm^{-3} and neutron fluxes (ϕ_n) of 0.8-1.5x10^{13} cm^{-2}s^{-1} [14] and by Russia, who continued experimental work in the 1970s, achieving competitive space charge mitigation conditions (n_e = (1-2)x10^{13} cm^{-3} for ϕ_n =(1-8)x10^{13}cm^{-2}s^{-1}) [15]. Both nations' work in TEC eventually gave way to the more developed Cs vapor diode concept, largely because of its potential applications outside nuclear technologies, e.g. solar, fossil fuel, and process heat. Nuclear excited plasma research was ultimately obscured by a mostly classified pursuit in nuclear pumped laser technologies. It has since been diminished into an esoteric topic known only by a work force that is generally unavailable, retired or (mostly) deceased.

1.2 Thesis Objectives and Scope

Given that fission fragment generated plasmas have achieved free electron densities capable of efficient thermionic electron transport in laboratory settings [14, 15], it would be illuminating to extrapolate these results to plasma conditions attainable in a nuclear reactor. Such a model could establish the feasibility, capabilities, and applications of charged particle excited plasmas to in-core thermionic nuclear reactors in space (and beyond). Determining critical parameters to thermionic plasmas, namely the bulk plasma density and temperature, will directly infer useful reactor-scale performance values, such as electrical power production and thermal and electrical efficiency. This knowledge, across a wide range of input variables, would solidify its specific power (W_e kg^{-1}) potential and thus inform its potential mission set applications.

The modeling paradigm for the proposed reactor concept is akin to other fission based heat engines. But, while both types may establish their core neutronics through a common reactor physics design package (e.g. MCNP, SERPENT, etc.), a heavy ion thermionic energy converter (HITEC) reactor's electrical power generation has nothing in common with that of conventional fission heat engines. Fundamentally, HITEC's heat input and electrical output both derive from the kinetic energy of fission fragments and/or their subsequent β^- decay; its electrical power model depends on directly tracking charged particle energy deposition in a gaseous medium, rather than indirectly for thermal hydraulics and electromechanics of conventional power generation systems. HITEC thus cannot interface with standard electrical power modeling workflows.

Instead, the model must couple core neutronics (which infers fission rates) to a charged-particle transport code. This would track charged particle energy deposition across multiple regions (the electrodes and gas) to establish plasma ionization rates. Through basic heat transfer equations and plasma particle and energy balances, thermionic emission and steady state plasma

parameters (electron density, n_e) and temperature, T_e) may be determined and ultimately derive current-voltage characteristics for power production. This dissertation work will provide a modeling package that performs the stated workflow given only a set of user input parameters. This gives designers the ability to model in-core thermionic reactor electrical performance with little knowledge of charged particle transport or low temperature plasma physics – subject areas that are not core to the nuclear engineering discipline. The overall objective is to allow reactor core designers to predict electrical power outputs of in-core, charged particle ignited thermionic nuclear reactors. Such a capability has never existed in nuclear reactor design.

The design tool incorporates physics from several disciplines: charged particle transport in matter, heat transfer, and low temperature plasma physics. As stated above, the package simulates the electrical performance characteristics of a novel in-core thermionic nuclear reactor design. This is accomplished with the following workflow:

1. **Charged particle stopping power models:** fission fragments' Z, A, and kinetic energies (E$_0$) are sampled from a library generated by the Fission Reaction Event Yield Algorithm (FREYA) [46]; in the case of β^- transport, the corresponding average β^- kinetic energy is sampled. This particle is assigned a specific position and angle of emission in the fissionable material, then its energy loss is tracked through the origin electrode (emitter or collector), interelectrode gap (plasma), and endpoint electrode (collector or emitter).
2. **Plasma model:** based on the energy deposition for the regions calculated in step 1, total energy deposition per region is normalized to their respective volumes (provided by user). Given a volumetric fission rate or decay rate, n_e and T_e are calculated at the emitter and collector boundaries (given a user input T_E and T_C) via particle and power balance equations; proper rate constants are provided.
3. **I-V characteristics for TEC unit cell and reactor scaling:** saturation current, output voltage, and resistivity are calculated directly from the plasma density and temperature; these parameters also infer electrical efficiency. Device efficiency is calculated by comparing electrical power output to the heat input. Given the length of the fuel element and spacing (user input), and using the flux-electron density relation $\sqrt{\phi} \propto n_e$ (derived later), reactor-scale I-V and efficiency curves are readily calculated. The thermal neutron spatial flux distribution, $\phi_{th}(r,z)$ behaves as axial and radial Bessel functions assuming a cylindrical core with axially and radially uniform fuel loading. This infers $n_e(r,z)$ and $T_e(r,z)$ which are directly proportional to the power output.

Figure 1 summarizes this workflow diagrammatically. As an emphasizing point, the modeling tool is the first of its kind to apply data from real, energy conserving fission events (from FREYA) as well as average beta decay energy spectra from the resulting fission fragments (from ENDF/B-VIII.0 decay libraries). The current standard practice for modeling fission fragment generated plasma phenomena assumes an average "light" and "heavy" fission fragment's Z, A, and E$_0$; beta spectra have only been assessed for singular radioactive species. Though these practices may broadly capture charged particle transport phenomena in plasmas, modeling individual fission events and subsequent beta decay spectra allows users to determine highly resolved charged particle (from both fission fragment subsequent beta decay) energy-angle flux spectra from the fuel's surface. Such a capability would be particularly useful to more detailed

plasma models that determine ionization and excitation numerically by solving the Boltzmann kinetic equation. Thus, not only will this first generation design tool be able to estimate reactor scale performance, but it will also provide highly resolved charged particle spectra emitted from fuel elements of various dimension and material composition to facilitate more advanced modeling schemes.

The design tool will be useful across a wide range of users, from power reactor designers to low temperature plasma modelers (e.g. lasers, glow discharge phenomena, etc.). To the latter, beyond the basic capability of determining mission-specific details (e.g. system total/specific power, efficiency, etc.) the modeler, with sufficient low-temperature plasma knowledge expertise, can gain further insight into unique operational characteristics (electrical) inherent in thermionic diodes [12] such as pulsed power operation and EM wave generation and propagation in fuel cells. Such features are outside the scope of
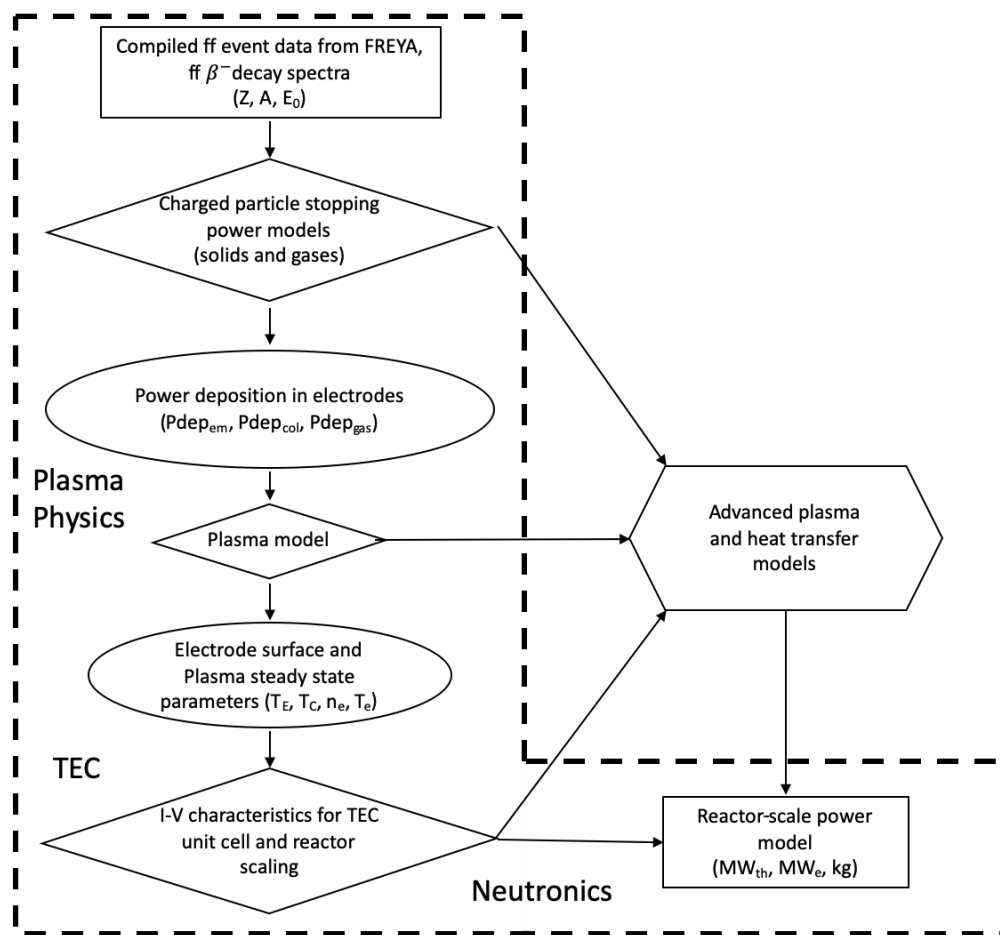

Figure 1. Modeling flow diagram. The red border encapsulates the steps included within the scope of the thesis work. Diamond = calculation; oval = output/input; square = source data/product data.

the thesis's modeling objectives which are concerned only with determining steady state electrical power generation. However, given the widespread application of pulsed power, RF

plasmas, and EM wave cavity interactions to civilian and defense technologies, their connection to nuclear reactor generated plasmas should be explored in future work.

In summary, the in-core thermionic nuclear reactor is uniquely well-suited for high powered missions in space given its inherently high power density, high rejection temperature, and high power "surge" mode. Yet, there has been no technological development in the US on this type of reactor since the TOPAZ-II International Program, which was dissolved in the early 1990s. Given that there is no obvious alternative reactor system design suitable for high powered space missions, a continued hiatus in in-core thermionic reactor R&D could allow the US to fall behind competitors who are actively engaged in this field of research (e.g. Russia and China) [51, 71].

To address major criticisms of the reactor's design, which mainly center on the design challenges involved with converters' small dimensions (interelectrode gap < 0.5mm) and use of a cesium plasma, the author proposes an alternative plasma ionization mechanism that would relax these design constraints by utilizing kinetic energy from fission fragments and their subsequent beta decay. The only US research that explored this concept specifically for TEC occurred in the 1960s by a joint Office of Naval Research and General Motors effort: their experimental results exceeded theoretical expectations by factors of 5 to 30 ($P_{exp} \sim 0.25W/cm^2$). However, the group could not reconcile the differences between experimental results and theoretical models, and consequently were unable to scale their results to a power reactor. The primary objective of this thesis is to develop a first-of-a-kind capability to model nuclear reactor electrical power characteristics based on charged particle-ionized TEC plasmas. This design tool is specifically aimed to serve nuclear reactor designers with no prior expertise in the multiphysics involved with this energy conversion process so that they may obtain meaningful results without a plasma physics knowledge-base. A unique feature of the model is that it samples fission fragments from FREYA and beta decay energy spectra from the resulting fission fragments: this allows users to determine highly resolved charged particle energy-angle flux spectra from the fuel's surface and incident on non-fuel surfaces. It follows that the user could use the code to generate source data for more detailed plasma, heat transfer, and material damage models that would draw directly from these charged particle flux spectra.

As a final note, though the focus of this dissertation centers on developing a model for full-scale nuclear reactor core designs, the model's broad applicability – from small scale experiments to large scale nuclear reactor design – will extend the user base across multiple fields in physics and engineering, allowing maximal connectivity between design teams. This connectivity will be instrumental in exploring all aspects nuclear excited plasma-based TEC, a multidisciplinary subject matter at the intersection of nuclear and plasma physics.

Chapter 2: Charged Particle Ionized Plasmas

2.1 Literature Review

Low-temperature, Nuclear reactor generated plasmas – via charged particle excitation – have almost exclusively been researched for applications to lasers since their inception in the early 1970s. Correspondingly, there is a wealth of literature on the subject matter that is well documented elsewhere [16]. The majority of studies in nuclear reactor ignited plasmas have been computational-theoretical and there's an obvious lack of experimental data – especially in

discerning basic plasma properties, such as the electron density, n_e, and electron temperature, T_e. This lack of experimental data is likely due to the context under which charged particle ignited plasmas were researched in the first place, which was for nuclear pumped lasers, a field that is primarily concerned with excited state population inversion and subsequent light amplification. However the chief difference between laser plasmas and TEC plasmas lies in their desired outcome: laser plasmas seek maximum *excitation* whereas TEC plasmas seek maximum *ionization.* This gives rise to a sparsity of experimental data in the following areas crucially important to developing accurate charged particle ignited TEC plasma models:

1. High temperature parent gas (1000K – 3500K) reaction coefficients where the electrons are not in thermal equilibrium with the gas i.e. $T_e > T_g$. Especially important to quantify at high temperature is dissociative recombination, the chief electron recombination mechanism for high pressure plasmas (except for helium), which differs significantly from low temperature values due to vibrational excitations [17]. Dissociative recombination at high gas temperature has been studied experimentally, to a certain extent, in shock wave-heated plasmas, where $T_e = T_g$ and may be valuable to low power density modeling (or with helium as a parent gas), where electrons are able to completely thermalize with the surrounding gas.
2. Heavy ion total ionization/excitation cross sections for noble gases (heavier than helium) at intermediate to high energies. This data would be useful to modeling any charged particle ignited plasma under circumstances where additional electromagnetic fields are present as it would increase accuracy in modeling the electron energy distribution function (EEDF); an a priori knowledge of the EEDF established by charged particle ionization is crucial to subsequent plasma behavior when applying additional electromagnetic excitation. Though experimental data – or well established models in lieu of it – for singly charged, mono-nucleonic protons exist for essentially any energy and atomic species, the same cannot be said for heavy ions, whose nuclear properties and charge states may vary throughout the ionization deposition process [18].

To the author's knowledge, there is only one major US study that attempted to probe basic characteristics of nuclear reactor excited plasmas for the specific purpose of TEC, mentioned in Chapter 1 [14]. A collaboration between the Office of Naval Research and General Motors Corporation, the study comprises of 8 annual reports and a final report. The final report – the focus of our analysis – consists of two volumes: the first is unclassified and specifically confines its theoretical and experimental treatment to the plasma physics of the TEC device and the second was previously classified and analyses the thermionic electron transport (both theoretically and experimentally) in the nuclear reactor generated plasma as described in the first volume. Consistent across both volumes, which had two entirely different experimental setups, was the significantly greater electron density found experimentally in the Ar:Cs (1:10^{-5}) plasma compared to that predicted by theoretical models. Volume I used a thin (25μm) ^{235}U foil as its plasma ionizing source while Volume II used a much thicker (0.6mm – 1.5mm) unclad BaO-UO$_2$-W thermionic emitter element. Both experimental setups are summarized and analyzed in Chapter 5. We argue that the anomalously high electron density may likely be accounted for by the study's use of inaccurate dissociative recombination rate constants and an underestimation of the electron temperature.

The following sections address the foundational physics involved with charged particle ignited plasmas. It reviews principles of energetic charged particle transport in matter and how this translates into the ionization and excitation of gaseous matter. The discussion transitions into low-temperature plasma theory, where an electron particle and energy balance are developed for the conditions expected in a power producing device. The particle-energy balance draws a relation between reactor power (as a function neutron flux) and the electron density and temperature n_e and T_e, respectively. Electrical power output from a thermionic fuel element is directly calculated by quantities n_e and T_e via to the Richardson Dushman equation, elucidated in Chapter 3. We finish by comparing our particle-energy balance to that of both the much more ubiquitous electrically ionized high pressure plasmas and reference [14], highlighting the fundamental differences in the respective treatments.

2.2 Charged Particle Transport in Matter

Fundamentally, when energetic charged particles travel through matter, they are slowed down and eventually stopped by three main collisional mechanisms: electronic, nuclear, and radiative stopping. The sum of these individual mechanisms gives rise to a total *stopping power*, which characterizes the energy deposition per unit length as a function of the particle's initial energy. The total path length, s, an energetic charged particle travels, is related to its energy dependent stopping power by:

$$s = \int_{E_0}^{E_f} \left(-\frac{dE}{dx}\right)^{-1} dE \tag{2.1}$$

where

$$\frac{dE}{dx} = \left(\frac{dE}{dx}\right)_{el} + \left(\frac{dE}{dx}\right)_{nuc} + \left(\frac{dE}{dx}\right)_{rad} \tag{2.2}$$

where $\frac{dE}{dx}$ is the total stopping power [MeV mm^{-1}] and is the sum of the energy dependent electronic, nuclear and radiative stopping powers and E_0 and E_f are the initial and final energies of the charged particle, respectively [MeV]. Hans Bethe first derived energy dependent relationships between charged particles' stopping powers and respective ranges in matter in 1930: his initial treatment of the problem serves as the underlying foundation for virtually every field concerned with charged particle transport in matter, and to this day is an active field of study.

This thesis applies established stopping power models in cold matter to both fission fragment and beta particle energy deposition as they traverse solid state fuel and gaseous media. Energy deposition into the solid state fuel is dissipated mainly as heat and material damage, whereas energy deposition into the gaseous media produces ionization and excitation for the modest power deposition of our concern (1-10 W cm^{-3}). Though the phenomena that arise due to charged particle stopping in solid and gaseous state matter differ from one another to a great extent, the underlying physics of the stopping itself may be modeled the same! We consider the energy deposition of low energy heavy ions and electrons separately, as their relative velocities

at birth are quite different from one another, due to their mass and charge disparity; fission fragment energy loss is due to electronic and nuclear stopping, whereas beta decay electron energy loss is due to electronic and radiative stopping. Later sections will expound on how $\frac{dE}{dx}$ energy is transformed into ionization in gaseous media.

2.2.1   Low Energy Heavy Ions from Fission

A comprehensive review of ion stopping powers may be found in multiple references [19, 20]; a more recent summary that compares the current state-of-the-art stopping power models and existing experimental data for low energy stopping in cold matter can be found may be found in reference [21]. As we are much more concerned with the general results from these theoretically and experimentally complicated models than we are with the underlying physics of them, we will limit our discussion to the basic formulae that are incorporated into the HITEC model. Further investigation into more fundamental aspects of heavy ion stopping is encouraged and may begin with references therein.

The radiative stopping term in (2.2) may be neglected when considering heavy ions that emerge from most nuclear reactions or processes. This loss mechanism only becomes significant for charged particles traveling at relativistic speeds ($\frac{v}{c}$ >0.85), which for a typical light fission fragment of mass of 95 amu, would require an initial kinetic energy of order 5 GeV; as light fission fragments take away roughly 100 MeV per fission event, this is 50 times below the threshold where radiative stopping becomes significant. Thus, fission fragment energy loss comes almost exclusively from electronic and nuclear stopping, and we are concerned with the *sum* of these two energy deposition mechanisms when calculating heating and damage for solids and ionization rates for gases.

We will consider the electronic stopping component first followed by nuclear stopping. The electronic stopping of heavy ions in any form of matter is highly empirical. Basic theories do exist to explain, phenomenologically, electronic stopping of large nuclei, but it is only through empirically fitting available experimental data to these theories that allows stopping models to achieve accuracies within a modest 10-20% of experimental results. Here, we adopt the most widely accepted model in terms of accuracy, Stopping and Range of Ions in Matter (SRIM). This program, which has had many contributors over time, separates electronic stopping into a low velocity group in which the stopping power is proportional to the ion's velocity (called the Lindhard-Scharff model), and a high velocity group where the stopping power is proportional to a more complex function of energy (the Bethe model). To calculate the stopping of a heavy ion, the stopping of a proton is scaled by the ion's effective charge via the Brandt-Kitagawa (BK) Theory [22]; the culmination is empirically fit with a large experimental data set, which is discussed in much greater detail elsewhere [19]. Bethe's model, colloquially known as the Bethe-Bloch formula, on the other hand, is applicable to ion velocities >1.5MeV/amu; this is higher than most energetic fission fragments, which, are typically emitted at a velocity just under 1MeV/amu. Fission fragments generated at moderate to relatively low speeds obey the empirical form [19]:

$$\left(dE / dx \right)_{i,el} = \left(dE / dx \right)_{H,el} \{[1 - \exp(-\alpha)][1.034 - 0.1777 \exp(-0.08114 Z_i)]\}^2$$

where $\alpha = 0.866\sqrt{\frac{E_i}{25A}}\frac{1}{Z_i^{2/3}} + 0.0378 \sin\left(\pi\frac{0.866\sqrt{\frac{E_i}{25A}}\frac{1}{Z_i^{2/3}}}{2}\right)$ and E_i is in keV. This expression

is valid until the heavy ion has slowed to the "velocity proportional" stopping power regime, where it assumes a proportionality to $\sqrt{E_i}$. We delve into this formulation in greater detail in Chapter 4 where the HITEC model is introduced.

In contrast with electronic stopping, where projectile nuclei interact with target atom *electrons*, nuclear stopping occurs as the result of the projectile's interaction with target atom *nuclei*. As formulated by [19] the reduced energy-dependent nuclear stopping power is expressed as:

$$\left(\frac{dE}{dx}\right)_{nuc} = \frac{\ln(1 + \alpha\epsilon)}{2(\epsilon + \beta\epsilon^\gamma + \delta\sqrt{\epsilon})}$$

Where $\alpha, \beta, \gamma, \delta$ are empirically adjusted parameters and will be fully defined in chapter 4. As an example, $\left(\frac{dE}{dx}\right)_{el}$, $\left(\frac{dE}{dx}\right)_{nuc}$ and their sum are plotted in Figure 2.1 for a typical light ($A_p = 96$, $Z_p = 38$) and heavy ($A_p = 136$, $Z_p = 54$) fission fragment in 0.5 atm argon. In general, we see that the electronic component of the stopping power dominates total energy deposition from the initial fragment energy (~67MeV for the heavy fragment and ~95MeV for the light fragment) down to approximately 5MeV. We note that excitation and ionization processes are solely due to electronic stopping, as nuclear stopping is by definition an interaction between a projectile and atomic *nuclei*. However, as will be shown later, nuclear stopping can be a significant contributor to material heating, thus it is important to track both electronic and nuclear stopping when modeling HITEC systems.
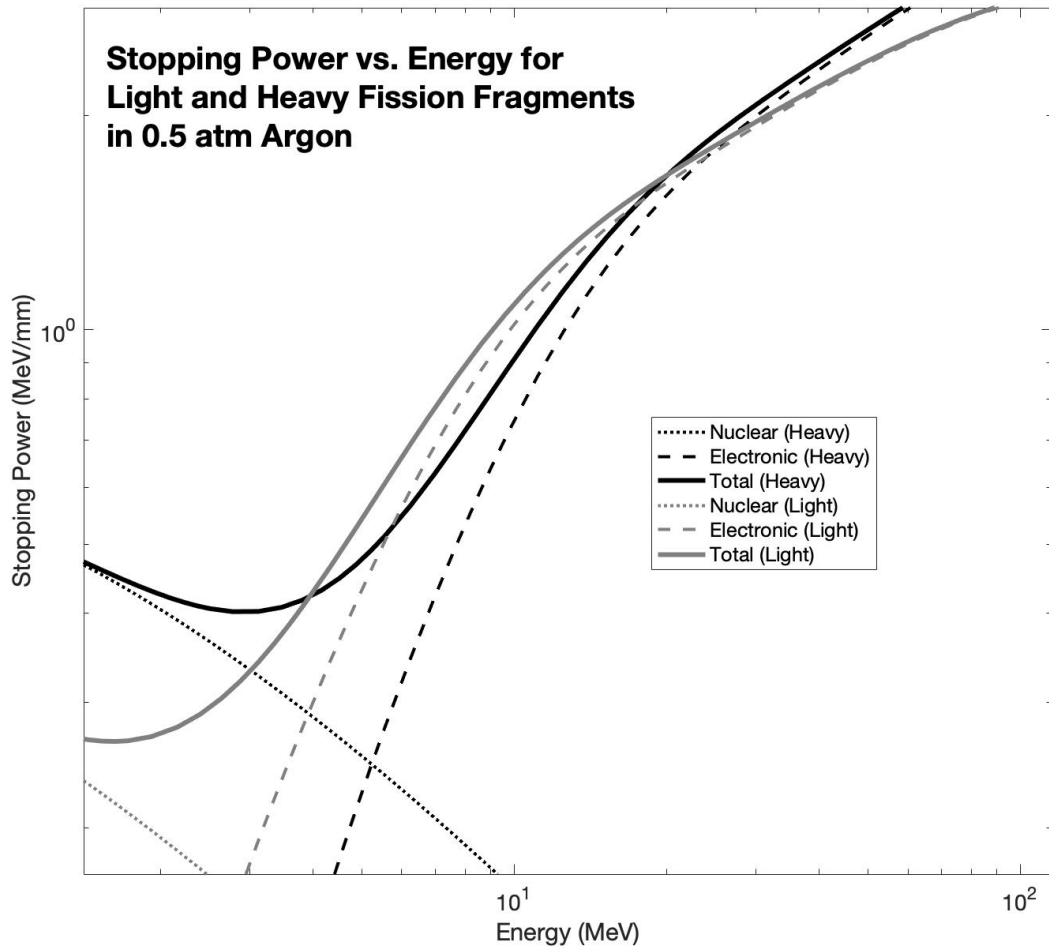
Figure 2.1 Energy dependent stopping power for typical light and heavy fission fragments in argon.

2.2.2   High-Energy Electrons from Beta Decay

Referring back to equation (2.2) under the context of electron stopping from fission fragment beta decay, we see now that there is no nuclear stopping component but in its place, radiative stopping. This is because the equivalent "nuclear stopping" collision for an electron is elastic-momentum transfer: these collisions do not dominate electron energy loss until the electron's energy has relaxed below the excitation threshold, around 15 eV or 0.001% of the electron's initial energy. Further, for typical beta decay energies, from 1-5 MeV, the electron's velocity is nearly the speed of light ($\frac{v}{c} > 0.9$) making radiative stopping significant. The expressions for both collisional and radiative stopping powers for electrons were derived by Bethe:

12

$$\left(\frac{dE}{dx}\right)_{el} = \left(\frac{e^2}{4\pi\epsilon_0}\right)^2 \frac{2\pi N_{av}\rho Z_t}{m_e c^2 \beta^2 A_t} \Bigg[\ln\left(\frac{E_p(E_p + m_e c^2)^2}{2I^2 m_e c^2}\right)$$
$$+ (1 - \beta^2)$$
$$- \left(2\sqrt{1-\beta^2} - 1 + \beta^2\right)\ln 2 \qquad\qquad (2.3)$$
$$+ \frac{1}{8}\left(1 - \sqrt{1-\beta^2}\right)^2 \Bigg]$$

and

$$\left(\frac{dE}{dx}\right)_{rad} = \left(\frac{e^2}{4\pi\epsilon_0}\right)^2 \frac{(E_p + m_e c^2)N_{av}\rho Z_t^2}{137 m_e^2 c^4 A_t}\Bigg[4\ln\left(\frac{2(E_p + m_e c^2)}{m_e c^2}\right) - \frac{4}{3}\Bigg] \qquad (2.4)$$

Where c is the speed of light, $\beta = \frac{v_p}{c}$, I is the average excitation potential of the target atom and follows the general relationship $I \approx 10eV * Z_t$, and E_p is the energy of the projectile (an electron in this case). More accurate experimental data based off of both equation (2.3) and (2.4) have been tabulated in the National Institute of Standards (NIST) Electron STopping powers And Ranges (ESTAR) [23], and as an example, the electron energy-dependent $\left(\frac{dE}{dx}\right)_{el}$, $\left(\frac{dE}{dx}\right)_{rad}$ and their sum are plotted in figure 2.2 up to the maximum kinetic energy from fission fragment beta decay.

We see that even at the highest energies expected of beta decay, radiative stopping contributes no more than 10% to the total stopping power. Therefore, for this thesis's modelling purposes radiative stopping may be neglected. According to NIST [23], stopping power values and corresponding range calculations via equation (2.3) and (2.4) according to the continuous slowing down approximation (CSDA) are accurate from very high electron energies (1GeV) to 1 – 10keV. This lower bound is due to lack of shell correction incorporated into the model; the gross effect is an overestimation in electron stopping power at energies below 1 – 10keV. As our formulation of ionization and heating rate models are chiefly concerned with *total* energy deposition, a physically macroscopic quantity, and considering the average fast electron from fission fragment beta decay is born at an energy of order 1MeV, we may capture 99.9% of the electron's energy deposition due – sufficiently accurate for reactor scale devices.
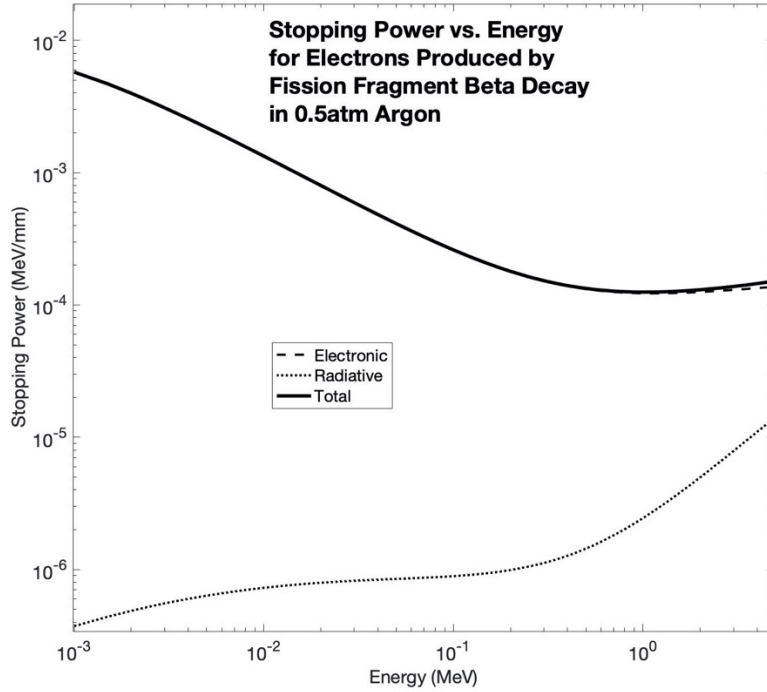
Figure 2.2 Energy dependent stopping power electrons produced by fission fragment beta decay in argon.

2.2.3   Energy Deposition

Perhaps the most obvious consequence of charged particle stopping in matter concerning electrical power generation is heat production, which comes directly from the energy deposition during this process. All practical devices can create electricity from nuclear energy by transforming energy deposition into heat (in the traditional sense). A discussion on how nuclear reactions produce heat in matter would be pedantic, as it has been a standard nuclear power approach for nearly 70 years. Instead, we refresh the reader with a simplistic formulation of how nuclear fuel deposits *energy* into both itself and surrounding material; these basic principles may be directly applied to heat generation and plasma ionization.

Let us consider a volume of fissionable material of thermal neutron fission cross section σ_{th} [cm^2] volume V [cm^3] and density n [cm^{-3}] that is subject to a uniform thermal neutron flux ϕ_{th} [cm^{-2}s^{-1}]. Further, we will assume the volume to be sufficiently large such that leakage of fission fragments and subsequent beta decays that occur near the boundary of volume V may be ignored. Then, we may express the rate of fission R [events s^{-1}] per unit volume [cm^{-3}] to be:

$$R/V = \phi_{th}\sigma_{th}\,n$$

Knowing the prompt (≤ 0.1 s) energy released per fission event to be roughly 200 MeV (or 3.2 x 10^{-11} J) and that around 80% is transferred into the kinetic energy of the fragments, we define this energy as E_{fiss} (J). Since we ignore leakage, the rate at which energy is produced by the

14

material is identical to the rate at which it is absorbed in the material. Then the rate at which energy is absorbed by the fuel per unit volume is:

$$P_{fuel} = \phi_{th}\sigma_{th}\, n\, E_{fiss} = \frac{R}{V} E_{fiss}$$

Where we define P_{fuel} [W cm^{-3}] as the specific *power absorption* of the fuel. In any other discussion regarding nuclear power, P_{fuel} would typically be defined as specific heat generation rate q''', and from this point, the conversation would run along the typical track to develop relevant heat transport equations between fuel, cladding, and coolant channels.

Suppose, now, we have a volume of fissionable material within another volume where neutron interactions may be neglected – i.e. a volume whose dimension is much smaller than a neutron's mean free path of interaction – but can absorb energy from other ionizing radiation. Further, let this volume be bounded by a surface such that energy transferred beyond this boundary is lost from the system. If we desire to assess the power absorption of this neutron-agnostic volume, we must calculate the fission fragment and beta decay leakage near the boundary of the fissionable material. The rate of energy production for this volume is simply the fission rate times the energy per fission becomes:

$$E_{prod} = R * E_{fiss} = \phi_{th}\sigma_{th}\, n_{fuel}\, V_{fuel} E_{fiss}$$

Correspondingly, the energy loss rate of the volume may be taken as some fraction of E_{fiss}, f, where $0 < f < 1$. Setting this volumetric energy loss rate equal to the energy absorption rate in the neutron-agnostic material, we see the specific power absorption for the neutron-agnostic material becomes:

$$P_{abs} = \phi_{th}\sigma_{th}\, n_{fuel}\, E_{fiss} f \frac{V_{fuel}}{V_{abs}} \tag{2.5}$$

which is more conveniently expressed by defining a fuel constant, $\beta_{mat} = E_{fiss}\frac{V_{fuel}}{V_{abs}}$ and $\Sigma_{th} = \sigma_{th}\, n_{fuel}$ such that $P_{abs} = \phi_{th}\Sigma_{th}\beta_{mat}f$. By satisfying the energy conservation relation, $E_{prod} = P_{fuel}V_{fuel} + P_{abs}V_{abs} + E_{loss}$ it is easy to see that

$$P_{fuel} = \phi_{th}\sigma_{th}\, n_{fuel}\, E_{fiss}(1-f) - \frac{E_{loss}}{V_f} \tag{2.6}$$

where E_{loss} is the total power lost from the system. We note that these power density relations may be readily adapted to radioactive sources by taking $\phi_{th}\sigma_{th} \rightarrow \lambda_{fuel}$ which is the decay constant of the fuel and $E_{fiss} \rightarrow E_{decay}$.

Specifically for P_{abs}, the $\frac{V_{fuel}}{V_{abs}}$ and f terms imply a stopping power dependence. For heavy ions (e.g. fission fragments), where the material stopping power is high, a fuel-absorber combination of practical dimension may only achieve $\frac{V_{fuel}}{V_{abs}} \sim (1-5)$ x10^{-3} given the typical fission fragment range (in the fuel) of 5μm and absorber thickness of 1mm-5mm whereas the

equivalent fuel-absorber combination for beta decay electrons may achieve $\frac{V_{fuel}}{V_{abs}} \sim 1 - 2$ given a typical beta decay electron range of 1-2 mm. Indeed, E_{fiss} (~160MeV) is 10^2 greater than E_{decay} (~1 – 10 MeV) which compensates for the volume fraction disparity to a great extent, but given f's strong dependence on the particular species' stopping power, a clear comparison of P_{abs} between fission fragments and beta decay cannot be drawn without more exact analysis. This will be addressed later in Chapter 4.

2.2.4   Gas Ionization

Ultimately, we are concerned with how energetic charged particles from nuclear fission and subsequent beta decay produce ionizing events (and peripherally excitation events) in a gaseous medium. We therefore seek to draw a relation between a particle's energy deposition – that is, its integrated $\left(\frac{dE}{dx}\right)^{-1}$ over some energy interval – and the number of ionizations (excitations) it produced over the course of its energy deposition. This is quantity is known as the "W" value and is specific to the gaseous medium under irradiation by charged particles.

Calculating W may be achieved in a number of ways, summarized by Platzman [24] namely by calculation from: sequential counting by use of cross sections directly [25], degradation spectra [26, 27] or an energy balance [28]. The former two methods are purely theoretical whereas the latter is semi-empirical. The details of charged particle ionization theory may be further explored using the references therein as a starting point. However their equations are reproduced and explained briefly here from [24]. It should be noted that the following equations are expressed for the case where the ionizing particle is an electron. Starting with sequential counting, or the Fowler equation, we define the number of ionizations, N_{ion} for some electron energy ε in terms of the sum of energy dependent probabilities for ionization:

$$N_{ion}(\varepsilon) = p_{ion}(\varepsilon) + \sum_n p_n(\varepsilon)N_{ion}(\varepsilon - E_n)$$
$$+ \int_{E_{ion}}^{(\varepsilon+E_{ion})/2} p_{ion}(\varepsilon, \varepsilon_s)[N_{ion}(\varepsilon - \varepsilon_s)$$
$$+ N_{ion}(\varepsilon_s - E_{ion})]\, d\varepsilon_s$$

Where $p_{ion}(\varepsilon) = \frac{\sigma_{ion}(\varepsilon)}{\sigma_{in}(\varepsilon)}$ and $p_n(\varepsilon) = \frac{\sigma_n(\varepsilon)}{\sigma_{in}(\varepsilon)}$ are the ratios of the ionization and nth excitation cross sections to the total inelastic cross section, respectively, $p_{ion}(\varepsilon, \varepsilon_s)d\varepsilon_s$ is the analogous probability of ionization with production of a secondary electron having a kinetic energy $\varepsilon_s - E_{ion}$, E_n (E_{ion}) is the nth excitation (ionization) energy of the medium, and ε_s is the energy of a secondary electron produced by impact of the primary electron. Then the total yield N_{ion} is found by tracking a particle and its secondaries in ε as they lose their energy to ionization and excitation events. Again, the above equation is applicable to high energy electrons and additional terms arise when calculating ionization events for heavy ions [28]. In essence, sequential counting tracks the particles' (both primary and secondary) energy degradation to discern the total ionization of the medium.

The degradation spectra method from Spencer and Fano, on the other hand, approaches the problem from the opposite direction. Instead of solving for the *total ionization* via particle-energy tracking, this method solves for the *source* of electrons generated at energy ε_0 that gives rise to a particular electron degradation spectrum. This degradation spectrum, denoted $y(\varepsilon)$, is related to the number of ionizations N_{ion} by:

$$N_{ion}(\varepsilon_0) = n \int_0^{\varepsilon_0} y(\varepsilon)\sigma_{ion}(\varepsilon)d\varepsilon$$

Where $\int_0^{\varepsilon_0} y(\varepsilon)d\varepsilon = 1$ [m^{-2}], $y(\varepsilon)$ is the electron energy spectrum (of *all* electrons present), n is the number of molecules present, and $\sigma_{ion}(\varepsilon)$ is the ionization cross section [m^2]. Here, some $y(\varepsilon)$ is solved for by numerical integration given some monoenergetic source of electrons of energy ε_0 and n and $\sigma_{ion}(\varepsilon)$ are known such that a number of ionizations may be calculated through direct integration.

Some disadvantages to using these methods on spatially full scale systems become quickly apparent; the most obvious is what is known as the "bookkeeping" problem. This manifests itself in the sequential counting method as follows: we see that one energetic particle, e.g. a single electron at 1MeV, may make more than 10^5 primary ionizing events; the secondary electrons will follow on to make several more ionizing events, whose tertiary electrons further ionize – and so on and so forth until either *all* the electrons relax under the subexcitation threshold (i.e. $\varepsilon < E_n$, where $n = 1$). Modeling a physical system on the size scale of a nuclear reactor (such as this thesis) based on this method, where primary particle fluxes are in excess of 10^{12} particles cm^{-2}s^{-1}, is beyond the capability of a single graduate student. Similar bookkeeping issues arise when solving for $y(\varepsilon)$, which involves numerical integration over energy groups that can span 8 orders of magnitude. To further complicate things, in order to model both fission fragments and high energy electrons, the individual energy dependent cross sections for all possible fission fragments (whose ionization states are also energy dependent) and electrons must be known reliably; this assertion would be dubious.

Alternatively, these methods are very useful when applied to small systems, as both offer unique physical insight into the problem at hand: sequential counting gives an exact number of ionizations given an initial particle energy, thus a very accurate measure of W; degradation spectra yield an electron energy distribution function (EEDF) of a specific source of ionization, thus a more precise picture of the total free electron population's energy characteristic. As we will see, however, for the specific purpose of thermionic energy conversion, we need only average values of W and may comfortably assume an EEDF for the low energy plasma electrons which govern the behavior of electrical power producing devices.

We now turn our attention to the energy balance method; by far the most readily verifiable method by both experiment and theory. The energy balance expression for the W value was formed[24]

$$T_0 = N_{ion}\bar{E}_{ion} + N_{ex}\bar{E}_{ex} + N_{ion}E_{ave} \tag{2.7}$$

where T_0 is the total kinetic energy absorbed in the medium, N_i and N_{ex} are the number of singly charged ions and excited atoms produced with their corresponding energy expenditures, $\bar{E}_i$ and $\bar{E}_{ex}$ respectively (eV), and E_{ave} (eV) is the average energy left to the free, *subexcitation* electron. Over some decades of extensive experimental and theoretical research [24 – 29] $\bar{E}_i$, $\bar{E}_{ex}$, and $\bar{\varepsilon}_e$

values were discerned, allowing for the semi-empirical relation of equation (2.7) to come to fruition. It is important to elucidate the definition of $\bar{\varepsilon}_e$, for it plays a crucial role in forming a particle-energy balance in the subsequent sections. Notably, $\bar{\varepsilon}_e$ is the average energy of a free electron, *whose absolute energy is less than the excitation potential of the major parent gas species in which it resides.* As a consequence, electrons produced at this energy (and rate) may only *lose* energy via elastic collisions with atoms or *transfer* energy to other electrons (electron-ion collisions are negligible). Further definition of a "W value" comes by dividing the total kinetic energy absorbed by the number of singly charged ions produced, thus:

$$w_{i,a} = \bar{E}_{ion} + \frac{N_{ex}}{N_i}\bar{E}_{ex} + E_{ave} = 1.71(1.82)V_{i,a} \tag{2.8}$$

where $w_{i,a}$ is the total energy expended by the charged particle per ionizing event, i for parent gas a and $V_{i,a}$ is the ionization potential for the gas. The parenthesized quantity pertains to fission fragments and the other, electrons. Among the many generalizations that can be drawn from extensive experimental and theoretical treatments for $w_{i,a}$ that precedes this discussion [16], the most pertinent to modeling devices which utilize charged particle ionization is the fact that the gross quantity, $w_{i,a}$ is only weakly dependent on both energy and of the type of ionization. The fact that its variation is only around 10% over a wide energy is quite remarkable. We will therefore use two fixed values of $w_{i,a}$ and corresponding values of equation blank: one for fission fragments and one for beta particles, and these values only depend on the species of the gas being ionized. These values are summarized in table 2.1. Experimental values are used when available for electrons: in the case of electron ionization, values come from [29] and in the case of fission fragments, values come from [30] (Neon and Argon, experimental) and by direct calculation from equation (2.7) (Helium, Krypton, and Xenon).

Table 2.1 Ionization potentials, $V_{i,a}$, and corresponding $w_{i,a}$ values for fission fragment and high energy electron ionized plasmas.

Gas	Helium	Neon	Argon	Krypton	Xenon
$V_{i,a}$ (eV)	24.6	21.6	15.8	14.0	12.1
$w_{i,a}$ (eV) (Fission Fragments)	44.8	39.2	28.2	25.5	22.0
$w_{i,a}$ (eV) (electrons)	42.3	36.6	26.4	24.2	22.0

2.3 Determining n_e and T_e: Particle and Power Balance

The two main parameters that characterize a separately excited plasma TEC's performance are the electron density, n_e, and electron temperature, T_e (see Chapter 3). In high pressure plasmas, where the main particle and energy gains and losses occur in the bulk, T_e and n_e are solved simultaneously via electron particle and power balance equations. For the plasma under consideration, i.e. one used in the diffusion-mode thermionic energy converter, we assume a uniform bulk density (i.e. a flat profile) and a modified Maxwellian temperature profile for the electrons. This global model is a good approximation for the following reasons:

1. The system dimension is much greater than the sheath dimension, therefore the bulk plasma properties dominate.
2. The mean free path for ion recombination is much less than the ambipolar diffusion length, thus local plasma density variations rely solely on the recombination rate $k_{dr}(T_e)$ according to $n_e \propto (k_{dr})^{-1/2}$
3. The momentum and energy relaxation times for fast electrons are much shorter than the power input time, allowing a steady state density and temperature profile to form.
4. The steady state ionization fraction is sufficiently high so that fast electrons will establish thermal equilibrium at some $T_e > T_a$. Since there is no field force present to increase the energy of the plasma electrons, electron-atom collisions will dominate the electron energy relaxation process.

2.3.1   Particle Balance for n_e

First, we obtain particle balance equations – analogous to the treatment by [16] – observing the main charged particle gain and loss rate mechanisms for a gaseous species a, summarized in Table 2.3 [16]:

$$\frac{d[a^+]}{dt} = f^+ - k_{ic}[a^+][a]^2 - k_{cr}[a^+]n_e^2 - k_{tb}[a^+][a]n_e$$

$$\frac{d[a_2^+]}{dt} = k_{ic}[a^+][a]^2 - k_{dr}[a_2^+]n_e \qquad (2.9)$$

$$n_e = [a^+] + [a_2^+]$$

Table 2.2 Rate constants for pertinent electron production and loss processes. ff and β refers to fission fragments and β-particle respectively.

Production Process	Reaction	Rate Constant (cm⁶/s)	Characteristic Time (s)
Ion Production	$ff/\beta^- + a \rightarrow a^+ + e + ff/\beta^-$	$f^+ = {P_{abs}}/{w_{i,a}}$	$\tau_f \approx 10^{-16}$
Ion conversion	$a^+ + 2a \rightarrow a_2^+ + a$	k_{ic}=(0.6-3.5)x10⁻³¹	$(k_{ic}[a]^2)^{-1} = \tau_{ic}$ $\approx 10^{-9}$

Loss process	Reaction	Rate Constant (cm⁶/s)	Characteristic time (s)
Collisional-radiative	$a^+ + e + e \rightarrow a^* + e$	k_{cr}=4x10⁻⁹$T_e^{-4.5}$(K)	$(k_{cr}n_e^2)^{-1} = \tau_{cr}$ ≈ 1
Three-body	$a^+ + e + a \rightarrow a^* + a$	k_{tb}=(0.5-30)x10⁻²²$T_e^{-2.5}$(K)	$(k_{tb}n_e[a])^{-1} = \tau_{tb}$ ≈ 0.1
Dissociative	$a_2^+ + e \rightarrow a^* + a$	$k_{dr}=\alpha_0 \left(\frac{T_e}{300}\right)^{-\xi} \left(\frac{T_a}{300}\right)^{-\eta}$ (K) $[cm^3/s]$	$(k_{dr}n_e)^{-1} = \tau_{dr}$ $\approx 10^{-5}$

where f^+ [ions cm⁻³ s⁻¹] is the source rate density, P_{abs} is defined by equation (2.5), and $w_{i,a}$ is given by Table 2.1. Again, we emphasize that f^+ represents the rate at which electrons of energy

19

less than the excitation threshold of the parent gas are generated [28]. Due to the strong temperature dependence of collisional-radiative recombination and three body recombination compared to the ion conversion process, the last two terms of the first equation of (2.9) may be neglected. This is applicable even in the limiting case where the electrons are assumed to be in thermal equilibrium with the gas (i.e. $T_e = T_a \approx 2000K$). Using assumption 3, we find

$$\frac{d[a_2^+]}{dt} = \frac{d[a^+]}{dt} = 0 \Rightarrow f^+ = k_{dr}(T_e, T_a)[a_2^+]n_e$$

Substituting $n_e = [a^+] + [a_2^+]$, this forms a quadratic relationship between $[a^+]$ and $[a_2^+]$:

$$-k_{dr}(T_e, T_a)[a_2^+]^2 - k_{dr}(T_e, T_a)[a_2^+][a^+] + f^+ = 0$$

The solution is:

$$[a_2^+] = \frac{[a^+]}{2}(\sqrt{F+1} - 1), \qquad F = \frac{4}{f^+ \tau_{ic}^2 k_{dr}(T_e, T_a)}$$

Considering approximate values $f^+ = 10^{16}$ cm^{-3} s^{-1}, $\tau_{ic} = 10^{-9}$s and $k_{dr,Ar_2^+}(5000K, 1500K) = 3 * 10^{-8}$ cm^{-3} s^{-1}, $F = 3 * 10^9$ and $[a_2^+] \approx 10^4[a^+]$. It is therefore reasonable to assume $n_e \approx [a_2^+]$. Note that this assumption is applicable to all noble gases except for helium, which has an exceptionally low dissociative recombination rate compared to the other noble gases (by at least a factor of 10^3 at room temperature) We are then left with a relationship between the ion production rate due to charged particle energy deposition and the steady state electron density:

$$n_e^2 = \frac{f^+}{k_{dr}(T_e, T_a)} = \frac{f^+}{\alpha_0}\left(\frac{T_a}{300}\right)^\eta \left(\frac{T_e}{300}\right)^\xi \qquad (2.10)$$

Where α_0 is the recombination constant of species a at 300K and ξ and η represent the electron and gas temperature dependence of k_{dr}, tabulated in table 2.3. Of most interest to thermionic energy conversion in nuclear reactors, where T_a is known and T_e may vary based on reactor conditions (i.e. $T_e \neq T_a$), ξ and η values have only recently been experimentally determined [33 – 35] in a limited range of noble gas temperatures (T_a = 300-500K), well below operating temperatures in thermionic energy converters (T_a = 1000-2500K). Of the noble gas temperature dependencies, only neon, argon, and krypton have been determined experimentally, summarized in table 2.3. In the absence of experimental data (i.e. η for helium and xenon), we use the traditional electron temperature dependent form, $k_{dr}(T_e) = \alpha_0 T_e^{-\xi}$. It should be noted that although lack of experimental data for η and ξ at higher T_a may affect the overall precision of the power model, n_e^2 is linearly proportional to f^+, which may be varied over several orders of magnitude of reactor power and have a much more profound effect on n_e and T_e. Regardless, there is an obvious need to experimentally determine $k_{dr}(T_e, T_a)$ at higher T_a (where $T_a \neq T_e$).

Table 2.3 Temperature-dependent dissociative recombination constants.

Gas	$\alpha_0 (\mathrm{cm^3 s^{-1}})$	η	ξ	Temperature Range $T_e \neq T_a$ (K)	Reference
He_2^+	$1.5*10^{-7}$	No data	1	T_a = Unavailable T_e = 300-19000	[16, 37]
Ne_2^+	$1.8*10^{-7}$	0.7	0.42	T_a = 300-500 T_e = 300-6300	[33]
Ar_2^+	$8.10*10^{-7}$	0.86	0.64	T_a = 300-500 T_e = 300-10400	[34]
Kr_2^+	$1.4*10^{-6}$	0.97	0.53	T_a = 300-500 T_e = 300-19000	[35]
Xe_2^+	$8.1*10^{-5}$	No data	0.6	T_a = Unavailable T_e = 300-19000	[16, 37]

2.3.2   Power Balance for T_e

To determine T_e, a power balance equation is be derived via the Boltzmann kinetic equation for an electron species, e, colliding with atomic species, a. This takes the general form:

$$\frac{\partial f(v)}{\partial t} + \frac{\boldsymbol{F}}{m_e} \cdot \frac{\partial f(v)}{\partial \boldsymbol{v}} = I_{ee}(f) + I_{ea}(f) + \sum_i n_a \sigma_{ex,i}(v) v f(v) + \sum_i n_a \sigma_{ion,i}(v) v f(v) + S(f) \tag{2.11}$$

where $f(v)$ is the electron velocity distribution function, $\boldsymbol{F}$ is the acting force on the electron, $I_{ee}(f)$ and $I_{ea}(f)$ are the electron-electron and electron-atom collision integrals [36], the $\sigma_{ex,i}(v)$ and $\sigma_{ion,i}(v)$ are the ith excitation and ionization processes, respectively, $S(f)$ is the sum of electron sources and sinks for electrons contained in the distribution, f. $I_{ee}(f)$ and $I_{ea}(f)$ tend to zero as f approaches a Maxwellian distribution (with $T_e = T_a$). However, due to the mass disparity between electrons and parent gas atoms and long range coulomb interactions between electrons, the electrons tend to establish thermal equilibrium amongst themselves much more rapidly than with the parent gas atoms where $T_e > T_a$ under assumption 4.

At this point, it is appropriate to make simplifications for the conditions expected of low density, reactor produced, charged particle ionized plasmas. First, from assumption 3, we may assume a steady state ($\frac{\partial f(v)}{\partial t} = 0$), and since these electrons are generated only by non-electric forces (i.e. energetic charged particles) we may take $\boldsymbol{F} = 0$ and we see that the LHS of the equation vanishes. Then, from Platzman[28], by definition, electrons from source f^+ are produced below the excitation threshold and may neither further ionize nor excite the medium surrounding it: this leads to $\sigma_{ex,i}(v) = \sigma_{ion,i}(v) = 0$. We see:

$$S(f) + I_{ea}(f) + I_{ee}(f) = 0 \tag{2.12}$$

where, under assumption 4, we may take $I_{ee}(f) = 0$. By multiplying each term of (2.12) by the average energy gained or lost during the process, then integrating over the electron velocity space, we obtain a power balance equation as a function of T_e, assuming the form:

$$f^+ E_{ave} - n_e^2 k_{dr}(T_a, T_e) T_e = -n_e \int_0^{v_{\Delta\varepsilon}} \frac{1}{2} m_e v^2 I_{ea}(f) 4\pi v^2 dv \tag{2.13}$$

Here, m_e is the electron mass [kg], E_{ave} is the defined by equation (2.8), $\Delta\varepsilon$ is the energy of the first excited state of the noble gas [J] and from [36]

$$I_{ea}(f) = \frac{n_a m_e}{M} \frac{\partial}{v^2 \partial v} \left[v^4 \sigma_{el}(v) \left(f + \frac{T_a}{m_e v} \frac{\partial f}{\partial v} \right) \right], \qquad \varepsilon_e \gg T_a$$

where M is the mass of the parent atom of species a (kg), $\sigma_{el}(v)$ is the electron-atom elastic momentum transfer cross section [m²] and

$$f(v) = \frac{1}{C(T_e)} \left(\frac{m_e}{2\pi T_e} \right)^{3/2} \left\{ \exp\left(-\frac{m_e v^2}{2T_e} \right) - \exp\left(-\frac{\Delta\varepsilon}{T_e} \right) \right\}, \qquad \int_0^{v_{\Delta\varepsilon}} 4\pi v^2 f(v) dv = C(T_e)$$

Integrating (2.13) by parts,

$$n_e \int_0^{v_{\Delta\varepsilon}} \frac{1}{2} m_e v^2 \frac{n_a m_e}{M} \frac{\partial}{v^2 \partial v} \left[v^4 \sigma_{el}(v) \left(f + \frac{T_a}{m_e v} \frac{\partial f}{\partial v} \right) \right] 4\pi v^2 dv$$
$$= \frac{2\pi n_a n_e m_e^2}{M} \left[1 - \frac{T_a}{T_e} \left\{ 1 + \exp\left(-\frac{\Delta\varepsilon}{T_e} \right) \right\} \right] \left([v^6 \sigma_{el}(v) f(v)]_0^{v_{\Delta\varepsilon}} \right.$$
$$\left. + 2 \int_0^{v_{\Delta\varepsilon}} v^5 \sigma_{el}(v) f(v) dv \right)$$

Given the boundary condition $f(v_{\Delta\varepsilon}) = 0$, this leaves the exact form:

$$-n_e \int_0^{v_{\Delta\varepsilon}} \frac{1}{2} m_e v^2 I_{ea}(f) 4\pi v^2 dv = \frac{n_a n_e m_e^2}{M} \left[1 - \frac{T_a}{T_e} \left\{ 1 + \exp\left(-\frac{\Delta\varepsilon}{T_e} \right) \right\} \right] \langle v^3 \sigma_{el} \rangle$$

And we obtain by inserting this result into (2.13) and using (2.12):

$$f^+ (E_{ave} - kT_e) = \frac{n_a n_e m_e^2}{M} \left[1 - \frac{T_a}{T_e} \left\{ 1 + \exp\left(-\frac{\Delta\varepsilon}{T_e} \right) \right\} \right] \langle v^3 \sigma_{el} \rangle$$

$$f^+ = \frac{\frac{n_a n_e m_e^2}{M} \left[1 - \frac{T_a}{T_e} \left\{ 1 + \exp\left(-\frac{\Delta\varepsilon}{T_e} \right) \right\} \right] \langle v^3 \sigma_{el} \rangle}{(E_{ave} - kT_e)} \tag{2.14}$$

Often, for low electron temperatures where $T_e < 30,000K$ this may be simplified to a more compact form where the distribution function is approximated as Maxwellian:

$$f^+ = n_a n_e \frac{\frac{m_e^2}{M} \langle v^3 \sigma_{el} \rangle \left(1 - \frac{T_a}{T_e} \right)}{(E_{ave} - kT_e)} \tag{2.15}$$

22

where $\langle v^3\sigma_{el}\rangle = \int_0^{v_{\Delta\varepsilon}} 4\pi v^2 * v^3\sigma_{el} * f(v)dv$. For typical operating temperatures in thermionic energy converters, $T_a = 1000K = 8.6 * 10^{-2}eV$ may be set as an appropriate lower limit for $T_{a,ave}$ in thermionic energy converters ,which generally exceed $1500K$. The upper limit electron velocity is constrained by the first excited state of the atom considered and depends on the noble gas, allowing variation of a factor of two, $v_{\Delta\varepsilon} \approx (1.7 - 2.5) * 10^6$ ms^{-1}. The approximate value of E_{ave} is $0.31V_{i,a}$ from Platzman [28] and ranges from 4-6 eV for noble gases (calculated from Table 2.1). Equation (2.15) may be expressed in terms of P_{abs} by substituting the relationship between f^+ and n_e from the charged particle balance equation (2.10) to yield:

$$P_{abs} = w_{i,a}\frac{\left(\frac{T_e}{300}\right)^\xi \left(\frac{T_a}{300}\right)^\eta}{\alpha_0}\left(\frac{n_a\frac{m_e^2}{M}\langle v^3\sigma_{el}\rangle\left(1 - \frac{T_a}{T_e}\right)}{E_{ave} - kT_e}\right)^2 \tag{2.16}$$

This gives a direct connection between electron temperature and reactor power, which is proportional to f^+. Specifically, for nuclear reactors, where the thermal neutron flux ϕ_{th} is used to reflect reactor power, we may insert the simplified form of equation (2.5), defining some factor β_{mat}, a property of the fuel composition only, such that $P_{abs} = \phi_{th}\sigma_{th}\beta_{mat}$. Then we see, finally:

$$\phi_{th} = \frac{w_{i,a}\left(\frac{T_e}{300}\right)^\xi \left(\frac{T_a}{300}\right)^\eta}{\sigma_{th}\beta_{mat}\alpha_0}\left(\frac{n_a\frac{m_e^2}{M}\langle v^3\sigma_{el}\rangle\left(1 - \frac{T_a}{T_e}\right)}{E_{ave} - kT_e}\right)^2 \tag{2.17}$$

It should be noted that since β_{mat} depends linearly on n_a (see equation (2.5)), the flux required to maintain a constant electron temperature (assuming a constant gas temperature, T_a) varies monotonically with gas density. As an example, equation 2.16 is plotted in Figure 2.3 for argon and xenon at 90 torr and T_a = 300K; cross sections were extracted from [36] and recombination rates, from [16, 34]. Evident in the characteristic curve for xenon is the Ramsauer minimum, which occurs at a higher electron temperature than that of argon (0.6 eV for xenon and 0.2 eV for argon). Also of note is that though the elastic momentum transfer cross section of xenon is, in general, greater than argon's, its atomic mass is almost three times greater: this leads to less electron thermalization and a correspondingly higher electron temperature in xenon for a given thermal neutron flux.
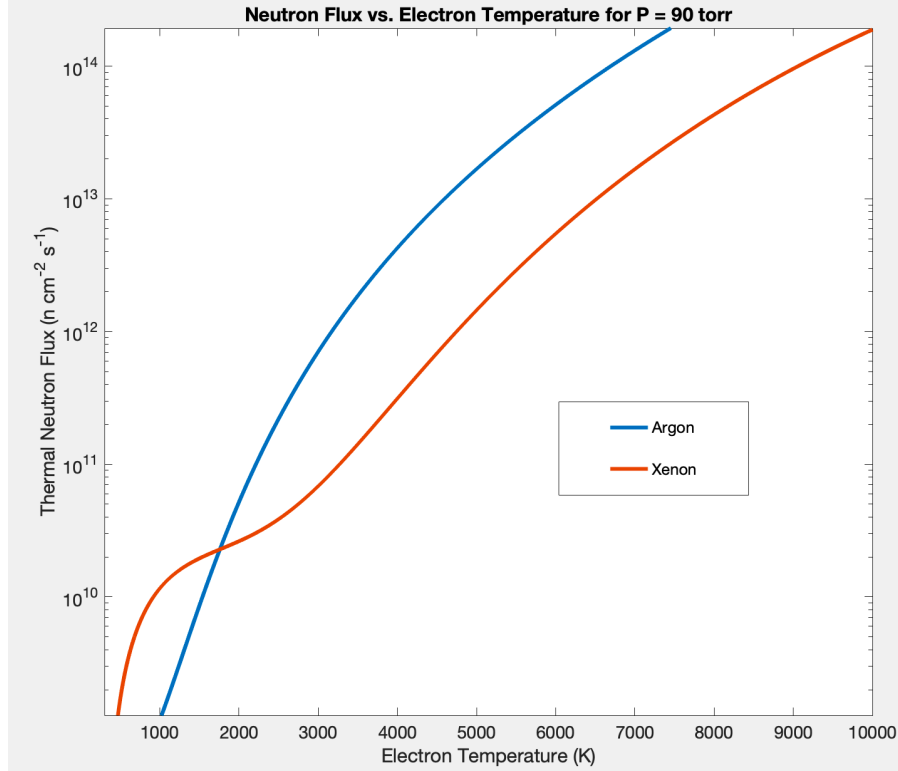
Figure 2.3 Sample plot of thermal neutron flux vs. electron temperature for argon and xenon at 90 torr and 300K.

Once T_e is determined at a given reactor power, its value (along with T_a) may be inserted back into (2.10) to obtain n_e. The preceding analysis is only one application of the power balance equation to charged particle ionized plasmas, specifically nuclear reactor generated plasma systems where the ionization source is correlated with reactor thermal flux ϕ_{th}. The general methodology of determining T_e via the power balance equation for high pressure, recombination-dominated plasmas may be adapted to systems where other ionization sources (e.g. radioactive decay, penning ionization, etc.) and electromagnetic forces are present (e.g. capacitive/inductive RF, laser, etc.) in a straightforward manner.

2.4 Comparison of Charged Particle and Field Ionized Plasmas

The principal difference between *charged particle* and *field* ionized plasmas (e.g. glow-discharge, RF, etc.) is that, in the case of field ionization, the power source (of the field) directly couples to the swarm electrons, using them to sustain ionization. Starting again with a particle balance, we may modify the results obtained in (2.10) by taking the ionization rate per unit volume $f^+ \rightarrow n_e n_a K_{iz}(T_e)$ (assuming $[a^+] = 0$) and we see

$$n_e = \frac{n_a K_{iz}(T_e)}{k_{dr}(T_e, T_a)} = n_a K_{iz}(T_e) \frac{T_e^{\xi} T_a^{\eta}}{\alpha_0}$$

$K_{iz}(T_e)$ can be crudely approximated as [37]

$$K_{iz}(T_e) \approx K_{iz0}\exp\left(-\frac{E_{iz}}{kT_e}\right)$$

which gives the electron temperature dependence on ionization fraction:

$$\frac{n_e}{n_a} = K_{iz0} \frac{\left(\frac{T_e}{300}\right)^\xi \left(\frac{T_a}{300}\right)^\eta}{\alpha_0} \exp\left(-\frac{E_{iz}}{kT_e}\right) \tag{2.18}$$

where k=8.617x10^{-5} eV K^{-1} and K_{iz0} [m^3 s^{-1}] is the pre-exponential ionization. Since electric fields are now the ionizing mechanism (via acceleration of electrons), there is no boundary condition which precludes the electron's energy from exceeding the excitation and ionization potentials: in fact, this is required to obtain a non-zero ionization rate constant, which by definition is $K_{iz}(T_e) = \langle v\sigma_{iz} \rangle = \int_0^\infty 4\pi v^2 * v\sigma_{iz} * f(v)dv$. For noble gases, where $E_{iz} > 15$eV, $\frac{n_e}{n_a} > 10^{-8}$ is not realized for $T_e < 1$eV. Figure 2.4 compares ionization fractions for argon as a function of T_e for charged particle and field ionized plasmas for $T_e \leq 1$eV.
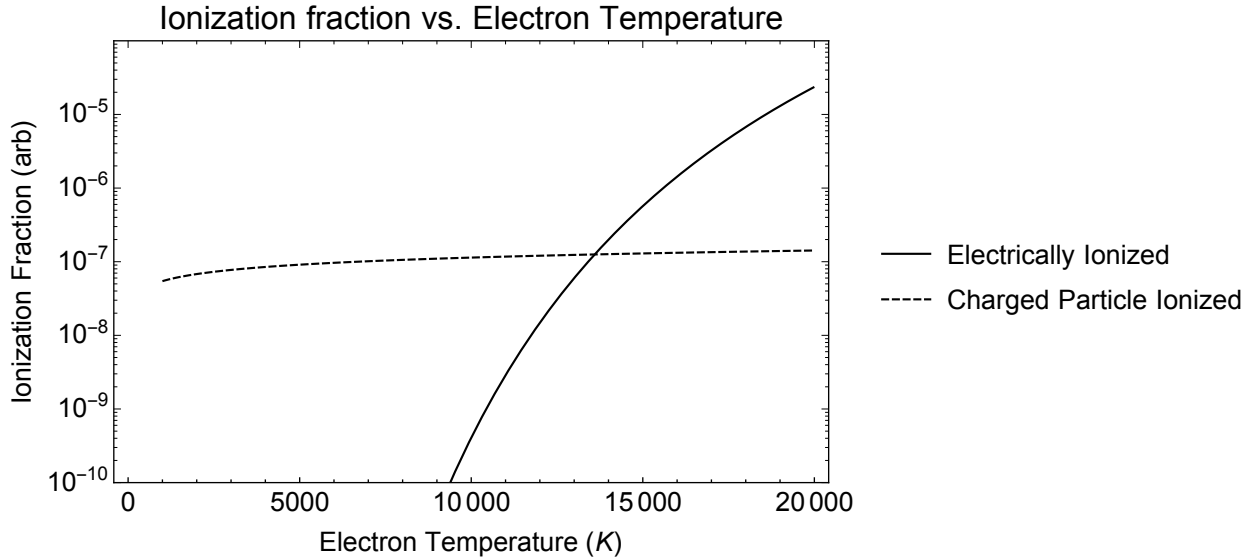
Figure 2.4 Temperature-ionization fraction relationships for charged particle ionized plasmas and field ionized plasmas.

To find the electron temperature, a power balance yields:

$$P_{aux} = n_a^2\left(\frac{n_e}{n_a}\right)\left(\frac{m_e^2}{M}\left(1 - \frac{T_a}{T_e}\right) < v^3\sigma_{el}(v) > + K_{ex,i}(T_e)E_{ex,i} + E_{iz,i}K_{iz,i}(T_e)\right) \tag{2.19}$$
$$+ n_a^2\left(\frac{n_e}{n_a}\right)^2 \alpha_0 \left(\frac{T_e}{300}\right)^{-\xi}\left(\frac{T_a}{300}\right)^{-\eta} T_e$$

and we note that, in most cases, the recombination losses are insignificant compared to the other terms and may be neglected. As an example, in a 0.5 atm argon discharge ($n_a \approx 10^{19}$ cm^{-3}) at room temperature (T_a = 300K), n_e=10^{11}-10^{12} cm^{-3} requires P_{aux} = 0.3-7 W cm^{-3} whereas the equivalent P_{abs} range for a charged particle ionized plasma will yield n_e = (1-5) x 10^{12} cm^{-3} or roughly a half to full order of magnitude higher degree of ionization. The difference is that, in the case of the field ionized plasma, the electron temperature is much higher with less variation, from 10600K – 11950K, than that of the charged particle ionized plasma, which is roughly lower by a factor of 4 and ranges from 2700K – 4400K.

We see in general for high pressure plasmas of low power density (P_{abs} < 100 W cm^{-3}), raising the input power in the form of charged particles tends to increase the electron temperature more than the degree of ionization, in contrast to the same raise in field input power, P_{aux}. Physically, this is due to the difference in loss mechanisms which dominate in each type of plasma. Charged particle ignited plasmas owe their electron energy relaxation entirely to elastic collisions, whose rate varies smoothly across the electron temperatures of interest (2x10^3-2x10^4 K). Field ionized plasmas, on the other hand, see sharp increases in energy relaxation with an increase of T_e as more excitation collisions and, more importantly, ionization collisions become energetically possible beyond T_e = 10^4 K. Because of the sharp increase in power loss with relatively small increases of T_e (beyond 10^4 K), high pressure plasmas see little increase in temperature without a dramatic increase in power input (orders of magnitude) – more modest power increases are manifested in the increase of the degree of ionization, which increases $\propto$ $\exp\left(-\frac{E_{iz}}{kT_e}\right)$. This distinction between charged particle ionized and field ionized plasmas has broader implications which may be of significant interest and/or utility to other disciplines within low temperature plasma research.

2.5 T_e Calculation Comparison to "The GM study"

The GM study attempted to calculate the electron temperature by performing a swarm electron power balance [14]. More specifically, the "electron swarm" pertains to the portion of plasma electrons that have thermalized with themselves and/or the parent gas; this is in contrast to "plasma electrons" which refer to the entire system of electrons that are liberated from their parent atoms. The basic methods used were similar to the analysis given above in that they used a detailed energy balance to determine T_e. However, they were conceptually flawed in that their model does not conserve energy and number of particles simultaneously, neglecting both particle and energy loss due to dissociative recombination. This dramatically changed the way the electron power balance was framed.

Essentially, the power balance was applied to the swarm electron subsystem only, rather than the entire subthreshold (i.e. where $\varepsilon_e < \Delta\varepsilon$) electron subsystem, which comprises of fast electrons *and* swarm electrons. [14] identified the electron swarm energy *gain* as the energy transferred from fast electrons to the swarm electrons as they slowed down via electron-electron collisions then equated this value to the energy *loss* of the swarm electrons to the surrounding gas and ions via elastic and electron-ion collisions, respectively. Figure 2.5 summarizes the power balance scheme used in the GM study with a neon:argon (1:10^{-4}) mixture.
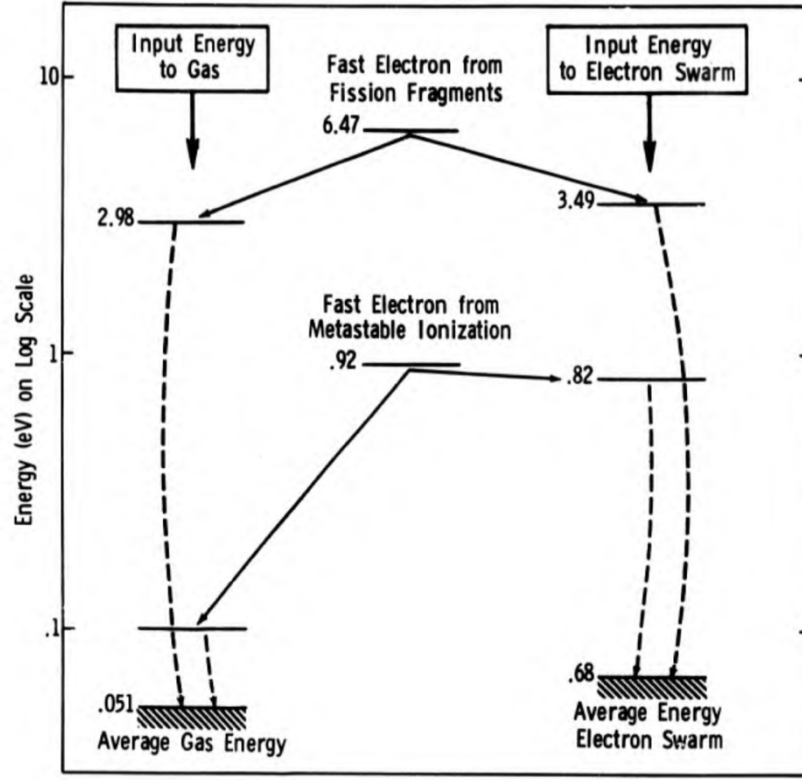
Figure 2.5 Schematic of energy balance for neon:argon (1:10^{-4}) mixture from [14].

Here, the energy loss rate from fast electrons in the subthreshold region is categorized into two distinct groups: one from fast electrons to gaseous atoms and one from fast electrons to swarm electrons (via elastic momentum transfer), expressed as:

$$\frac{d\varepsilon}{dt} = -\left(\frac{2m_e}{M} n_a v \sigma_{ea}(v)(\varepsilon - \bar{\varepsilon}_a) + n_e v \sigma_{ee}(v)(\varepsilon - \bar{\varepsilon}_e)\right) \tag{2.20}$$

Where ε is the energy of the fast electron, $v = \sqrt{\frac{2\varepsilon}{m_e}}$ is the corresponding velocity of the fast electron, and $\bar{\varepsilon}_a$ and $\bar{\varepsilon}_e$ are the average gaseous atom and swarm electron energies, respectively. As the RHS of (2.20) is a function of fast electron energy only, an integral relation between the fast electron energy and time appears:

$$-\int_{\varepsilon_i}^{\varepsilon} \frac{d\varepsilon}{\left(\frac{2m_e}{M} n_a v \sigma_{ea}(v)(\varepsilon - \bar{\varepsilon}_a) + n_e v \sigma_{ee}(v)(\varepsilon - \bar{\varepsilon}_e)\right)} = t$$

Where ε_i is the initial energy of the fast electron (e.g. $\varepsilon_i = 0.31 E_{iz,i}$ for fast electrons resulting from fission fragment excitation). Setting $\varepsilon = \bar{\varepsilon}_e$ we obtain the total slowing down time of the fast electron to some thermal energy, $\bar{\varepsilon}_e$. By inserting the time dependent expression $\varepsilon(t)$ into

27

the second term on the right hand side of (2.20) then integrating over the slowing down time of the fast electron, the fast electron's total energy loss to the swarm electrons is obtained. Then, the total fast electron energy loss rate and subsequent swarm electron energy gain rate may be trivially calculated by multiplying the electron's total energy loss by source rate, f^+. In order to determine $\bar{\varepsilon_e}$ and therefore T_e by the relation $\frac{3}{2}kT_e = \bar{\varepsilon_e}$, the integration must carried out over incremental values of $\bar{\varepsilon_e}$ until the energy gain rate of the swarm is equal to the energy loss rate of the swarm. The energy loss rate of the swarm electrons is readily calculated since the total number of swarm electrons is known experimentally and its distribution is assumed Maxwellian.

The most important conceptual error to point out in the analysis above lies in the treatment of electron-electron collisions between fast electrons and swarm electrons. Ultimately, the entire system of subthreshold electrons under consideration is the sum of fast electrons and swarm electrons; at steady state, this system must conserve both energy and number of particles. Though energy may be transferred *between* fast electrons and swarm electrons, this exchange is *within* the electron system and therefore does not contribute to the total power gained or lost *by* the system. Thus, electron-electron collisions play no role in the total power balance and corresponding electron energy relaxation; this relaxation occurs only by energy and/or particle transfer out of the electron subsystem. As is summarized by (2.15) these relaxation mechanisms are momentum transfer with neutral atoms and dissociative recombination with molecular ions.

Ultimately, the analysis from [14] underestimates the energy input rate into the electron subsystem by erroneously subtracting out the energy lost by momentum transfer between fast electrons and gas atoms; this generally acts to reduce the resulting electron temperature. However, by also neglecting energy losses due to recombination, the degree to which electron temperature is underestimated is lessened. The particle and energy balance for penning gas mixtures is much more complicated, and its assessment is outside the scope of this work. Later, we analyze the experimental thermionic output current-voltage curves from [14] (Vol. II), and show beyond reasonable doubt that T_e was underestimated.

Chapter 3: Underlying Physics of Thermionic Energy Conversion

3.1 Thermionic Emission

For single atoms held at the minimum physical temperature, 0K, electrons will occupy the lowest energy states available to them. Being fermions – thus obeying the Pauli Exclusion Principle – they will fill these discrete energy levels sequentially: from minimum to maximum potential energy. This concept is illustrated in figure 3.1a. Beyond single atom systems, crystalline solids comprised of large ensembles of atoms and correspondingly densely packed energy levels (10^{22} cm^{-3}) must also obey the Pauli exclusion principle. Where energy levels in single atoms differ by up to a few eV within shells (i.e. principle quantum number $n = 1, 2, 3, ...$), energy levels in crystalline solids differ by an order of 10^{-22} eV and are compressed so closely together (in energy interval) that they form a continuous energy band. Therefore, when discussing energy states in crystalline solids, we describe energy *bands* as in Figure 3.1b rather than energy *levels* as in single atoms or gaseous state matter. The highest energy state an electron may occupy at 0K in a crystalline solid is defined as the Fermi energy (eV) shown also in Figure 3.1b and is specific to every material, its crystallographic orientation, and many other factors.
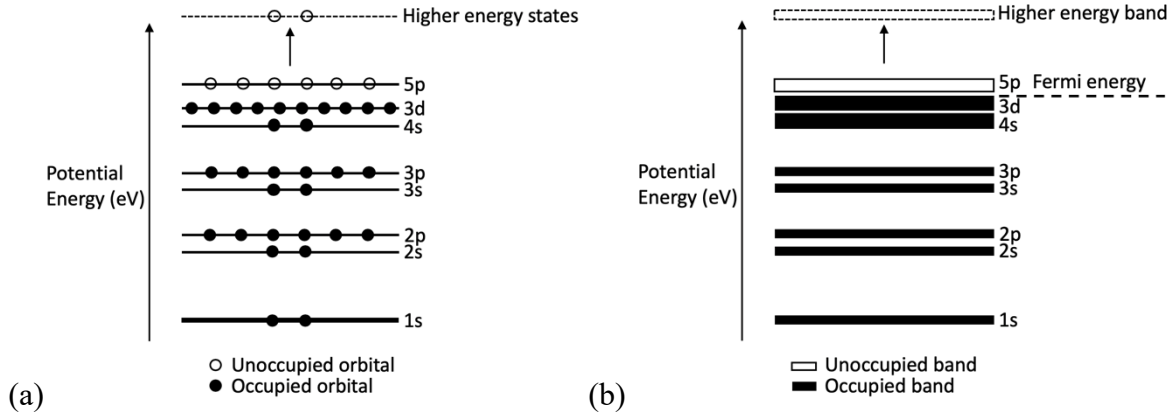
Figure 3.1 (a) Orbital energy diagram of a Zn atom at 0K along the equivalent energy band diagram for solid crystalline Zn (b).

The Fermi energy is essentially a physical abstraction, as it only applies to non-interacting fermions that have no kinetic energy in a system held at 0K. At temperatures above 0K, the Fermi *level*, analogous to the Fermi energy, is a more useful variable – it accounts for fermion interaction, kinetic energy, and physical temperature. We will describe phenomena with respect to the Fermi level from this point onward. It is possible for electrons possessing an initial potential energy, ϵ, at or near the Fermi level, μ, to occupy higher energy bands depending on the temperature of the system, T. This is represented mathematically by the Fermi-Dirac distribution function:

$$f(\epsilon) = \frac{1}{1 + \exp\left(\frac{\epsilon - \mu}{kT}\right)} \tag{3.1}$$

where ϵ is the energy of the electron [eV], μ is the Fermi level [eV], k is the Boltzmann constant [eV K^{-1}] and T is the temperature [K]. The Fermi-Dirac distribution function is plotted in Figure 3.2a for $\mu = 1$eV. This concept can be applied to a system of electrons in order to obtain the electron energy distribution function (EEDF). By multiplying the Fermi-Dirac distribution function by the density of electron orbital energy states (stated without proof):

$$D(\epsilon) = 4\pi \left(\frac{2m_e}{h^2}\right)^{3/2} \sqrt{\epsilon} \tag{3.2}$$

where m_e is the electron mass [eV/c^2], h is Planck's constant [eV s], and ϵ is the orbital energy, we plot this, product $D(\epsilon) f(\epsilon)$ alongside the Fermi-Dirac distribution function in figure 3.2b.

(a)

(b)
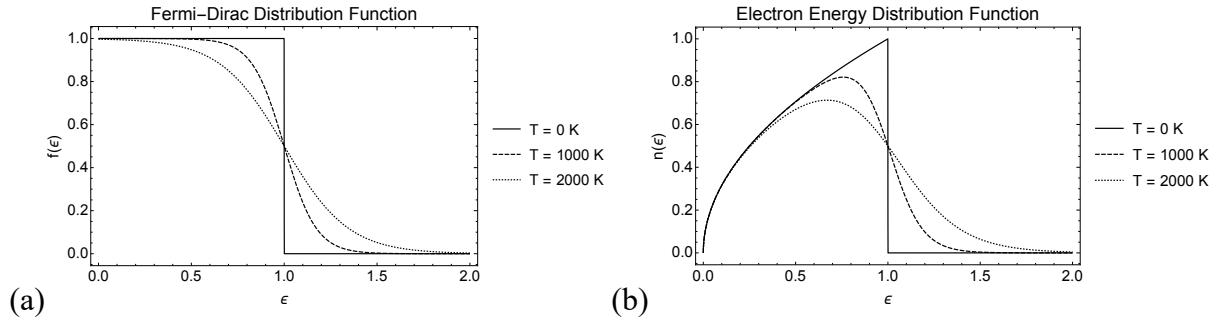
Figure 3.2 (a) the Fermi-Dirac distribution function, $f(\epsilon)$, and corresponding (b) Electron energy distribution function, $D(\epsilon)f(\epsilon)$, for $\mu = 1$eV at various temperatures. For $\epsilon > \mu$ in an electrical conductor, electrons are said to occupy the *conduction* band, where they may migrate freely between atoms in a crystal lattice.

The behavior of valence electrons (i.e. electrons nearest in energy to the Fermi level) is what most strongly influences physical properties of materials such as electrical and thermal conductivity. Electrons below the Fermi level are said to occupy the "valence band", where they are still bound to their respective atom, while electrons above the Fermi level occupy the "conduction band", where they may freely move across many atoms throughout the material. However, referring back to Figure 3.1b, we still observe discrete "band gaps" between energy bands; the transition between valence and conduction bands is not necessarily continuous. In fact, this is how conductors, semiconductors, and insulators are differentiated. Figure 3.3 illustrates energy band diagrams for the three materials. Band gaps effectively reduce the total number of conduction band electrons in a material for a given temperature and Fermi level since there is a threshold energy, i.e. the band gap width, that the electron must possess in order to transition from the valence band to the conduction band. In electrical insulators such as diamond, band gaps may exceed 5.5 eV, and there is no amount of heat energy absorption it can withstand to migrate electrons into the conduction band without vaporizing the material itself.
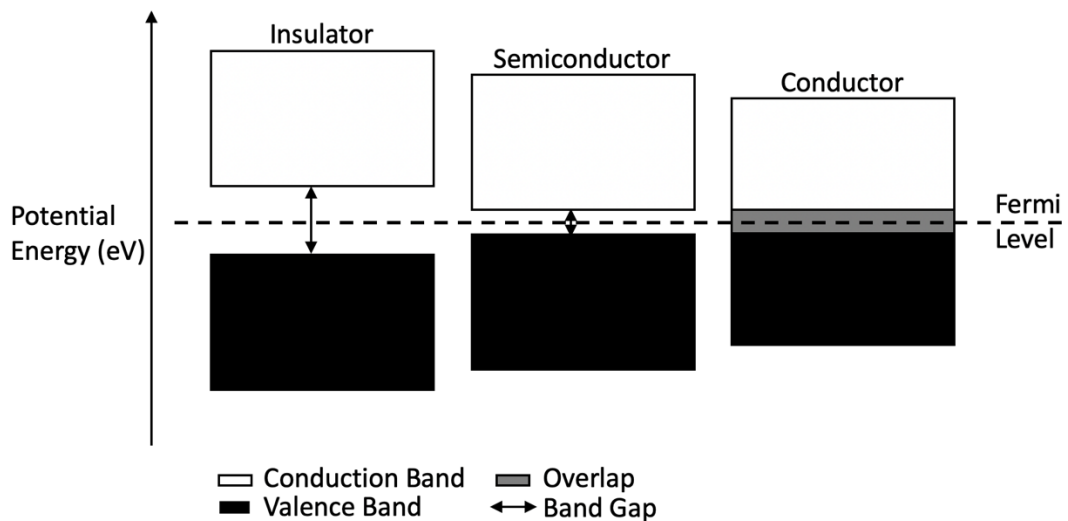
Figure 3.3 Simple Band Diagrams for an insulator, semiconductor and conductor. Typical band gap widths are > 4 eV, 0.2-4 eV, and < 0.2eV for insulators, semiconductors and conductors, respectively.

Most conductors, on the other hand, have little to no band gap width, and therefore readily permit electrons into the conduction band at room temperature. As the only practicable TEC devices have used refractory metals (electrical conductors) for thermionic emission, we will confine further analysis to that of conductors.

For conductors heated to any extent beyond 0K, their valence electrons will begin occupying the conduction band, becoming available for subsequent thermionic emission. Electrons sufficiently energetic to overcome the potential barrier which confines it to the surface will escape into vacuum: this is thermionic emission. A material's work function, often denoted as ϕ (eV), quantifies the propensity of an electron of a certain material to emit thermionically. Thus, the work function is defined as the minimum thermodynamic work required to move an electron from the surface of a material to a point immediately outside of that material in vacuum. Physically, thermionic emission results when an electron's thermal energy exceeds the electric potential energy that confines it to the material's surface. Therefore, with an a priori knowledge of the electric potential near the surface, we could calculate emission properties at any given temperature. But a material's electric potential near the surface, along with the many factors that affect it, make its evaluation prohibitively complex: determining emission properties by an electrostatics approach is intractable.

Instead, we turn to a thermodynamic approach. Consider thermionic emission from a metal surface into vacuum. Immediately after thermionic emission, the electron experiences an image charge force, depicted in figure 3.4, that draws the electron back to the surface. Then, for a system where there is no net energy or particle transfer, the emitted electrons are in thermodynamic equilibrium with the returning electrons. We may therefore infer the rate of electrons leaving the surface by calculating the subsequent random electron current density entering the surface from vacuum. Assuming a Maxwellian distribution of electrons in thermodynamic equilibrium with the conduction band electrons at the surface, and noting the definition of the random electron current density $J = \frac{1}{4} e n \bar{v}$ [C m^{-2} s^{-1}],where e is the electron charge [C], n is the electron density [m^{-3}] and $\bar{v}$ is the average velocity [m s^{-1}], we integrate $vf(\epsilon)D(\epsilon)$ over the entire velocity space:
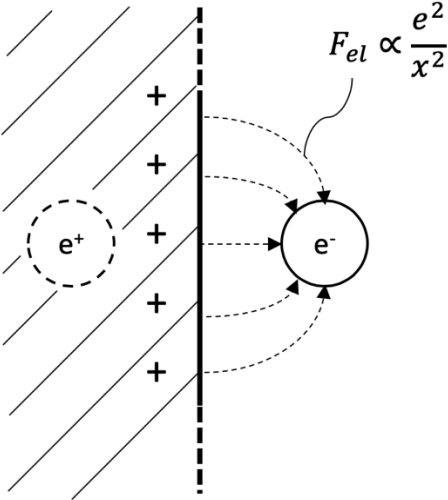
Figure 3.4 The image charge force on a free electron just outside of a conducting surface.

$$J_{th} = 2e \exp\left(\frac{\mu}{kT_E}\right)\left(\frac{m_e}{h}\right)^3 \int_0^{2\pi} d\phi \int_0^{\pi/2} \sin\theta \, d\theta \int_0^{\infty} \cos\theta v^3 \exp\left(\frac{-m_e v^2}{2kT_E}\right) dv$$

$$I_{th} = A_E \frac{4\pi e m_e k^2}{h^3} T_E^2 \exp\left(-\frac{\phi_E}{kT_E}\right) \qquad (3.3)$$

where J_E is the electron current density [C s^{-1}m^{-2}] e is the electron charge [C], μ is the Fermi level of the emitter [J], k is the Boltzmann constant [m^2 kg s^{-2} K^{-1}] m_e is the electron mass [kg], h is Planck's constant [m^2 kg s^{-1}], T_E is the temperature of the emitting surface [K] and ϕ_E is the material's work function [J]. Note that we used a simplified expression for equation (3.2) $f(\epsilon) = \exp\left(\frac{\mu-\epsilon}{kT}\right)$ for $\epsilon - \mu \gg kT$. In general:

$$\phi_E = V - \mu$$

Where V is the vacuum level energy [J] and represents the electrostatic energy due to the presence of an electron. In defining the system above to be in thermodynamic equilibrium, i.e. there is no net energy or charge flow, $V = 0$ and we see $\phi_E = -\mu$. Equation 3.3 is also known as the Richardson-Dushman equation and is plotted in figure 3.5. It represents the maximum emission current for a given emitter temperature and work function. Further reading on the subject matter can be found in [38], which offers a good introductory treatment of thermionic emission, and [39] for a more thorough treatment. We will now develop energy conversion principles off thermionic emission in the following section.
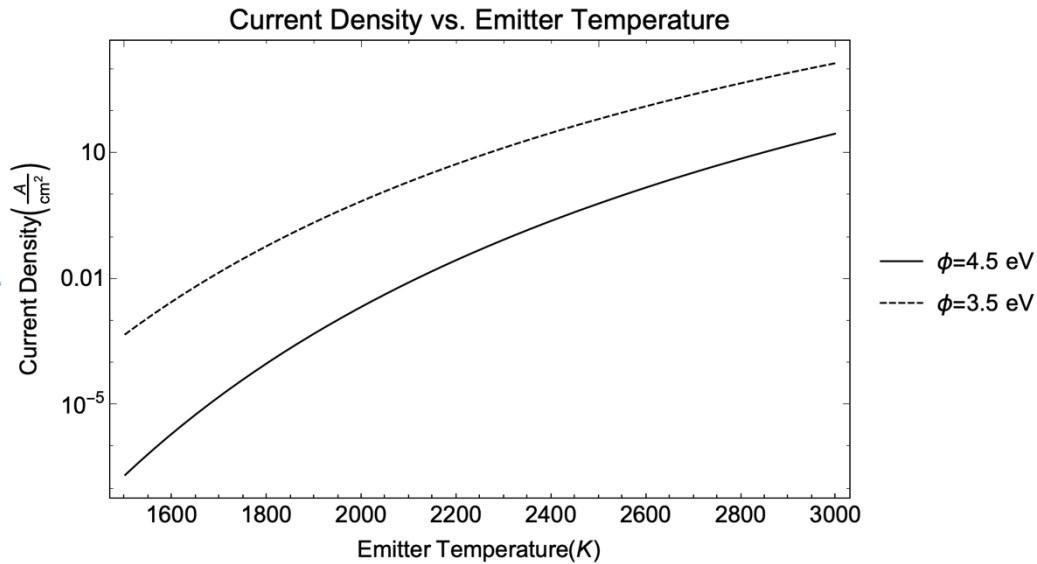
Figure 3.5 Richardson-Dushman Equation. For reference, $\phi_E = 4.5$ eV is a typical work function for a refractory metal, such as W and $\phi_E = 3.5$ eV is the work function of the refractory ceramic, ZrC.

3.3 Thermionic Energy Conversion

3.3.1 Basic Operation

TECs have been studied for over a century, with the first practical devices appearing in the 1950's. The operating principle behind a TEC is thermionic emission (discussed previously): an effect seen when a material of work function (ϕ_E) is heated to a sufficiently high temperature (T_E) to begin emitting electrons. In the simplest case, where we neglect space charge effects, if the emitted electrons traverse a gap to some collecting material of lower work function (ϕ_C) and temperature (T_C) they will impart electrical energy on the collector equal to $\phi_E - \phi_C$, which would be dissipated as heat in the absence of an applied voltage, V_{out} and external load, R_L. However, if we introduce some applied voltage and external load, we may capture the electrical energy from the emitted electrons and use this energy to drive electrical power through the load; this process is illustrated in Figure 3.6 by a simple TEC schematic. In the schematic, the x-direction corresponds to the spatial coordinate between the emitter (left) and collector (right) and the y-direction corresponds to the electron's spatially dependent potential energy, called the electron motive. Analogous to the electric potential V, whose negative spatial gradient is the electric field $(-\nabla V = \vec{E})$, the negative spatial gradient of the electron motive is the directional force experienced by an electron as it traverses across the interelectrode space. However, the *electron motive* in the interelectrode space should not be confused with the *electric potential*, as they are opposite from one another; succinctly, the gradient of the electron motive is a measure of the force experienced by an electron whereas the gradient of the electric potential is a measure of the local electric field.

For clarity, figure 3.6 shows the motive diagram step-by-step for the case when the diode is producing maximum power. First, the electron is heated to a sufficient energy so that it may overcome the emitter work function; the electron does work on this potential. As there is an applied voltage at the collector equal to that of the contact potential, $\phi_E - \phi_C$, the electron experiences no force as it traverses the gap; no work is done in this case. Then, the electron recombines at the collector where it does work on the applied (negative) voltage, V_{out}, and the collector work function does work on the electron as the electron falls back to the surface. Thus, the net work done by the electron on the emitter and collector work functions is entirely converted into potential energy, whose power is equal to $P_{out} = I_{th}V_{out}$ [W]. This useful power is used to drive some electrical load R_L. To analogize, the TEC cycle is akin to the Rankine cycle, where the electrons are the working fluid. Heat is supplied to an emitter, which "boils" electrons off at high temperatures, then these electrons "condense" as they impart their energy to the collector.

One can reasonably infer how the power output of the device is affected for $V_{out} \neq \phi_E - \phi_C$. For $V_{out} < \phi_E - \phi_C$, the electron motive between the emitter and collector would have a downward slope, therefore the emitted electrons would be accelerated toward the collector. The additional energy gained by the electron is kinetic and is dissipated as heat at the collector, therefore does not contribute to the electrical output; this lowers the power output by the reduction of V_{out}. For $V_{out} > \phi_E - \phi_C$ and given the Maxwellian nature of thermionically emitted electrons, the electron motive between the emitter and collector would have an upward slope, and the emitted electrons would be decelerated as they traversed the gap. Though doing work on a larger electric potential, only the fraction of electrons with the energy to overcome the

potential will transmit to the collector; as will be seen later, this fraction falls $\propto \exp\left(-\frac{V_{out}-(\phi_E-\phi_C)}{T_E}\right)$ and the power output is therefore lowered by the reduction of I_{th}.
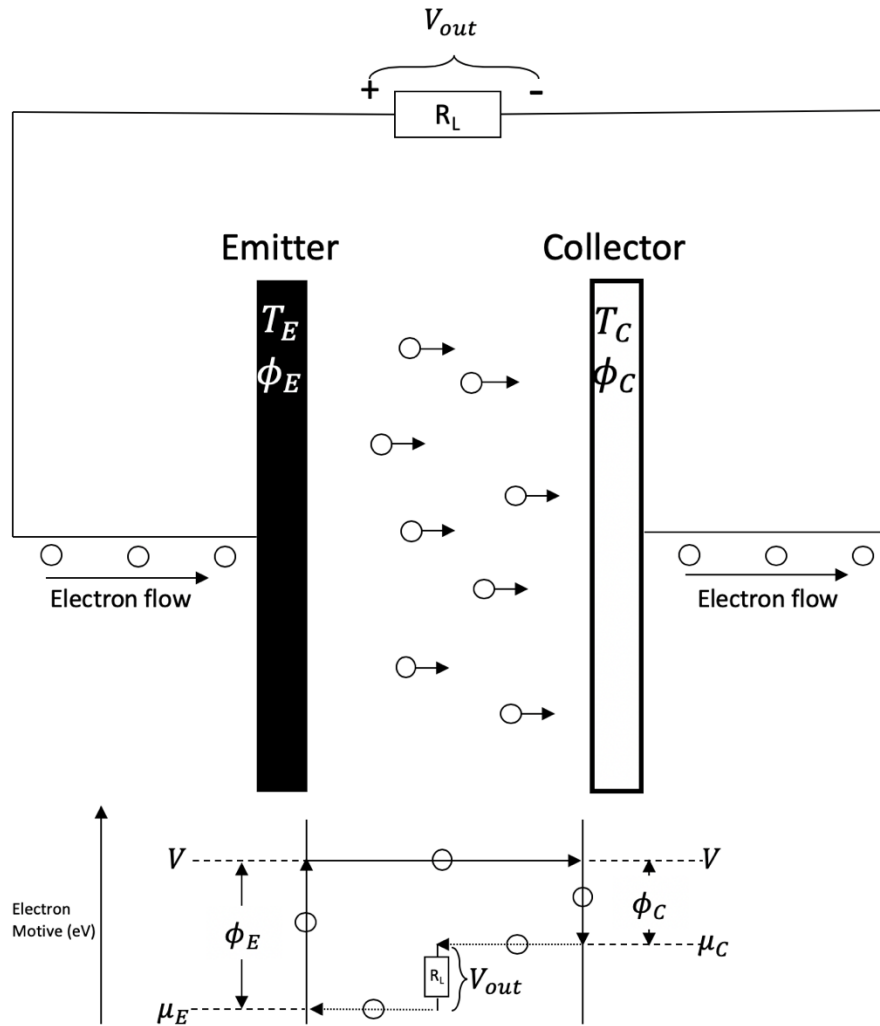
Figure 3.6 A TEC cycle schematic. Above is a physical representation of TEC with a corresponding electron motive diagram below.

3.3.2   Ideal Power and Efficiency of TEC

Now, having established a general basis for an ideal TEC's principles of operation, it is useful to derive ideal power output, efficiency and therefore performance characteristics. Starting with an engineering definition of electrical power [W]:

$$P_{el,ideal} = IV_{out} = JAV_{out}$$

where J is the current density [C m^2], A is the area perpendicular to the current flow [m^2], and V_{out} is the output voltage. We substitute equation 3.3 and the ideal output voltage to obtain the ideal output power as a function of T_E:

$$P_{el,ideal} = J_{th}A_E(\phi_E - \phi_C) = ADT_E^2 e^{\frac{-\phi_E}{kT_E}}(\phi_E - \phi_C)$$

where we have defined the constant $D = \frac{4\pi e m_e k^2}{h^3} \approx 1.2 \times 10^6$ [A m^{-2} K^{-2}]. Note that we have neglected the "back" emission current generated by the collector. This is a reasonable assumption, as for most practical devices, $\phi_E - \phi_c \approx 1V$ and $T_E - T_C \approx 1000K$, therefore $J_C < 10^{-6}J_E$. The ideal power output density is plotted in figure 3.7 for a range of emitter work functions.
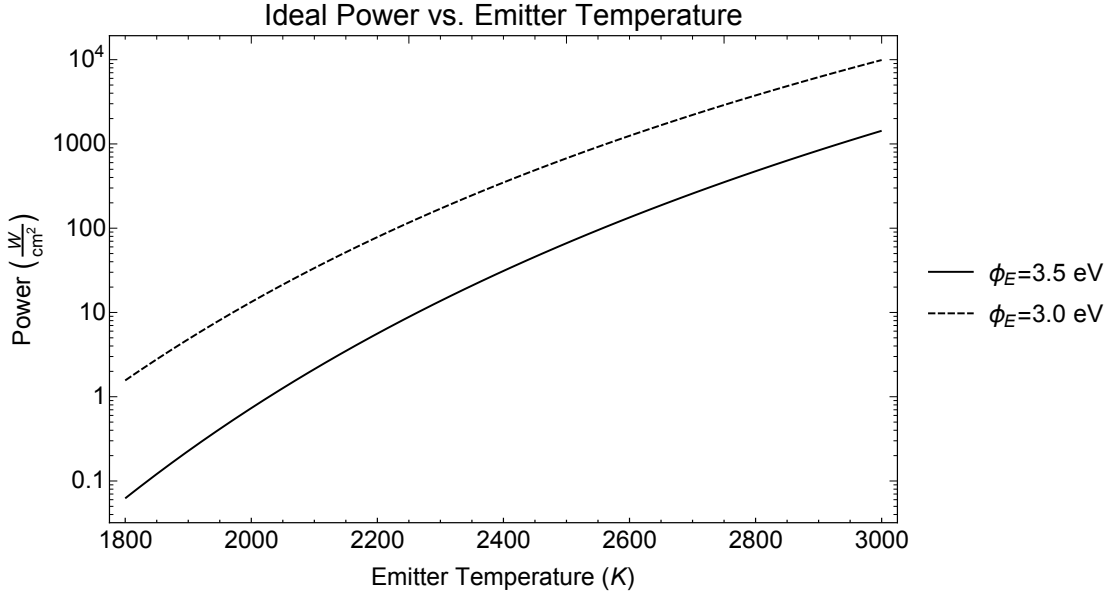
Figure 3.7 Ideal Power vs. Emitter Temperature for $\phi_E = 3eV$ and $\phi_E = 3.5eV$. In both cases, $\phi_E - \phi_C = 1eV$ and $T_E - T_C = 1000K$.

We note that Cs diode TECs achieve much lower ϕ_E values (~1.7-2.7eV) due to the adsorption of Cs onto the electrodes. We chose to use "bare" work functions representative of electrodes that may be feasibly used for in-core TECs without Cs, such as HfC and ZrC.

The total heat supplied to the emitter is balanced by the total heat removed from the emitter in the form of electron emission (Q_{em}), thermal radiation (Q_{rad}), conduction (Q_{cond}, through the electrical leads) less the power dissipated in the device directly as heat, i.e. joule heating (Q_J):

$$Q_{tot} = Q_{em} + Q_{rad} + Q_{cond} - Q_J$$
$$= I\left(\phi_E + \frac{2kT_E}{e}\right) + \sigma\epsilon(T_E^4 - T_C^4) + Q_{cond} - \frac{1}{2}I^2R_L \quad (3.4)$$

Here, $\frac{2kT_E}{e}$ is the average kinetic energy per electron emitted, $\sigma = 5.67 \times 10^{-8}$ W m^{-2} K^{-4} is the Stefan-Boltzmann constant, $\epsilon = (\epsilon_E^{-1} + \epsilon_C^{-1} - 1)^{-1} \approx 0.1 - 0.2$ is the net thermal emissivity of

the system with ϵ_E and ϵ_C being the thermal emissivity of the emitter and collector, respectively and R_L is the load resistance [Ω] of the system. Taking the typical thermal efficiency definition for a TEC device:

$$\eta = \frac{P_{el}}{Q_{tot}}$$

$$= \frac{DT_E^2 e^{\frac{-\phi_E}{kT_E}} (\phi_E - \phi_C)}{DT_E^2 e^{\frac{-\phi_E}{kT_E}} \left(\phi_E + \frac{2kT_E}{e}\right) + \sigma\epsilon(T_E^4 - T_C^4) + Q_C - \frac{1}{2}(DT_E^2 e^{\frac{-\phi_E}{kT_E}})^2 R_C} \tag{3.5}$$

Under ideal circumstances, where losses due to thermal radiation are much greater than that of conduction ($Q_{rad} \gg Q_C$) and where joule heating may be neglected ($Q_J \approx 0$)) we see that the maximum efficiency becomes:

$$\eta_{ideal} = \frac{DT_E^2 e^{\frac{-\phi_E}{kT_E}} (\phi_E - \phi_C)}{DT_E^2 e^{\frac{-\phi_E}{kT_E}} \left(\phi_E + \frac{2kT_E}{e}\right) + \sigma\epsilon(T_E^4 - T_C^4)} \tag{3.6}$$

which is plotted in figure 3.8, again for work functions between 3.0 and 3.5.

The ideal efficiency of a thermionic diode approaches from 50-60% of the Carnot efficiency ($\eta_C = 50\%$). However, thus far, Cs vapor TECs have only achieved about half these values in the laboratory setting, and half again less for practicable devices (e.g. TOPAZ-I and II) [4].The dramatic decrease in efficiency for TECs is due to the techniques used to mitigate a previously ignored effect in our analysis, but one that fundamentally impacts TEC: space charge.
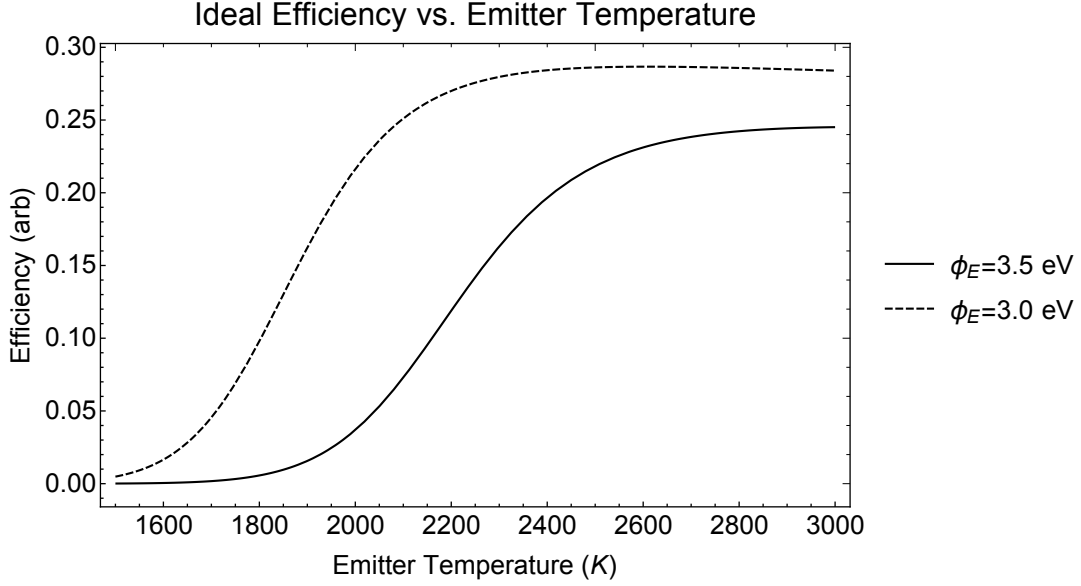
Figure 3.8 Ideal Efficiency vs. Emitter Temperature for $\phi_E = 3\text{eV}$ and $\phi_E = 3.5\text{eV}$. In both cases, $\phi_E - \phi_C = 1\text{eV}$ and $T_E - T_C = 1000\text{K}$.

3.3.3 Space Charge and the Child-Langmuir Limit

Referring back to figure 3.4, the presence of a point charge near a conducting surface induces an electric field such that that point charge is drawn back toward the conducting surface; in the case where the system is in thermodynamic equilibrium, we obtained the Richardson-Dushman equation, a purely thermodynamic formulation of a thermionic emission. However, in TEC devices, there is no equilibrium; energy *is* transferred – from the emitter to the collector – in the form of a steady state electron current. In this instance, a *space charge* emerges between the emitter and collector and with it, an effect we have neglected until this point. Essentially, space charge inhibits the transmission of electrons from the emitter to collector and degrades the TEC's power output substantially. To analyze the problem, we must reorient our focus from thermodynamics to electrostatics.

We begin by defining the two processes happening in tandem: first, electrons are streaming from the emitter to the collector and second, the presence of electrons creates an electric potential between the emitter and collector. We consider the problem in 1-D. The first process can be described by conservation of energy, where the purely kinetic energy of the electrons beginning at the emitter is converted into purely electrical potential energy at the collector; the second process is captured by the Poisson equation, or:

$$\frac{1}{2} m_e v(x)^2 = e V_g(x) \tag{3.7}$$

$$\frac{d^2 V_g(x)}{dx^2} = \frac{\rho(x)}{\epsilon_0} \tag{3.8}$$

where m_e is the mass of the electron [kg], $v(x)$ is the velocity of the electron [m s^{-1}], e is the electron charge [C], V_g is the potential drop across the gap [V], $\rho(x)$ is the spatially dependent

electron charge density [C m^{-3}], ϵ_0 is the permittivity constant [N^{-1} m^{-2} C^2], and x is the spatial variable [m]. If a constant current flows through the circuit such as in figure 3.6, we see the relation:

$$\rho(x)v(x) = J \tag{3.9}$$

where J is the electron current density [A m^{-2}]. By solving equation (3.7) for $v(x)$ and substituting into equation (3.9) we see that $\rho(x) = J\sqrt{\dfrac{m_e}{2eV_g(x)}}$. Substituting this result into the Poisson equation (3.8):

$$\frac{d^2V_g(x)}{dx^2} = \frac{J}{\epsilon_0}\sqrt{\frac{m_e}{2eV_g(x)}}$$

which is a nonlinear second order differential equation. We use the following chain rule identity:

$$d\left[\left(\frac{dV_g}{dx}\right)^2\right] = 2\frac{dV_g}{dx}\frac{d^2V_g}{dx^2}dx = 2\frac{d^2V_g}{dx^2}dV_g$$

then by substituting the new form of equation (3.8) into this identity and integrating,

$$\left(\frac{dV_g}{dx}\right)^2 = \frac{2J}{\epsilon_0}\sqrt{\frac{m_e}{2e}}\int_0^{V_g}\frac{dV_g}{\sqrt{V_g}} = \frac{4J}{\epsilon_0}\sqrt{\frac{m_eV_g}{2e}}$$

$$\int_0^{V_g}\frac{dV_g}{\sqrt[4]{V_g}} = \int_0^x\sqrt{\frac{4J}{\epsilon_0}\sqrt{\frac{m_e}{2e}}}\,dx$$

$$\frac{16}{9}V_g^{3/2} = \frac{4J}{\epsilon_0}\sqrt{\frac{m_e}{2e}}x^2$$

and finally

$$J_{sat} = \frac{4\epsilon_0}{9}\sqrt{\frac{2e}{m_e}}\frac{V_g^{3/2}}{x^2} \tag{3.10}$$

which is the result from Langmuir [41], revealing the maximum current density attainable between two infinite conducting planes in vacuum separated by distance x and held at a potential difference V_g. Using the relation $P_{out} = P_{sat} = J_{sat}V_g$, we may infer the maximum gap distance to achieve a desired power density:

$$x = \sqrt[4]{\frac{32\epsilon_0^2 e}{81 m_e}} V_g^{5/4} P_{sat}^{-1/2} = 1.52 * 10^{-2} V_g^{5/4} P_{sat}^{-1/2} \ [mm]$$

where P_{sat} here is expressed in W cm^{-2}. As is seen in figure 3.9, in order to obtain power densities of significance ($P_{sat} > 0.1$ W cm^{-2}) with realistic output voltages, $V_g = V_{out} = (\phi_E - \phi_C)/e$ gap distances are in the range of 10-50μm; at $P_{sat} = 1$ W cm^{-2}, gap distances are less than the width of a human hair ~20μm, a rather restrictive design constraint for vacuum based devices.
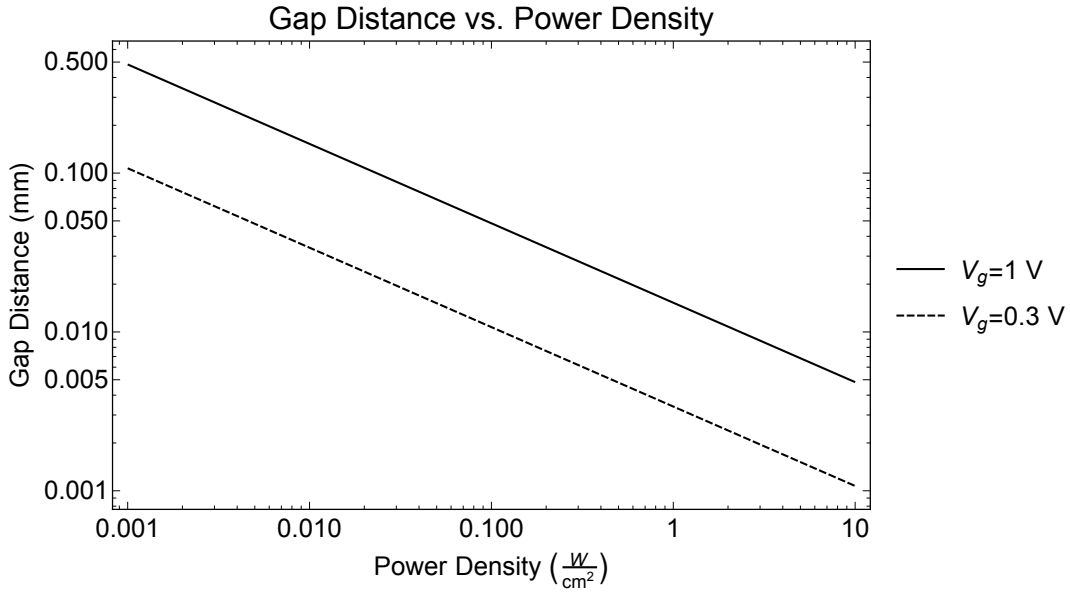
Figure 3.9 Gap distance vs. power density in a realistic voltage range for vacuum TEC devices, where $V_g = V_{out} = (\phi_E - \phi_C)/e$.

3.3.4 Space Charge Mitigation Techniques

As was made obvious in the previous section, space charge mitigation is imperative to TEC's viability in devices of practical power densities (0.1-10 W/cm²). There are two main types of TECs, delineated by how they approach space charge: the vacuum diode and plasma diode. The former must overcome the small distance hurdle, while the latter uses a charge neutral plasma to relax the interelectrode gap distance requirement (explained in the next section). In essence, vacuum gap TECs attempt to leverage advanced, low work function materials along with advanced manufacturing processes (e.g. Micro ElectroMechanical Systems, MEMS) to devise small scale, non-nuclear devices for waste heat recovery [42]. Major deployment issues include:

1. Given such restrictive electrode spacings (1-10μm), vacuum diodes TEC must operate at significantly lower temperatures ($T_E \approx 1200$K, $T_C \approx 700$K) than typical plasma diodes ($T_E \approx 2000$K). Consequently, they require very low work function electrodes, with $\phi_E < 1.8$ eV and the $\phi_C < 1.5$ eV. As recently as 2014 [42] "state of the art" vacuum converters were thermally stable only for several hours (before short

circuiting) at these significantly reduced temperatures. Conversely, devices applicable to high powered space missions must operate at least 600K higher and for greater than 12000 hours continuously [5].

2. High radiation environments will undoubtedly perturb (if not destroy) the nanoscale microstructures required to mediate vacuum-mode thermionic energy conversion. Therefore vacuum devices would not only have to be placed far outside of the nuclear reactor core (and thus require additional coolant and electrical transfer systems), but also require shielding from cosmic radiation; the combination would almost certainly add significant mass to the energy conversion module, thereby diminishing its inherent advantages outlined in the introduction. Furthermore, to the authors knowledge, the material properties of advanced low-work function electrodes have not been verified in any significant radiation environments.

Despite these inherent disadvantages, the lack of progress in thermal stability in laboratory settings, and an explicit recommendation from the national academy of sciences to discontinue research in vacuum type converters, the vacuum-type TEC remains the focus of current US R&D efforts (both academic and industry) in thermionics [42]. This is primarily because of potential applications to small-scale, non-nuclear devices, e.g. waste heat to power production in electronics; the prospect of vacuum-type TECs being applicable to nuclear devices of any kind is remote.

The plasma diode-type TEC, on the other hand, has successfully generated kW_e – level electrical power in the two most powerful space nuclear reactors flown to date: TOPAZ – I and TOPAZ – II. This technology mitigates the space charge effect by injecting the interelectrode space with a low-pressure vapor, typically Cesium. While the device operates in the most common "ignited mode", thermionically emitted electrons transiting the gap partially ionize the vapor (by inelastic collisions), producing a low-temperature plasma. Being electrically neutral, the plasma serves to eliminate space charge between transiting electrons. Without the space charge effect, typical cesium plasma diode TEC gap sizes range from 100μm-1mm.

The most common plasma TEC embodiment uses a low pressure cesium vapor (~1 torr) both because of its low ionization potential (3.9 eV) and its ability to favorably lower refractory metal (e.g. tungsten, molybdenum, niobium) work functions, which effectively raises the emission current for a given heat input. The most common electrode materials are tungsten (emitter) and molybdenum (collector); adsorption of cesium onto their surfaces drives down the effective emitter and collector work functions to around 1.8 eV and 1.5 eV, respectively. These systems have demonstrated 25-35% Carnot efficiency in the laboratory at emitter and collector temperatures of 2000 K and 1000 K, respectively. However, practical devices, such as the TOPAZ nuclear reactors (I and II) have only achieved about half that: 11% of the Carnot efficiency. This is due to a particular physical limitation: the device sacrifices up to 50% of the emitted electron energy to generating the cesium plasma. This ultimately drives down electrical output and thermodynamic efficiency.

One way to increase the thermal efficiency of such a plasma diode TEC would be to excite the plasma separately, in lieu of an "ignited mode" plasma, to mitigate space charge. That is, instead of using thermionically emitted electrons to ionize the plasma, a separately excited plasma is sustained via another energy source. Consider a nuclear fission source: high energy fission fragments (1-50 MeV) and energetic beta decay electrons (2-8 MeV) from fissioning nuclear fuel elements. Igniting a plasma via high energy charged particle radiation would benefit

both TEC design and performance. High energy charged particles have a far greater ionization rate and penetration into the plasma than thermionically emitted electrons. These inherent qualities of high energy charged particles allow for 1) a more volumetrically uniform plasma density that would relax interelectrode gap distances to greater than 1mm, and 2) a higher electron temperature (see chapter 2), which drives higher voltage, power output, and efficiency. Where previous practical Cs plasma-diode converters achieved 11% Carnot efficiency with gap distances < 0.5mm, high energy charged particle ignition could simultaneously enhance the device's efficiency in excess of 90% Carnot efficiency and relax design constraints to gap distances > 1 mm. These enhancements to TEC would completely change the current landscape of space nuclear power paradigm.

3.3.5   The I-V characteristics of the Separately Excited Plasma Diode

In a charge-neutral plasma of uniform density ($n_i = n_e$) between an emitter and collector of equal surface area (figure 3.10) we observe the following: due to the lower mass (therefore greater mobility) of the plasma electrons with respect to the ions, the electrons will be lost from the system through the electrode surfaces much more rapidly than the ions. This gives rise to a small region of increased ion concentration (that is, $n_i > n_e$) between the electrode surfaces and the uniform plasma. Often, the small region where $n_i \neq n_e$ between the electrode and neutral plasma is called the *sheath* and the larger region where $n_i = n_e$ is called the *bulk*.

In the absence of applied voltages or *net* thermionic emission (i.e. , $T_E = T_C$ and $V_E = V_C$) the electrode surfaces adopt a negative potential with respect to the bulk plasma, the plasma potential, V_p [V]. It is important to note that the plasma potential is independent of the electrode material properties. The plasma species' arrival rates to the electrode surfaces (in the absence of applied fields) depends solely on their relative mobilities, therefore this potential is a property of the plasma only. The plasma potential is asserted without proof for $T_e \neq T_i$ as:

$$V_p = \frac{kT_e}{2} \ln\left(\frac{M}{2\pi m_e}\right)$$

where k is the Boltzmann constant expressed in V K^{-1} and the random plasma electron current or ion current incident on the sheath is attenuated by a factor of $\exp\left(-\frac{V_p}{T_{e(i)}}\right)$ depending on applied voltages at the electrode boundaries (a more in depth treatment of the subject matter may be found elsewhere [37]). This positive plasma potential near the emitter mitigates space charge in order to allow thermionic electron transmission into the bulk plasma.

In the simplest case where there is no net thermionic emission or applied voltages, the steady state open circuit voltage of the system will simply be equal to the contact potential between emitter and collector, or $\phi_E - \phi_C$. This must be the case as both electrodes facing the plasma will adopt a potential, $-V_p$, in order to establish a net 0 current through that plasma: then the corresponding contact potential between emitter and collector must form such that no net thermionic emission from the collector to emitter occurs. In this case, we may think of the plasma acting as a lossless conducting wire. Figure 3.10 serves as a conceptual illustration of the main components and features of a separately excited plasma diode. If we further simplify by allowing $\phi_E = \phi_C$ and electrically ground the electrodes, we would see contact potential vanish between the electrodes, which would both "float" equally to $-V_p$. Depending on specific

boundary conditions at the electrode surfaces, such as applied voltages, differing material work functions and electron emission, sheath properties will change; we will assess this problem, specifically for TEC.

Let us consider a system where some current, I, flows in a power *producing* fashion, as in figure 3.11. The total current at the emitter is:

$$I = I_{th} + I_{i,E} - I_{e,E} \exp\left(-\frac{V_{p,E} - V_E}{T_{e,E}}\right), V_E < V_{p,E}$$

(3.11)

$$I = (I_{th} + I_{i,E}) \exp\left(-\frac{V_E - V_{p,E}}{T_E}\right) - I_{e,E}, V_E > V_{p,E}$$
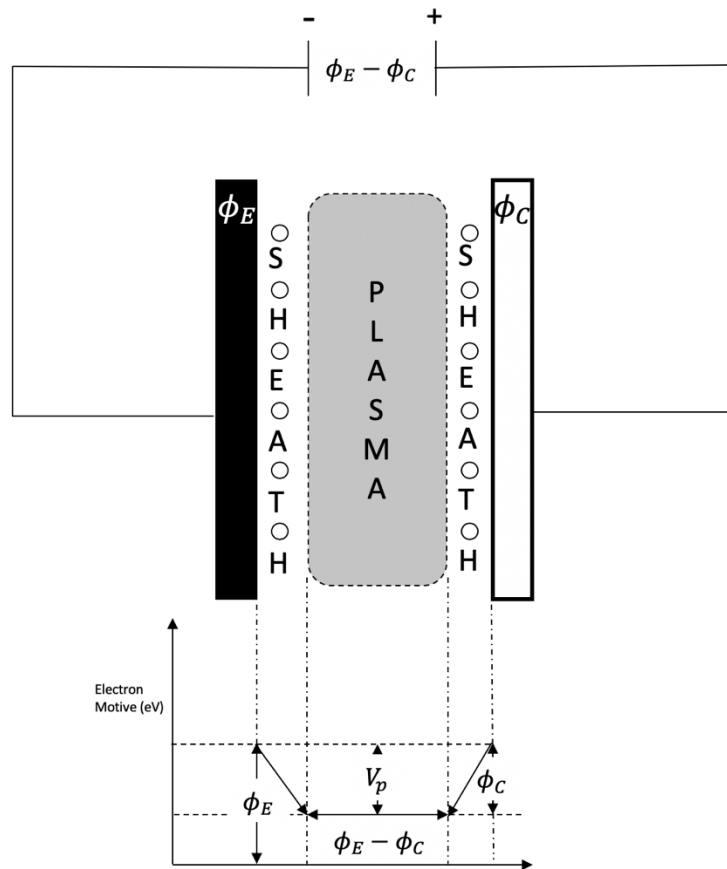
Figure 3.10 Schematic of an open circuit separately excited plasma TEC and corresponding electron motive diagram. Due to rapid loss of electrons through the electrodes, sheaths develop between the electrode surfaces and the bulk plasma. Since $n_i > n_e$ the resulting electric fields point outward from the bulk plasma to the walls. These fields repel electrons to the bulk while attracting ions to the electrodes. An open circuit voltage between the emitter and collector naturally forms due to the differences in work function, as would occur with no plasma present (e.g. placing a conducting wire in place of the plasma). Note that when $\phi_E = \phi_C$, the contact potential vanishes along with the open circuit voltage.

and at the collector:

$$I = I_{e,C} \exp\left(-\frac{V_{p,C} - V_C}{T_{e,C}}\right) - I_{i,C}, V_C < V_{p,C}$$

(3.12)

$$I = I_{e,C} - I_{i,C} \exp\left(-\frac{V_C - V_{p,C}}{T_C}\right), V_C > V_{p,C}$$
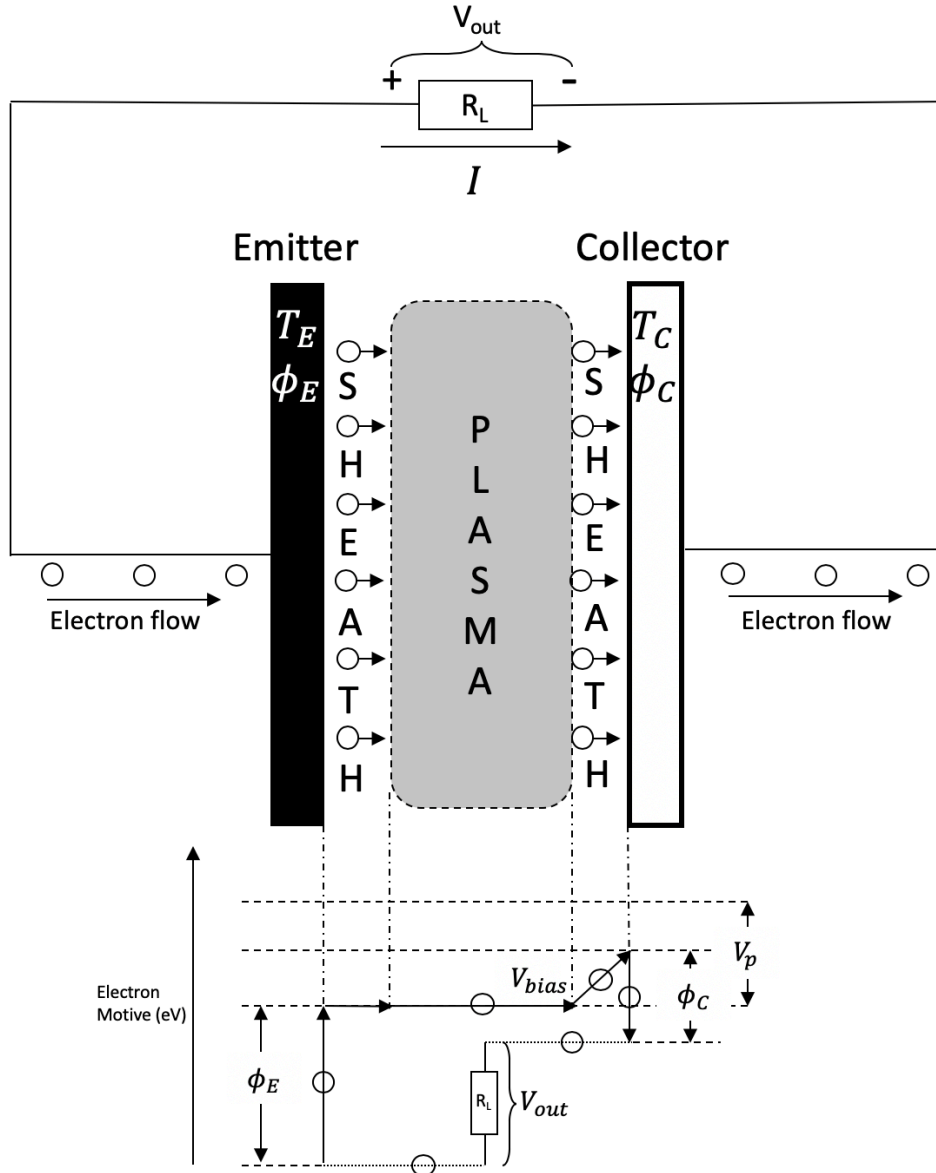
Figure 3.11. Schematic and electron motive diagram of an emitter and collector immersed in a separately excited plasma. In the ideal case, the emission current is adjusted such that the $V_E = V_p$, thereby eliminating any electron motive forces. This is analogous to the ideal diode in section 3.3.1 where the optimal power was extracted when $V_{out} = \phi_E - \phi_C$.

where I is the net current, $I_{i,E}$ and $I_{i,C}$ are the ion currents at the emitter and collector, respectively, $I_{e,E}$ and $I_{e,C}$ are the electron currents at the emitter and collector respectively. Here, the expression for the electron and ion currents are given by:

$$I_{e,\alpha} = \frac{eA_\alpha n_{s,\alpha}}{4}\bar{v}_e = A_\alpha e n_{s,\alpha}\sqrt{\frac{kT_{e,\alpha}}{2\pi m_e}}$$

$$I_{i,\alpha} = eA_\alpha n_{s,\alpha}u_{bohm} = A_\alpha e n_{s,\alpha}\sqrt{\frac{kT_{e,\alpha}}{M}}$$

(3.13)

where A_α is the surface area of electrode α [m²]. The Bohm velocity, u_{Bohm} [m s⁻¹], greater than the ion's thermal velocity, is the velocity ions gain as they diffuse from the bulk plasma to the sheath. Assuming a system where the emitter and collector are held at potentials below that of the plasma, we may solve for V_E and V_C:

$$V_E - V_{p,E} = T_{e,E}\ln\left(\frac{I_{th} + I_{i,E} - I}{I_{e,E}}\right)$$

$$V_C - V_{p,C} = T_{e,C}\ln\left(\frac{I + I_{i,C}}{I_{e,C}}\right)$$

Defining an electrode bias voltage, $V_{EC,bias} = V_E - V_C$, and plasma bias, $V_{p,bias} = V_{p,E} - V_{p,C}$ we see:

$$V_{EC,bias} - V_{p,bias} = T_{e,E}\ln\left(\frac{I_{th} + I_{i,E} - I}{I_{e,E}}\right) - T_{e,C}\ln\left(\frac{I + I_{i,C}}{I_{e,C}}\right)$$

$$= \ln\left[\frac{\left(\frac{I_{th} + I_{i,E} - I}{I_{e,E}}\right)^{T_{e,E}}}{\left(\frac{I + I_{i,C}}{I_{e,C}}\right)^{T_{e,C}}}\right]$$

$$= \ln\left[\frac{I_{e,C}^{T_{e,C}}\left(I_{th} + I_{i,E} - I\right)^{T_{e,E}}}{I_{e,E}^{T_{e,E}}\left(I + I_{i,C}\right)^{T_{e,C}}}\right]$$

Following the electron motive diagram given in figure 3.11 The total output voltage, $V_{out} = V_{EC,bias} - V_{p,bias} + \Delta\phi/e$ ($\Delta\phi = \phi_E - \phi_C$) is obtained. Thus, the system's output I-V characteristic is given by:

$$V_{out} = \ln\left[\frac{I_{e,C}^{T_{e,C}}\left(I_{th} + I_{i,E} - I\right)^{T_{e,E}}}{I_{e,E}^{T_{e,E}}\left(I + I_{i,C}\right)^{T_{e,C}}}\right] + \Delta\phi/e, \quad V_E < V_{p,E}$$

(3.14)

In the opposite case, where $V_E > V_{p,E}$, we may employ the same methodology to obtain:

$$V_{out} = T_E \ln\left(\frac{I_{th} + I_{i,E}}{I_{e,E} + I}\right) - T_{e,C} \ln\left(\frac{I + I_{i,C}}{I_{e,C}}\right) + \Delta\phi/e, \quad V_E > V_{p,E} \tag{3.15}$$

To obtain a general sense of the I-V characteristic for this particular TEC device, it is instructive to make some simplifying assumptions: a constant plasma density and temperature profile throughout the bulk plasma (i.e. from the emitter and collector sheath edges) as was done by Waymouth [43]. Thus, $V_{p,E} = V_{p,C} = V_p$, $V_{p,bias} = 0$ Equations (3.14) and (3.15) become:

$$V_{out} = \begin{cases} T_e \ln\left[\frac{I_{e,C}}{I_{e,E}} \frac{(I_{th} + I_{i,E} - I)}{(I_{i,C} + I)}\right] + \Delta\phi/e, & V_E < V_p \\[3mm] T_E \ln\left(\frac{I_{th} + I_{i,E}}{I_{e,E} + I}\right) - T_{e,C} \ln\left(\frac{I + I_{i,C}}{I_{e,C}}\right) + \Delta\phi/e, & V_E > V_p \end{cases}$$

It is useful to identify relations between the ion and random electron currents at the emitter and collector sheaths given the constant temperature and density profile approximation. From equation (3.13) we see that $I_{e,\alpha}/I_{i,\alpha} = \sqrt{\frac{M}{2\pi m_e}} \equiv \mu$, $I_{e,C}/I_{e,E} = \frac{A_C}{A_E} \equiv A$. Further, it is desirable to maximize the device's power output. As discussed previously (see section 3.3.1) For $V_E \neq V_{p,E}$ thermionic emission is *undercompensated* for $V_E > V_{p,E}$ and the resulting space charge attenuates the emission current, thereby limiting power output; for $V_E < V_{p,E}$ thermionic emission is *overcompensated* and a sub-maximal emission current is being drawn from the emitter, thereby also limiting power output. Thus, diode performance is maximized for conditions where space charge is *exactly* mitigated at the emitter, making $V_E = V_{p,E}$ such that the condition at the emitter becomes:

$$\frac{I}{I_{th}} = 1 + \frac{I_{e,E}}{I_{th}}\left(\frac{1}{\mu} - 1\right) \tag{3.16}$$

and it is useful to define $I_{e,E}/I_{th} \equiv R$ such that V_{out} for maximum power output conditions may be expressed as:

$$V_{bias} = \begin{cases} T_e \ln\left[A \frac{\left(1 + R/\mu - I/I_{th}\right)}{\left(AR/\mu + I/I_{th}\right)}\right], & V_E < V_p \\[4mm] T_E \ln\left(\frac{1 + R/\mu}{R + I/I_{th}}\right) - T_e \ln\left(\frac{I/I_{th} + AR/\mu}{AR}\right), & V_E > V_p \end{cases} \tag{3.17}$$

It is illuminating to compare the I-V characteristics and the relative power output of separately excited plasma TEC to that of an ideal TEC. Using the relation $V_{out} = V_{bias} + \Delta\phi/e$:

$$\frac{P_{out}}{P_{el,ideal}} = \frac{IV_{out}}{I_{th}\Delta\phi}$$

$$= \frac{I}{I_{th}}\frac{(V_{bias} + \Delta\phi)}{\Delta\phi}$$

Both $\frac{V_{out}}{\Delta\phi}$ and $\frac{P_{out}}{P_{el,ideal}}$ are plotted in figure 3.12 for different values of A ranging from 1 to 100. For $A > 10$, the device may achieve ideal TEC performance (50% Carnot efficiency) and beyond; as $A \to 100$, $\eta_{th} \to 0.45$ which is 90% of the Carnot efficiency. In comparison, ideal TECs approach 60% of the Carnot efficiency and practical devices have only achieved about half this value (25-35% of the Carnot efficiency) [40].

Of course, evaluating a separately excited plasma TEC's peformance based on its Carnot efficiency alone would not be accurate: its elevated performance is enabled by adding energy to the plasma without generating heat in the process. In doing so, the added energy (or "heat") leads to a uniformly increased plasma electron density and temperature regardless of the emission current. An increased collector/emitter surface area ratio then allows the lower energy thermionic current from the emitter to be collected at a higher energy at the collector, thereby increasing the total power output with this voltage gain (see figure 3.12). This is described by Waymouth [43]. However, as this additional plasma "heat" is only weakly coupled to the heat source, i.e. the emitter, it can be scaled almost arbitrarily high without affecting the heat input term used to calculate the Carnot efficiency. Adding a sufficient amount of this plasma heating could feasibly push the device's efficiency to greater than 100% of the Carnot efficiency. Thus, the separately excited plasma TEC is not a true heat engine; rather, the impossible surmounting of the Carnot efficiency reflects an increase in the device's power density, W kg^{-1}, as electrical power output is increased with no additional heat dissipation requirement.

It is crucial to note that all other TEC devices are true heat engines and are therefore tied to the ideal diode performance limits derived previously. Particularly for ignited mode Cs diodes, where thermionic electron impact ionization is the primary plasma ionization mechnism, additional heat to the plasma may either come by increasing thermionic emission or improving the plasma chemistry (via vapor additives). In the case of the former, to increase emission without additional heat input, one must increase the emitter surface area. Therefore, for Cs diode TECs it is desirable to *decrease* the collector/emitter surface area ratio; This concept has been investigated previously in the form of developed emitter surfaces, where small grooves (~10s of μm) etched into the emitter increase its apparent surface area. A review of these studies may be found elsewhere [44]. Optimizing plasma chemistry has proven more fruitful to improved performance. For example, introducing trace amounts of oxygen into the traditional Cs diode increased the device's output 300% and improved efficiency 80% from traditional diodes at large spacings (~0.5mm) [45].

In short, where traditional TEC devices derive their input energy entirely from heat, the separately excited plasma TEC offers its plasma as an additional conduit through which energy may be transferred without dissipating heat. The major implication is that not only can this class of TEC device *produce* energy at a higher specific power than any of its predecessors, but may

also *transfer* this power at equivalent densities across multiple systems; this will be a highly sought after feature in power systems for future space missions [5, 16].

Relative Voltage vs. Current

Relative Power vs. Current
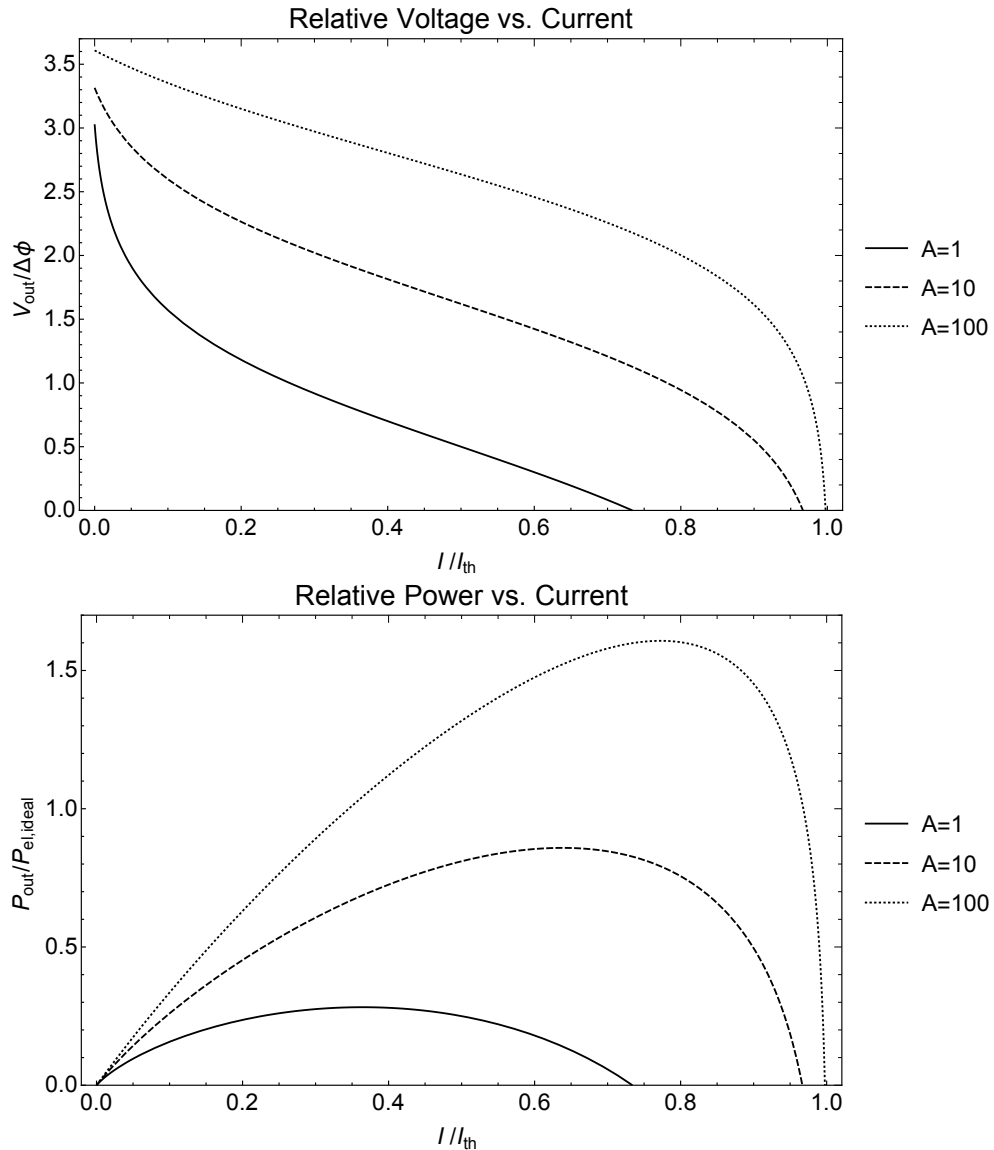
Figure 3.12 Relative Voltage and Power vs. Current for increasing collector to emitter surface area ratios, A. Here, we used $\mu =150$, corresponding to an Ar_2^+ ion species, $T_e =5000K$, $T_E =2000K$, $R = 0.64$, 0.36, and 0.2 for $A = 1$, 10, and 100 respectively, and $\Delta\phi/e = 1V$. These are expected values for a CW power producing nuclear reactor.

Chapter 4: HITEC Model

4.1 Overview

Chapter's 2 and 3 established a theoretical basis for charged particle ionized plasmas and thermionic energy conversion principles for such a plasma, i.e. the separately excited plasma

TEC. Our treatment further extended into conditions specific to a nuclear reactor, where the driving force of the plasma comes from neutron induced fission. Together, these theories inform a sensible (and useful) parameter space under which ideal performance can be achieved. For instance, given a 5 μm thick foil of pure ^{235}U subjected to a thermal neutron flux, $\phi_{th} = 10^{13}$ n cm^{-2} s^{-1} submerged in 90 torr of 1mm thickness argon gas (the interelectrode gap distance), the resulting steady state plasma conditions are of order $T_e \approx 5000$ K and $n_e \approx$ 1-2 x 10^{12} cm^{-3}. Given these conditions, for an emitter collector surface area ratio, $A = 1$, $\mu = 150$, $\Delta\phi = 1$eV and $R = 0.64$ for maximum power output, and the required thermionic current density, J_{th}, becomes 2.5 – 5 A cm^{-2}; a candidate thermionic emitter, e.g. ZrC, whose work function $\phi_E = 3.5$eV would operate at the temperature range of 2100-2200K to meet this emission current density requirement, and the power output would be 30% of the ideal value, or 0.75 – 1.5 W cm^{-2}.

The example above shows that we have adequate means to make useful (but approximate) calculations and gain insight into the experimental results obtained in the GM study, whose conditions were very similar to those outlined above. However, using these average values are not sufficient to inform a sensible *design* space for a full scale nuclear reactor based off this energy conversion scheme. This is what we seek to accomplish here. To achieve this, we must adapt nuclear reactor scaling laws and our previously established theoretical basis into a common framework. Called the Heavy Ion Thermionic Energy Conversion (HITEC) model, a model flow-diagram is reintroduced from Chapter 1 into Figure 4.1. Now, we will step through each modular component of HITEC, which may be grouped broadly into four subsections: charged particle stopping, the plasma and heat transfer, single TEC cell output, and reactor scaling. The HITEC model is responsible for accurately tracking charged particle energy deposition throughout solid and gaseous media, then determining plasma properties and TEC I-V characteristics based on the theoretical basis established in previous chapters. It is not responsible for calculating the fission rate, which depends on neutronics analysis, and it is not responsible for calculating fuel element temperature profiles, which depends on thermal analysis. The plasma properties and corresponding TEC I-V characteristics depend on heavily on both fission rate and fuel element temperature profiles, parameters that are *outside* of HITEC's sphere of influence. Thus, reactor scaling will only be as accurate as the additional analyses and/or assumptions made by user.
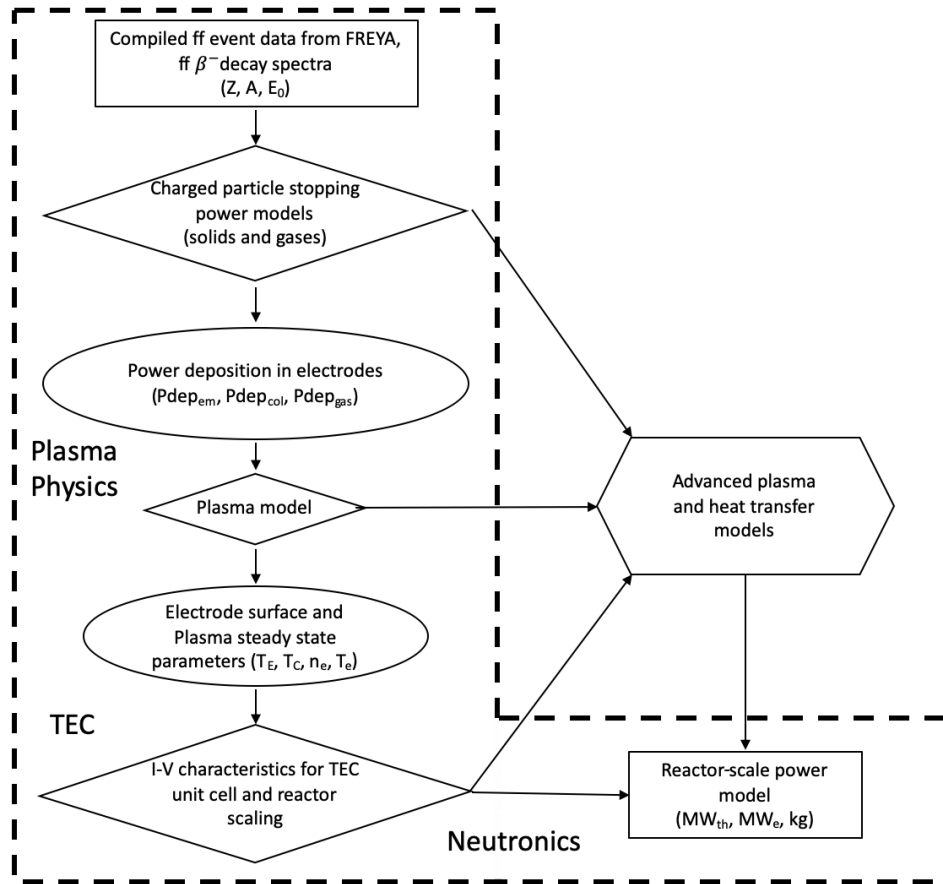
Figure 4.1 Overview of the HITEC model.

4.2 Charged Particle Stopping

4.2.1 Spatial tracking: Infinite Planar and Coaxial Geometries

It is helpful to understand the general particle tracking methodologies employed in this model. We will begin by forming the geometric basis for two emitter-collector geometries: the infinite parallel plane configuration and the infinite coaxial cylinder configuration. A schematic for the infinite planar configuration is illustrated below in Figure 4.2. In this case, we see immediately that there is no azimuthal angular dependence, since the planes' transverse dimensions are much greater than the distance which separates them. Therefore, when determining the total distance traveled by a randomly sampled particle we may reduce the random sampling to two quantities: some perpendicular distance, d, from the surface of either the emitter or collector (or both) and some angle, θ which ranges from $0 - 90°$. Then, referring to Figure 4.2, the distance a particle may travel through the collector and interelectrode space is given by $l = \frac{d}{\cos \theta}$, and $L = \frac{R}{\cos \theta}$ respectively.

49
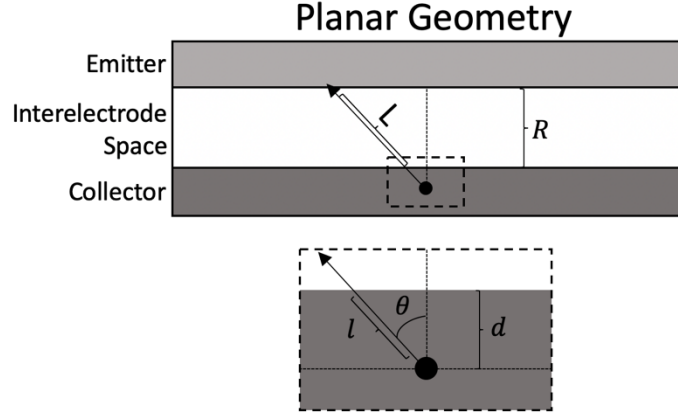
Figure 4.2 Planar geometry for charged particle trajectories.

Treating the coaxial geometry is a bit more complicated. In the case of fission fragments, where the distance, d, from the surface of either the emitter or collector is much smaller than the inner and outer radii dimensions, r, and R, respectively, we may treat the particle's trajectory through the fuel as we did for the infinite plane previously as shown in Figure 4.3. However, once the particle enters the interelectrode space, we see both poloidal and azimuthal dependence. The azimuthal dependence is accounted for by simply dividing the total length traveled by the particle, L, by a factor of $\sin\phi$, where ϕ is randomly sampled from $0 - 90°$. In the poloidal coordinate, there are two regions that a particle may travel through once it escapes the collector. The first is where the particle's path is unimpeded by the presence of the emitter. For this scenario, it is easy to show through simple geometric analysis that the total distance a particle may travel is $L(R, r, \theta, \phi)^* = 2R\cos\theta\csc\phi$. However, once the particle's path is intercepted by the emitter, it may be shown that the total distance it travels is

$\csc\phi\sqrt{R^2 + r^2 - 2R^2\sin^2\theta - 2\sqrt{R^2\cos^2\theta(2r^2 - R^2\cos 2\theta)}}$. The condition under which this occurs is when the angle of emission, $\theta < \sin^{-1}\frac{r}{R}$. Thus, we may define the total path length of a heavy ion emerging from the collector as:

$L(R, r, \theta, \phi)^* =$

$$\begin{cases} 2R\cos\theta\csc\phi & \theta > \sin^{-1}\frac{r}{R} \\ \csc\phi\sqrt{R^2 + r^2 - 2R^2\sin^2\theta - 2\sqrt{R^2\cos^2\theta(2r^2 - R^2\cos 2\theta)}} & \theta < \sin^{-1}\frac{r}{R} \end{cases}$$
(4.2)

We may not make the infinite plane approximation for coaxial geometries when tracking beta particle emission from surfaces, since the range of betas in the fuel is usually comparable to its major and minor radii (several mm to cm) in general. For beta particles propagating inward toward the center of the coaxial geometry, i.e. when d is the *outward* distance from a surface of radius R:

$$l(R, r, \theta, \phi)^* = \csc\phi\left[(d + R)\cos\theta - \sqrt{\frac{1}{2}[R(R - 2d) - d^2 + (d + R)^2\cos 2\theta]}\right]$$
(4.3)

50
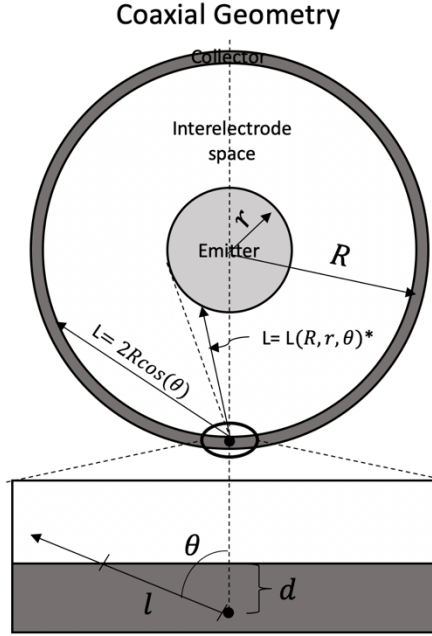
Figure 4.3 Semi-infinite Coaxial geometry for charged particle tracking, where fission fragments are emitted from the collector.

and when propagating out from the center, i.e. d is the *inward* distance from the surface:

$$l(R, r, \theta, \phi)^* = \csc \phi \left[(d - R) \cos \theta - \sqrt{\frac{1}{2}[R(R + 2d) - d^2 + (d - R)^2 \cos 2\theta]} \right] \tag{4.4}$$

which this is shown schematically in Figure 4.3. Once the beta particles leave the surface, their distance traveled in the interelectrode gap may be treated by equations (4.3) and (4.4) once again, where $d \rightarrow R - r$ and $R \rightarrow r$ (for (4.3) only). Actually, we see that (4.2) for $\theta < sin^{-1}\frac{r}{R}$ is actually (4.4) where the aforementioned substitution for variables d and R are made.

We note a couple of assumptions made in the randomness and chosen limits of θ and ϕ. First, due to the isotropic nature of both fission and subsequent beta decay, both θ and ϕ may be assumed to be completely random for every event. Second, fission fragments emerge in diametrically opposed directions in 4π, therefore for every fission event, exactly 1 fission fragment will travel *toward* the interelectrode space. Thus, given the poloidal and azimuthal symmetry of both the semi-infinite coaxial and infinite planar configurations, we may restrict the random sampling of θ and ϕ to the range of 0 – 90º. In the case of beta decay, exactly ½ of the beta particles will travel toward the interelectrode space for the planar configuration, but since there are two fission fragments per fission event that both necessarily beta decay, we see that on average 1 beta particle travels toward the interelectrode space. Correspondingly, for the planar configuration, we may use similar bounds on θ and ϕ for betas. For beta emission in the coaxial geometry, where the propagation is outward, we must extend the upper bound of θ to 180º, since the emitter's dimension may be small enough so that the betas may escape into the interelectrode gap for $\theta > 90$º; this can never be the case when the propogation direction is inward because the

51

beta would simply escape the converter system for $\theta > sin^{-1}\frac{d}{R}$ analogous to when fission fragments "miss" the emitter as they travel inward from the collector. With geometry tracking equations sufficient to calculate projected path lengths, l and L, for both fission fragments and beta particles in infinite planar and semi-infinite coaxial electrode configurations, we now formulate the energy tracking models used for these particles.

4.2.2   Energy Tracking: Fission Fragments

Referring back to figure 4.1, the first step is to calculate charged particle energy deposition in the system, as this will give us insight into the heat production (given a neutron flux) in the main components of a TEC fuel element: the emitter, collector, and interelectrode plasma (gas). Where previous fission fragment stopping models use a representative average mass, charge state and kinetic energy for a "light" and "heavy" fragment as an input [14, 16], we use a fission fragment library, generated by FREYA [46], an energy conserving fission event generator, for the mass A (amu), proton number Z, and initial kinetic energy E_0 (MeV). Since the HITEC model uses individual fission fragments, rather than average "light" and "heavy" values, it must take a sufficiently large sample of fission fragments and run each fragment through its entire energy deposition into the system. This energy deposition calculation process is summarized in figure 4.2 for a coaxial fuel element geometry.

The code begins by reading in 10^5 fission events generated by FREYA; each event is assigned a light and heavy fragment Z and A value, as well as the total kinetic energy of each fragment. Mass and energy distributions of the fission event file are shown in figure 4.2 and the fundamental theory behind their calculation may be found elsewhere [46]. Along with the fission events, stopping power for hydrogen in the relevant materials are loaded (i.e. the emitter, collector, and interelectrode spacing. The code includes several sample materials, all derived from the SRIM stopping power code [19], including all the noble gases, uranium, uranium oxide, and uranium carbide. The user may also upload his own energy dependent hydrogen stopping power values in a straightforward manner. Appendix A will outline the general format of the data input so this process is seamless.
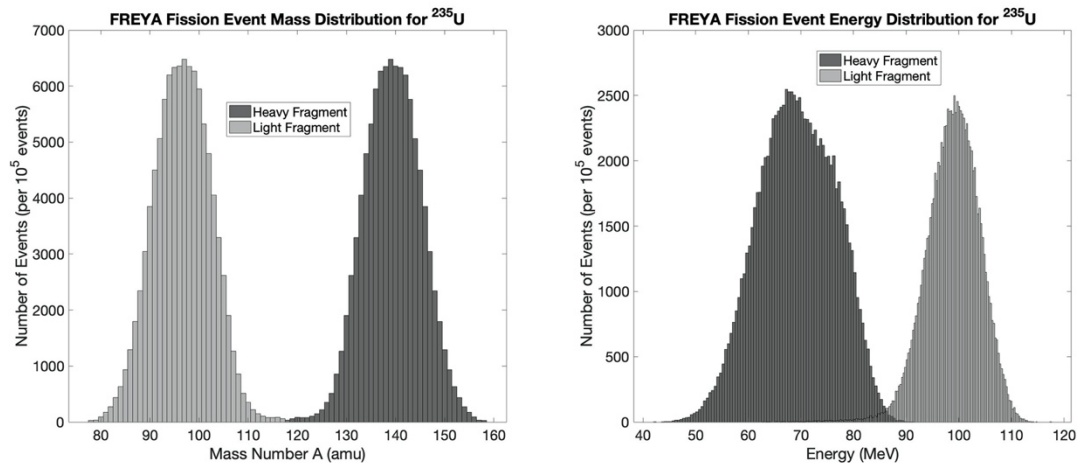
Figure 4.2 Mass and Energy distributions for FREYA output file.

From here, the fission fragment's total range in the fuel is calculated using the Projected Range ALgorithm (PRAL), adapted from SRIM. For the sake of brevity, we show only the major

steps of the calculation; the reader is referred to the complete derivation of the algorithm's components in their manual [19]. Remembering equations (2.1) and (2.2), we formulate the range of an ion by determining both the electronic and nuclear stopping powers, then integrating their sum over the particle's total energy. For electronic stopping we, begin by comparing the ion's initial velocity, v_i to that of the electrons in the medium, or the target, as this determines its effective charge, $Z_{i,eff}$, which satisfies an empirical relationship between the stopping powers of hydrogen and all other heavy ions. For fission fragments, which are considered medium velocity heavy ions[19], the interaction with these electrons is as if they were a free electron gas in the ground state. Then, the fermi velocity (m s^{-1}), stated without proof, is:

$$v_F = \frac{\hbar}{m_e}(3\pi^2 n_e)^{1/3}$$

where n_e [m^{-3}] is the electron density in the fuel (or solid medium). The following criteria determines the expression for the relative velocity between the ion and Fermi velocity

$$v_{rel} = \begin{cases} v_i\left(1 + \dfrac{v_f^2}{5v_i^2}\right) & v_i \geq v_F \\[2em] \dfrac{3}{4}v_F\left(1 + \dfrac{2v_i^2}{3v_F^2} - \dfrac{v_i^4}{15v_F^4}\right) & v_i < v_F \end{cases}$$

where $v_i = \sqrt{\dfrac{2E_0}{931.5*A}}$. The effective ion velocity, v_{eff} [m s^{-1}] is defined as:

$$v_{eff} \equiv \frac{v_{rel}}{v_{bohr}Z^{2/3}}$$

where $v_{bohr} = \dfrac{\hbar}{m_e r_{bohr}} = 2.188 \times 10^6$ m s^{-1} is the Bohr velocity. For $v_{eff} < 0.13$, the ion velocity is said to have slowed to what is called "velocity proportional" stopping, or where the electronic stopping power is $\propto \sqrt{E_i}$. $v_{eff} > 0.13$, the empirical scaling formula – which scales the electronic stopping power of heavy ions to that of hydrogen – originally put forth by Northcliffe is [47]:

$$\frac{\left(dE/dx\right)_{i,el}}{\left(dE/dx\right)_{H,el}} = \left(\frac{Z_{i,eff}}{Z_{H,eff}}\right)^2 \approx \left[1 - \exp(-v_{eff})\right]^2$$

where $\left(dE/dx\right)_{i,el}$ and $\left(dE/dx\right)_{H,el}$ are the stopping powers of the ion and hydrogen, respectively and $Z_{i,eff}$ and $Z_{H,eff}$ are the *effective* charge states of the heavy ion and hydrogen, respectively. Reshaping this general form to fit thousands of experimental heavy ion stopping power measurements reveal the final form [48]:

$$\left(dE/dx\right)_{i,el} = \left(dE/dx\right)_{H,el} \{[1 - \exp(-\alpha)][1.034 - 0.1777\exp(-0.08114Z_i)]\}^2 \qquad (4.2)$$

where $\alpha = 0.866\sqrt{\dfrac{E_i}{25A}}\dfrac{1}{Z_i^{2//3}} + 0.0378\sin\left(\pi\dfrac{0.886\sqrt{\dfrac{E_i}{25A}}\dfrac{1}{Z_i^{2//3}}}{2}\right)$ and E_i is in keV. This formulation

is directly used in the HITEC model to determine the electronic stopping of any arbitrary heavy ion sampled from the fission fragment data base. Note that this cannot be accomplished by using the SRIM software package itself, which only allows for single ion projectiles of initial energy to be simulated at once

Nuclear stopping is similar in complexity and empiricism to that of electronic stopping. Its formulation develops an interatomic screening potential between the colliding projectile atom and the target atom; numerous screening potentials have been formed theoretically, as summarized in [19]. Of use to this thesis is the the Ziegler-Biersack-Littmark formulation of the screening potential, known as the ZBL Universal Screening potential, $\Phi(x)$, which is inserted into the two-body central force scattering equation with *reduced* variables. The result, which relates the final angle of scatter Θ (radians), in center of mass coordinates, to the impact parameter between the target and projectile, b (unitless) is:

$$\Theta = \pi - 2\int_{x_0}^{\infty} \frac{b\,dx}{x^2\sqrt{1 - \frac{\Phi(x)}{x\varepsilon} - \left(\frac{b}{x}\right)^2}}$$

where ε is the Lindhard reduced energy given by the relation $\varepsilon = \dfrac{32.5A_iE_i[keV]}{Z_iZ_{target}(A_i+A_{target})(Z_i^{0.23}+A_{target}^{0.23})}$ and x is the reduced radius (unitless) between the target and projectile. This relation is tied to the energy transfer per collision by summing over all impact parameters:

$$\left(\frac{dE}{dx}\right)_{nuc} = 2\varepsilon\int_0^{\infty}\sin^2\frac{\Theta}{2}b\,db$$

Given the complicated form of $\Phi(x)$, $\left(\frac{dE}{dx}\right)_{nuc}$ is not readily integrable. It is fit by the following expression:

$$\left(\frac{dE}{dx}\right)_{nuc} = \frac{\ln(1 + 1.1383\epsilon)}{2(\epsilon + 0.01321\epsilon^{0.21226} + 0.19593\sqrt{\epsilon})} \qquad (4.3)$$

This form is only applicable for $\varepsilon < 30$. At higher energies, the nuclear stopping becomes "unscreened" and $\Phi(x)$ assumes a simple coulomb potential. Then, $\left(\frac{dE}{dx}\right)_{nuc} = \frac{\ln\epsilon}{2\epsilon}$. Thus, we see for the stopping power's nuclear component:

$$\left(\frac{dE}{dx}\right)_{nuc} = \begin{cases} \dfrac{\ln(1 + 1.1383\epsilon)}{2(\epsilon + 0.01321\epsilon^{0.21226} + 0.19593\sqrt{\epsilon})} & \epsilon < 30 \\[3mm] \dfrac{\ln \epsilon}{2\epsilon} & \epsilon > 30 \end{cases} \qquad (4.4)$$

Now, with both components of the total stopping power, the projectile's range may be calculated. this is done via a finite differencing method. Using equation (2.1) we see that the total path length traveled by a heavy ion is:

$$s = \int_0^{E_0} \frac{dE}{\left(\frac{dE}{dx}\right)_{nuc} + \left(\frac{dE}{dx}\right)_{el}} \qquad (4.5)$$

One might imagine that by direct integration of (4.5) he might directly obtain the range of the particle. However, in order to calculate the total range, we must account for the directional deviation that occurs due to nuclear stopping near the end of its path length. For this, we multiply (4.5) by the average directional cosine then integrate. We may define the average directional cosine in terms of the particle's energy - dependent angular spread parameter $\tau(E_0, E)$ – a measure of how a projectile's motion changes as it loses energy – then substitute into (4.5) to obtain:

$$\bar{x} = \int_0^{E_0} \frac{\exp[-2\tau(E_0, E)]\, dE}{\left(\frac{dE}{dx}\right)_{nuc} + \left(\frac{dE}{dx}\right)_{el}} \qquad (4.6)$$

Where it may be shown that [19]:

$$\tau(E_0, E) = -\frac{\mu}{4} \int_{E_0}^{E} \frac{dE}{E} \frac{\left(\frac{dE}{dx}\right)_{nuc}}{\left(\frac{dE}{dx}\right)_{nuc} + \left(\frac{dE}{dx}\right)_{el}}$$

where μ is the molar mass ratio of the target atom to the projectile atom. Differentiating (4.6) with respect to the ion's initial energy,

$$\frac{d\bar{x}}{dE_0} = \frac{\partial s}{\partial E_0} \exp[-2\tau(E_0, E_0)] + \frac{\partial \exp[-2\tau(E_0, E)]}{\partial E_0} s$$

Noting that $\tau(E_0, E_0) = 0$,

$$= \frac{1}{\left(\frac{dE_0}{dx}\right)_{nuc} + \left(\frac{dE_0}{dx}\right)_{el}} - \frac{\mu}{2E_0} \frac{\left(\frac{dE_0}{dx}\right)_{nuc}}{\left(\frac{dE_0}{dx}\right)_{nuc} + \left(\frac{dE_0}{dx}\right)_{el}} \int_0^{E_0} \frac{\exp[-2\tau(E_0, E)]dE}{\left(\frac{dE}{dx}\right)_{nuc} + \left(\frac{dE}{dx}\right)_{el}}$$

55

$$= \cfrac{1}{\left(\cfrac{dE_0}{dx}\right)_{nuc} + \left(\cfrac{dE_0}{dx}\right)_{el}} - \cfrac{\mu\bar{x}}{2E_0} \cfrac{\left(\cfrac{dE_0}{dx}\right)_{nuc}}{\left(\cfrac{dE_0}{dx}\right)_{nuc} + \left(\cfrac{dE_0}{dx}\right)_{el}}$$

Which is a linear differential equation for $\bar{x}(E_0)$. Given that $\bar{x}(0) = 0$, we may employ the finite differencing method to obtain the final form of the range algorithm:

$$\bar{x}(E_{i+1}) = \bar{x}(E_i) + (E_{i+1} - E_i)\left(1 - \cfrac{\mu\bar{x}(E_i)}{2E_i} \cfrac{\left(\cfrac{dE_i}{dx}\right)_{nuc}}{\left(\cfrac{dE_i}{dx}\right)_{nuc} + \left(\cfrac{dE_i}{dx}\right)_{el}}\right) \tag{4.7}$$

We now have a means to calculate the range of any heavy ion in any material given the energy dependent electronic and nuclear stopping power formulations. For fission fragments only, we may make a helpful correlation between the charged particle's projected range and its spatially dependent energy deposition. Derived in [49], the spatially dependent energy of an arbitrary fission fragment is:

$$E(x) = E_i\left(1 - \frac{x}{\bar{x}}\right)^n \tag{4.8}$$

Where E_i is the initial energy of the fission fragment (MeV), x is the total distance it has travelled (mm) and n is a unitless scaling factor used for specific ions. For instance, $n = 1$ may be used for light ions, such as alpha particles and protons [50]; $n = 2$ is considered to be most adequate for fission fragments [16, 49]. Equation (4.8) greatly reduces the amount of computation required to track the fission fragment's energy: without it, one must solve equation (2.1) directly for E_f iteratively such that it corresponds with the particle's projected track length $s = l$. We will see this treatment in more detail in the following section on beta particle energy tracking.

4.2.3   Energy Tracking: Beta Particles

Beta particle energy tracking is an inherently simpler problem to that of fission fragments. First, we need only keep track of one *type* of particle, i.e. an electron which has a fixed mass to charge ratio. Second, for the energies we are concerned with, $E_\beta < 10\text{MeV}$, there is only one component to the stopping power: electronic stopping. Then, as alluded to previously, we may find the total distance traveled by a beta particle by integrating equation (2.3) according to formula (2.1) on the energy interval E_0 to E_f in a straightforward manner. However, if we chose some E_β, θ and ϕ to obtain E_0 and l, it is immediately apparent that in order to find E_f, (2.1) must be evaluated repeatedly for values of E_f until the correct path length, s matches that of l. Ultimately, this is a computationally expensive and inefficient process which needs to be improved upon in future work. However, for the purpose of this thesis work, where computational efficiency is not held at a premium, we may employ the direct integration methods in the beta energy tracking model.

4.2.4   The Charged Particle Stopping Power Model

With the means to track fission fragments and beta particles both spatially and energetically throughout the major components of specific TEC geometries, we introduce the charged particle stopping power model component of HITEC. Shown in Figure 4.3 are flow diagrams of a coaxial geometry where the collector emits the ionizing radiation (fission fragments and beta particles). Though Figure 4.3 represents only one of several configurations for a HITEC fuel element, all other configurations will follow the same general process in calculating charged particle energy deposition.

Initially, fission fragment data (FREYA), electron stopping power (NIST) and hydrogen stopping power (SRIM) are provided for all the materials in the system comprising the: the emitter, collector, and interelectrode gas. With this data, provided by the user, the code samples a particle in energy, angle, and centerline distance from the surface of the material where it was generated. Then a *projected* distance, l, of the first material is calculated. l is compared to the particle's range in that material. If l is greater than the particle's range, the particle will deposit all of its energy into the material; if l is less than the particle's range, the particle will have residual energy at the boundary of the next surface. This residual energy is calculated directly by equation (4.8) for fission fragments, and iteratively via equation (2.3) for beta particles. The particle's new energy becomes the input value to calculate its new range in the next material and the deposited is simply the particle's initial energy less its new energy; this is tallied at every material boundary. This process is repeated at each material boundary until the particle has expended all its energy and the entire process may be iterated for an arbitrary number of particles. The output values are the total charged particle energy deposition in the emitter, collector and interelectrode gas. Thus, the primary goal of the charged particle stopping code is to calculate f values such that P_{abs} and P_{fuel} values (equation 2.5) may be directly determined, given a user defined reaction rate (fission or decay). Most unique – and therefore useful – to HITEC reactor power modeling is the energy deposition in the interelectrode gas, as this may be used to calculate plasma parameters pertinent to electrical energy production.

Coaxial Geometry

Collector

Interelectrode space

Emitter R

$L= 2Rcos(\theta)$

$L= L(R,r,\theta)^*$

θ

l d

$L(R,r,\theta,\phi)^* = \csc\phi \sqrt{R^2 + r^2 - 2R^2\sin^2\theta - 2\sqrt{R^2\cos^2\theta\,(2r^2 - R^2\cos 2\theta)}}$

Read in FREYA ff data and Hydrogen dE/dx data

Sample a new ff (Z, A, E_0). Assign position (d) and direction (θ)

$l = d/\cos\theta$

Calculate range in fuel using modified PRAL

$l <$ range? (Collector)

yes

$E_{new} = E_0\left(1 - \left(\frac{l}{range}\right)^2\right)$

$E_{dep,c} = E_0\left(1 - \left(1 - \left(\frac{l}{range}\right)^2\right)\right)$

Fission fragment flux energy-angle distribution at surface of collector

no

Deposited in collector

Makes it into interelectrode space: Calculate new range in gas

Energy deposition data input for plasma modeling

$E_{dep,g} = E_{new}\left(1 - \left(1 - \left(\frac{l}{range}\right)^2\right)\right)$

$E_{dep,e(c)} = E_{new}\left(1 - \left(\frac{l}{range}\right)^2\right)$

$E_{dep,g} = E_{new}$

$E_{dep,c} = 0$

$\theta < \sin^{-1}\frac{r}{R}$

yes (toward emitter) $L= L(R,r,\theta)^*$

(toward collector) **no**

$L= 2Rcos(\theta)$

$L+l <$ range? (gas)

no

yes

Coaxial Geometry

Collector

Interelectrode space

Emitter R

$L= 2Rcos(\theta)$

$L= L(R,r,\theta)^*$

θ

l d

$L(R,r,\theta,\phi)^* = \csc\phi \sqrt{R^2 + r^2 - 2R^2\sin^2\theta - 2\sqrt{R^2\cos^2\theta\,(2r^2 - R^2\cos 2\theta)}}$

$l(R,r,\theta,\phi)^* = \csc\phi\left[(d - R)\cos\theta + \sqrt{\frac{1}{2}\left[R(R + 2d) - d^2 + (d - R)^2\cos 2\theta\right]}\right]$

Read in NIST electron dE/dx and range data for collector and gas

Assign energy (E_0), position (d), and direction (θ) to beta.

$l = l^*$

select range based on assigned energy (E_0)

$l <$ range? (Collector)

yes

$l = \int_{E_0}^{E(l),} \left(\frac{dE}{dx}\right)^{-1} dE$

$E_{new} = E(l)$

$E_{dep,c} = E_0 - E(l)$

β flux energy-angle distribution at surface of collector

no

Deposited in collector

Makes it into interelectrode space: select range in gas based on E_{new}

Energy deposition data input for plasma modeling

$E_{dep,e(c)} = E(L)$

$E_{dep,g} = E_{new} - E(L)$

$E_{dep,g} = E_{new}$

$E_{dep,c} = 0$

$\theta < \sin^{-1}\frac{r}{R}$

yes (toward emitter) $L= L(R,r,\theta)^*$

(toward collector) **no**

$L= 2Rcos(\theta)$

$L+l <$ range? (gas)
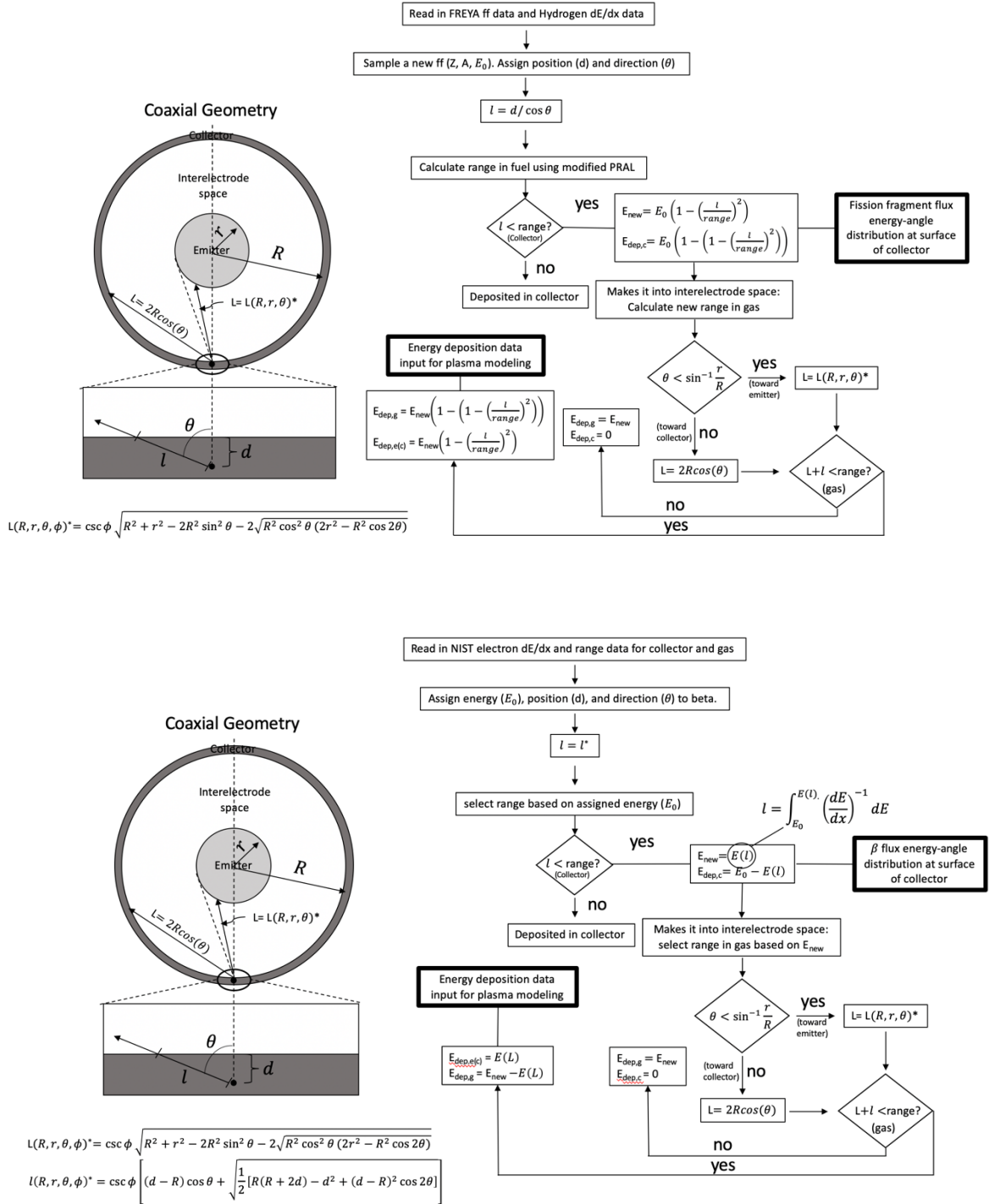
no

yes

Figure 4.3 Energy deposition model flow diagram for coaxial TEC geometries, where the type of charged particle is a) fission fragments and b) beta particles.

4.3 Plasma Model

With knowledge of the relative charged particle energy deposition values in the interelectrode gas (i.e. f from equation (2.5)), we may calculate plasma parameters $T_{e,E}$, $n_{e,E}$,

58

$T_{e,C}$, and $n_{e,C}$ given a fission (or decay) rate ionization, $\phi_{th}\Sigma_{th}$ $(n_{fuel}\lambda)$ and parent gas parameters, n_a, $w_{i,a}$ and T_a (at the emitter an collector surfaces) by directly solving (2.16) for T_e then inserting this value of T_e into (2.10) where $f^+ = \frac{P_{abs}}{w_{i,a}}$. As the plasma parameters are a function of P_{abs}, they will vary spatially throughout the reactor. Given the general heterogeneity of most nuclear reactors, it is best use a neutronics code, such as Monte Carlo Neutral Particle (MCNP) or Standardized Computer Analysis for Licensing Evaluation (SCALE) to determine this spatial dependence. This may be achieved by spatially zoning the reactor core and tallying the fission rate of these zones. Then, by normalizing the zones to that which fissions most and assigning this zone an initial P_{abs}, one may determine the spatially dependent P_{abs}.

Fuel temperature, on the other hand, is more complex. Though it is possible to calculate the emitter and collector temperatures by using the spatially dependent fuel heating rate via equation (2.6) then applying relevant heat transfer equations, we may not make these calculations meaningfully without more sophisticated heat transfer models. The emitter and collector temperatures hinge not only on fuel design (e.g. use of central voids, varying enrichment, dimensions, etc.) but also heat transfer methods and temperature dependent thermal conductivity; such a problem would be more adequately approached by more sophisticated thermal hydraulics analyses beyond the scope of this thesis.

To remedy the absence of an adequate thermal model in the HITEC code, we turn to recent experimental and computational data that accurately models axially dependent temperature profiles for thermionic fuel elements [51]. In the HITEC code, we scale the peak temperature of the emitter, input by the user, according to [51] along several axial points in order to estimate total thermionic emission from a HITEC fuel cell. It is worth mentioning that the user should make use of the following approximate centerline fuel temperature, T_{cl} (K) calculations to guide his initial choice in fuel dimensions:

$$T_{cl} = \begin{cases} T_{wall} + \dfrac{P_{fuel}t^2}{k_{fuel}} \\ T_{wall} + \dfrac{P_{fuel}r^2}{4k_{fuel}} \end{cases} \qquad (4.9)$$

Where t and r are the thickness and radius (cm) of an infinite planar and cylindrical fuel element, respectively, T_{wall} is the fuel wall temperature (K) and k_{fuel} is the thermal conductivity of the fuel (W cm^{-1} K^{-1}). This approximate solution to the heat conduction equation assumes a uniform, volumetric heating rate with no other heat sources. Equation (4.9) is most helpful to employ when the user establishes some P_{abs} criteria to attain a certain n_e and T_e in a HITEC fuel cell and must know the corresponding fuel dimension that does not violate fuel centerline temperature limits yet maintains a high enough wall temperature for adequate thermionic emission.

4.4 Single TEC cell output

A single TEC cell output is given by evaluating equation (3.14). Given T_E and ϕ_E, J_{th} is directly calculated by the Richardson Dushman equation (3.3) and $J_{e,E}$ $(I_{e,E} = A_E J_{e,E})$ by equation (3.13). Using the electrical definition of power, equations (3.15) and (3.16) are

multiplied to produce a power density vs. voltage curve from which we may obtain the maximum value. This initial power density calculation defines an output voltage, V_{out}, which is assumed to be the uniform across an entire cell. To calculate power density off peak values, the RHS of equation (3.16) is evaluated for the new values of $J_{e,E}$ and J_{th} and compared to the peak values: for $\frac{J_{e,E}}{J_{th}} > \frac{J_{e,E,peak}}{J_{th,peak}}$ the diode is undercompensated, therefore the current density is solved by equation (3.14) and for $\frac{J_{e,E}}{J_{th}} < \frac{J_{e,E,peak}}{J_{th,peak}}$ the diode is undercompensated and the total current density is solved by evaluating equation (3.15). Thus, the total output of a TEC cell is determined by:

$$P_{out} = V_{out} \sum_{i=1}^{N} J_i(z_i)A_i \tag{4.9}$$

Where $J_i(z_i)$ [A cm^{-2}] and A_i [cm^2] are the axially dependent current density at position, z_i [cm], and area of assessment respectively.

4.5 Reactor Scaling

Reactor scaling, i.e. calculating multiple TEC cell outputs, is best accomplished by means of using a neutronics modeling code, such as MCNP, SCALE, etc. Since reactor scaling will differ amongst users, in both rigor and baseline assumptions, we outline general guidelines.

Fission plasma deposition depends on the spatially dependent fission rate near a solid-gas boundary. Therefore, its accuracy strongly depends on the spatial resolution with respect to the particle's range. For high energy electrons, where the range in a solid is approximately 1 mm, the rate at which these electrons are being generated (and therefore the fission rate, given steady state conditions) should be known to a spatial resolution of at least a mm length scale. This length scale is readily approached by a volumetric flux tally, e.g. the volumetric fission heating rate tally in MCNP. By zoning a nuclear reactor core (axially and radially) with the volumetric fission heating tallies, these values may be directly scaled to some R ($= P_{fuel}E_{fiss}$) assigned by the user. Fission fragments have a range around 500 times less than that of high energy betas; this length scale lends itself more adequately to a surface flux tally, e.g. the neutron flux average over a surface given such small spatial dimensions ($\sim 5\mu m$). A similar zoning process can be used, then corresponding fission rate R [fissions events cm^{-3} s^{-1}] through those surfaces may be calculated by integrating the product of the energy dependent neutron flux and macroscopic fission cross section over the entire neutron energy spectrum:

$$R = \int_0^{\infty} \phi(E)\Sigma(E)dE \tag{4.10}$$

Where $\phi(E)$ is the energy dependent neutron flux [n cm^{-2} s^{-1}] and $\Sigma(E)$ is the energy dependent macroscopic fission cross section [cm^{-1}]. Here, we assume that over a spatial variation on the order of a fission fragment's range in a solid (5 μm) both the material density and spatial dependent neutron flux both remain constant. Such an assumption is valid for nuclear reactor

scale systems whose material densities and spatial dependent neutron fluxes only vary significantly on the mm and cm length scales, respectively.

As a final note, scaling HITEC results to nuclear reactor systems can only be as accurate as the radiation (neutron, gamma, electron) and thermal transport models involved with this scaling: especially near the electrode surface – plasma boundary where thermionic emission occurs. Thermionic emission phenomena under nuclear reactor conditions has remained virtually uninvestigated experimentally or theoretically to date, however its accurate understanding will be vital to assessing a HITEC reactor's performance .

Chapter 5: Example Applications and Conclusions

5.1 GM Fission Foil Experiment: the Importance of Accurate k_{dr} Values

One of the simplest benchmarks for the HITEC code may be made on fission foil plasma excitation studies [52] in the earlier years of the GM study. The experimental setup, depicted in Figure 5.1 was very simple: ionization tubes of different fill gases (Argon, Neon, Xenon and Ne:Ar $(1:10^{-3})$ penning gas) with thin uranium foils were placed in a nuclear reactor. One of the electrodes' was swept across a voltage range in order to obtain an I-V curve which is proportional to the source rate by:

$$I \propto f^{+3/4}V^{1/2}$$

The study used 93% enriched uranium foils bonded to nickel (5.4% wt.) such that the average density of the foil was 17.54 g cm^{-3} and the total macroscopic fission cross section was 23.4 cm^{-1} [53]. The thermal neutron flux was 1.2 x 10^{13} cm^{-2} s^{-1}, giving a fission rate density (R) of 2.76 x 10^{14} cm^{-3} s^{-1} ($P_{fuel} = 7400$ W cm^{-3}). Running the planar HITEC charged particle deposition model with the parameters from [53] for fission fragments only, we may calculate the ionization rate (f^{+}) and therefore P_{abs} for each gas. Then, resulting P_{abs} may be input into the plasma model to calculate T_e and the resulting n_e.

We show our results compared to the experimental results of [53] in Table 5.1. As can be seen, HITEC's ionization source rate density results are in excellent agreement with those found experimentally: all within 5% of experimental values. Calculations for the electron density differ markedly, on the other hand. The disparity in n_e calculations via equations (2.16) and (2.10) are due to the use of differing values of the dissociative recombination coefficient, which is known to be a function of both parent gas and electron temperatures.
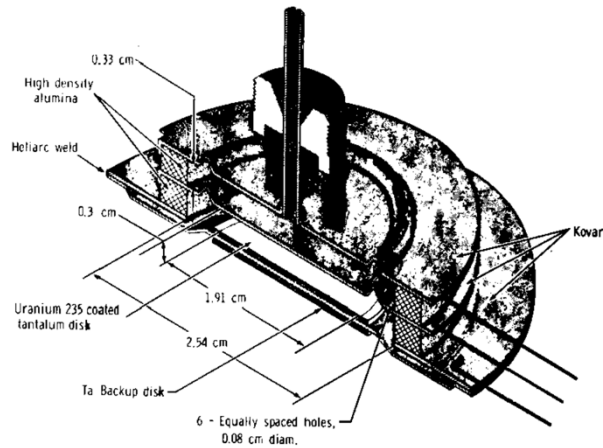
FIG. 3. Ceramic–metal ionization tube.
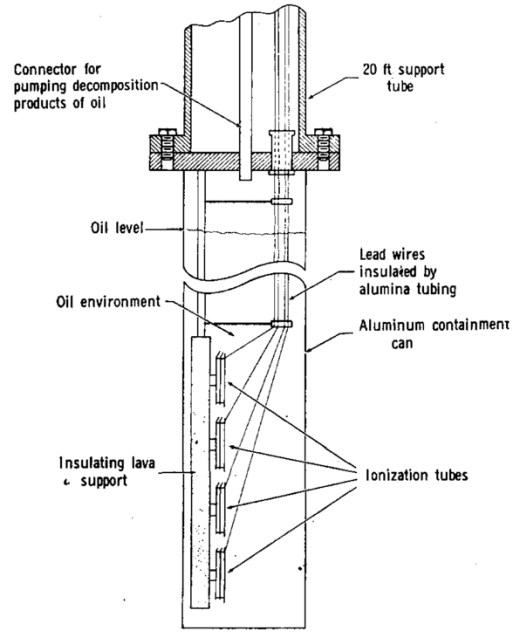
FIG. 6. Schematic of assembly for inpile operation of the ionization tubes. Inside the 4-ft containment can a lava insulator is shown supporting four ionization tubes.
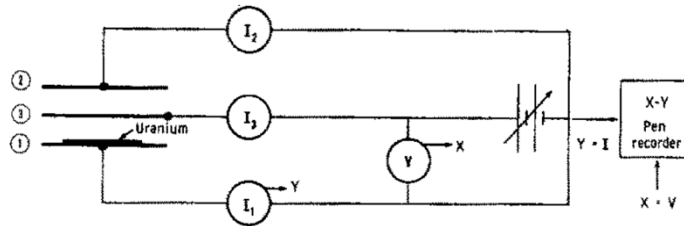
FIG. 7. Circuit for ion chamber experiments.

Figure 5.1 Fission foil ionization tube experimental configuration from [53].

Table 5.1 Experimental data and HITEC model calculations for the ionization source rate density and electron density for gas pressures of 240 torr, ϕ_{th} = 1.2 x 10^{13}cm^{-2} s^{-1} and temperature 400K

Gas	f^+ [cm^{-3} s^{-1}] x 10^{16}		n_e [cm^{-3}] x 10^{11}		$k_{dr,GM}/k_{dr,HITEC}$
	HITEC	GM (experimental)	HITEC	GM (calculated)	
Neon	1.7	1.8	4.5	2.9	2.7
Argon	3.7	3.6	5.3	2.3	5.2
Xenon	8.4	8.1	4.5	2.4	3.3

Study [52] assumed the electrons to be in equilibrium with the parent gas at 300K and used the recombination coefficients from [53]; this leads to electron density calculations at least a factor of 2 lower than those calculated with current dissociative recombination values and ultimately pigeonholed further research into fission plasmas that used penning gases Ne:Ar and Ar:Cs exclusively. For example, using HITEC electron density calculation for xenon of n_e = 4.5 x 10^{11} cm^{-3} and T_e = 6380 K, is sufficient to transmit thermionic current densities of at least 1.5 A cm^{-2} and consequently > 2-3 W cm^{-2}. This calculation is made without gas temperature

corrections, which would increase n_e substantially. Though penning gases may ultimately lead to higher performance diodes, single component gases should not be dismissed as they may offer equally beneficial operational simplicity for reactor-scale systems.

5.2 TEC Diode P-V Characteristics: Benchmarking the HITEC Model

It is important to benchmark the complete HITEC model against experimental data. Here, we quantify the roles of fission fragments and their subsequent beta decay on TEC plasma ionization in fuel element-scale systems. We compare the HITEC model simulation results to experimental in-core data for unclad, BaO-UO$_2$-W based thermionic emitters from the GM study. One of HITEC's limitations in its applicability to this data is that HITEC's electron transport module is only experimentally verified for single species noble gases at low temperatures (<600K). The in-core thermionic diodes for the GM experiment, on the other hand, used an Ar:Cs penning mixture at a much higher temperature ($T_a \sim$ 1450K); these conditions deviate far from those accounted for in a single species, low gas temperature electron transport model. However, given the relatively high pressure and low power density (<< 1 W cm^{-3}) nature of the plasma under consideration, the fundamental assumptions made in Chapter 3 in formulating the electron transport model are still correct, thus solving equations (2.16) and (2.10) for T_e and n_e is valid.

Furthermore, where ϕ_E and ϕ_C may be inferred by the out-of-core thermionic emission data, they were not measured in-core. As a result, ϕ_E and ϕ_C remain unknown for in-core experiments. Since ϕ_E and ϕ_C were never experimentally measured in-core, our analysis will proceed in two parts. First, we demonstrate the effects of varying ϕ_E and ϕ_C separately on power output. Then we empirically fit ϕ_E and ϕ_C in tandem to best fit the experimental data deriving from the P-V curves. Finally, we test the relative sensitivity of the parameter fit to P_{abs}. Thus, we will see how all these factors (both plasma and electrode properties) affect HITEC's overall accuracy in determining power characteristics and shed light on both experimental and theoretical future needs in understanding these systems further.

Table 5.2 summarizes the parameters of electron transport tube 4 (ETT-4) from [14] under consideration for modelling in HITEC. A more detailed description of the experimental setup may be found in the study. Most important to note in Table 5.2 is the decrease in Σ_f [cm^{-1}] at the surface of the fueled emitter compared to its volume averaged value. This depression is due to the neutron absorption that occurs in samples with dimensional thicknesses similar to that of the mean free path of absorption ($1/\Sigma_a$ [cm]) in-core. As the total neutron flux through a surface is the summation of directional currents at that surface, the directional current component of the neutron flux that travels *through* an absorbing material will be attenuated by that material some factor $\exp(-\Sigma_a d)$ where d is the thickness of the material. Since fission fragment plasma ionization is concerned only with length scales very near the emitter surface (on the order of its range, $\bar{x}$) this self-shielding effect significantly attenuates fission fragment production: by at least a factor of two. This resulted in a depressed P_{abs} and consequently lowered the expected T_e and n_e values. Conversely, for β^- decay energies ≥ 1 MeV, $\bar{x}$ exceeds the thickness of the emitter and we may simply take the volume averaged Σ_f for β^- ionization in HITEC simulations.

Table 5.2 Parameters for ETT-4 used in HITEC Model

Emitter:	
Material, ϕ_E	BaO-UO$_2$-W, 3.05eV
Thickness	0.137 cm
Density	10.8 g cm^{-3}
Σ_f (at surface)	2.05 cm^{-1}
Σ_f (total)	4.45 cm^{-1}
Σ_a (total)	5.93 cm^{-1}
Collector material, ϕ_C	Mo, 2.65 eV
Emitter temperature	1675K
I_{th} (A)	~0.5
Collector temperature	1150K
ϕ_{th}	5 x 10^{12} cm^{-2} s^{-1}
Gas composition/pressure	Ar:Cs (varying composition)/100 torr
Electrode Area (cm^2)	2.55

The HITEC simulation results are summarized in Table 5.3. For the β^- decay energy spectra, we used an experimental fission fragment spectrum [55], which spans from $0 < E_{\beta^-} < 10$ MeV. Comparing the results, it is apparent that for the diodes under consideration, the power deposition due to β^- decay contributes less than 4% to the total charged particle power deposition. Though, given n_e's proportionality to $\sqrt{P_{abs}}$, β^- decay actually adds 20% to the total n_e, however this does not change the device's power output characteristics significantly.

Table 5.3 Summary of HITEC model calculations for ETT-4

	Fission Fragments	β^- decay (fission fragment spectrum)	Total
P_{abs} (W cm^{-3})	0.0059	0.0002	0.0061
T_e (K)	-	-	3100
k_{dr} (cm^3 s^{-1})	-	-	4.68 x 10^{-8}
$w_{i,a}$ eV	28.8	26.4	28.7
n_e (cm^{-3})	1.65 x 10^{11}	3.17 x 10^{10}	1.68 x 10^{11}

Particularly influential to the power output is the thermionic emission current, and therefore ϕ_E. This is clearly reflected in the P-V curve in right of Figure 5.2a where the diode's experimental output power in the power producing region (i.e. when the collector is negatively biased with respect to the emitter) is compared to those obtained by HITEC simulation. Varying the emission current from 0.5 – 1.25A corresponds to a proportionately increased peak power output for a given voltage, while slightly lowering its peak output voltage; varying ϕ_C from 2.55 – 2.65 eV tended to slightly increase both power output and peak output voltage as well as broaden the P-V curve. Combining these two characteristics to find a best fit curve yielded an emission current ranging from 0.65 – 0.69 A, which is about 40% more than the out-of-core emission current measurement and ϕ_C between 2.50-2.55 eV.
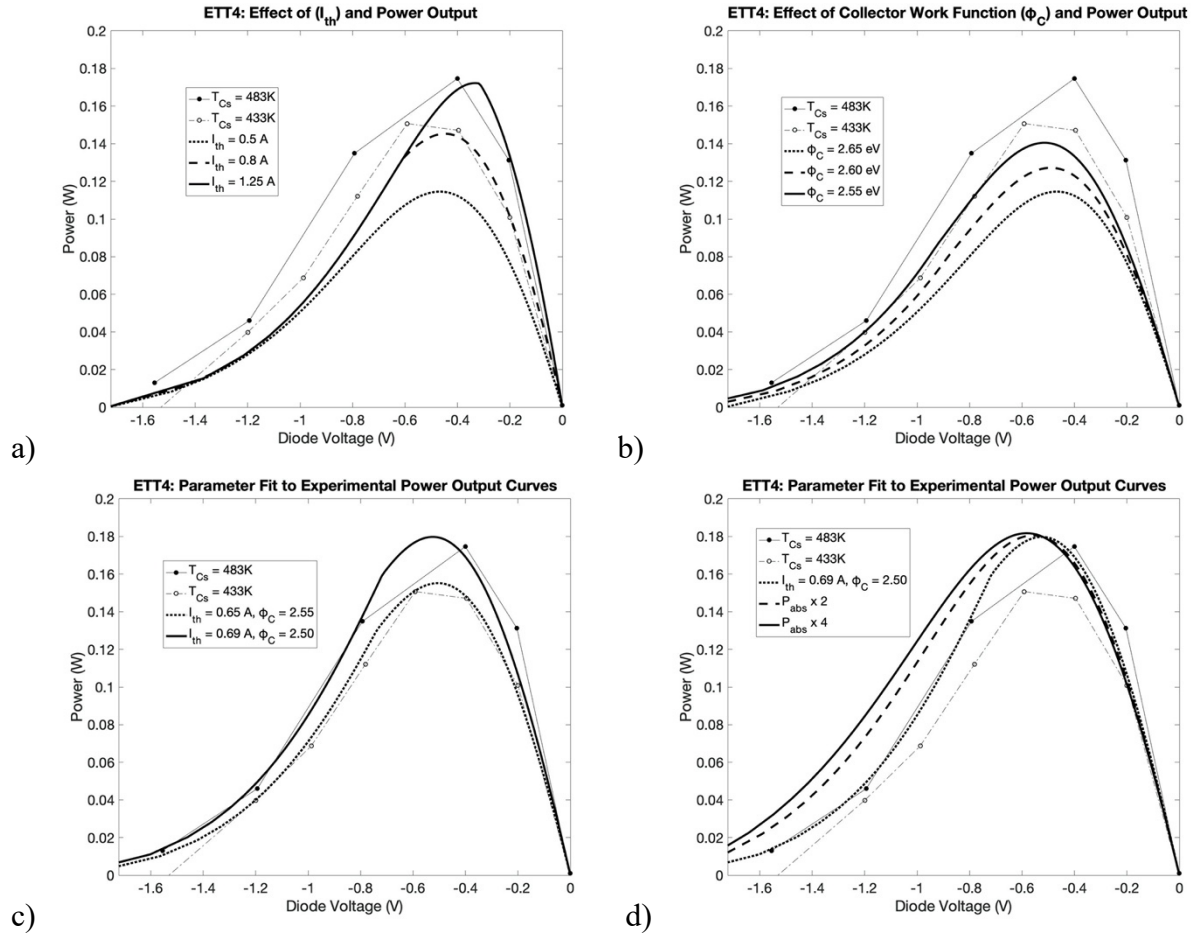
Figure 5.2 HITEC model comparison to experimental electron transport tube data. Effects on P-V curves are shown for modifying a) I_{th}, b) ϕ_C and c) Parameter fitting both I_{th} and ϕ_C, d) P_{abs}.

In general, we see very good agreement between the HITEC calculations and experimental data in the power producing region so long as we appropriately assign ϕ_E (I_{th}) and ϕ_C. Then, we may conclude that the HITEC code can accurately calculate power characteristics for fission plasma based thermionic energy converters, given accurate in-core experimental data for ϕ_E and ϕ_C exists.

A possible cause for the apparent increase in thermionic emission for the fueled, unclad emitter could be due to the nuclear processes occurring very near the surface of the emitter, including but not limited to:

1. Compton and Photelectric (PE) electron production by reactor generated gamma photons. ($1\text{keV} < E_e < 10\text{MeV}$)
2. Auger electron processes from production from fission fragment decay near the emitter surface and other phenomena. ($10\text{eV} < E_e < 1\text{keV}$)
3. Convoy electrons as multiple charge state fission fragments pass the emitter-interelectrode gap barrier. ($E_e < 100\text{eV}$)

The three mechanisms potentially affecting thermionic emission are listed in order of spatial sensitivity. Not surprisingly, the ordering also corresponds to the decreasing average electron energy (parenthesized in the list) resulting from each process, as the electron energy deposition increases strongly for decreasing electron energy (see Figure 2.2).

Though it is certain that these processes also increase plasma ionization, we argue that their overall contribution to increasing device *performance*, i.e. the output power, is not significant for the gas pressures considered ($<$ 1atm). Consider the ETT- 4 conditions (gas pressure $\sim$ 100 torr) where the ionization rate, $f^+ \sim 2$ x 10^{15} ionizations cm^{-3} s^{-1} ($P_{abs} = 0.0059$ W cm^{-3}). First, we note that the total ionization due to fission fragment beta decay is under 4% and argue by figure 5.2d that this additional contribution to P_{abs} does not dramatically change the devices output power characteristic. Given that Compton and PE electrons are produced roughly in the same energy range, the average macroscopic cross section for this interaction, $\Sigma_{compton}$, in a typical fuel element ($\rho \sim 10$ g cm^{-3}) is roughly $1 - 10$ cm^{-1} which is similar to Σ_f in the fuel. This implies that a gamma flux roughly equivalent to the neutron flux is required to yield an ionization rate comparable to that of fission fragment beta decay, which we already determined was not significant to increasing device performance. For the lower energy electrons produced in (2) and (3), although these electrons have a much higher energy deposition (by a factor of $10^2 - 10^3$) this is outweighed by a smaller fuel volume fraction ($10^{-3} - 10^{-4}$) that may contribute to plasma ionization, which is limited to the range of fission fragments. Thus, for sub atmospheric pressures, processes $1 - 3$ will not enhance (or decrease) device performance.

Though it is specifically mentioned in [14] that the electron transport tubes – especially the electrodes – were not optimized for power production, it is instructive to compare (calculated) optimized conditions that of experimental in order to show the paramount importance of emitter collector properties. And by "optimal" in this instance, we mean optimal electrode properties (vice the plasma), such that maximum emission currents are realized with maximum output voltages. We establish optimal conditions by adjusting the cesium concentration in order to lower ϕ_E and ϕ_C (at a given T_E and T_C) according to Figure 5.3. for $T_E = 1675$K, and a realistic ϕ_E value of 2.8eV, this yields a $T_{Cs} \sim 600$K. Correspondingly, for $T_C = 900$K, $\phi_C \sim 1.8$eV and $\Delta\phi \sim 1$eV. Here, we have lowered T_C sufficiently so that there isn't appreciable thermionic emission, or back current, from the collector as was seen in [14], where T_C was as high as 1225K ($I_{back} = 12$A!)

Table 5.5 and Figure 5.4 shows the results of these parameter changes. We see that by modest changes to the electrode properties varying the cesium concentration and adequate control of the collector temperature, we would see close to an order of magnitude performance increase out of the diode. Lowering both the collector work function and temperature with respect to the emitter are crucial in this optimization; by practice, this is achieved by the use of Cs additive which favorably lowers work functions of materials according to Figure 5.3. For example, a "typical collector" in TEC devices, Mo, may have its work function lowered to as low as 1.6 eV. Therefore, the optimized conditions suggested in Table 5.5 are by no stretch of the imagination.

Table 5.5 HITEC values for optimized conditions of ETT-4

	Experimental	Optimized	Relative Change
T_E (K)	1675	1675	$\leftrightarrow$
T_C (K)	1125	900	$\downarrow 0.2$
ϕ_E	~3.05 eV	2.7 eV	$\downarrow 0.11$
ϕ_C	~2.6 eV	1.8 eV	$\downarrow 0.3$

   The following conclusions may be drawn from comparing HITEC model results to the experimental data from [14]:

1. Fission fragments are the main contributors to fission based plasma ionization where the fuel thickness is comparable to the neutron mean free path of absorption and where gas pressures are low (<1atm).
2. The electron temperature is substantially greater than those predicted in the electron transport model of the GM [14], who predicted $T_e \sim 2000K$ for $P_{abs} = 0.07$ W cm^{-3}. This is evidenced by both the HITEC model results and the experimental data.
3. There is cause for nuclear effects to play a role in enhancing thermionic emission from unclad thermionic fuel elements. This should be investigated in future work.
4. P-V curves are very sensitive to ϕ_E, and ϕ_C. In order to adequately model practical devices, these values must be known to a high degree of accuracy under in-core conditions.
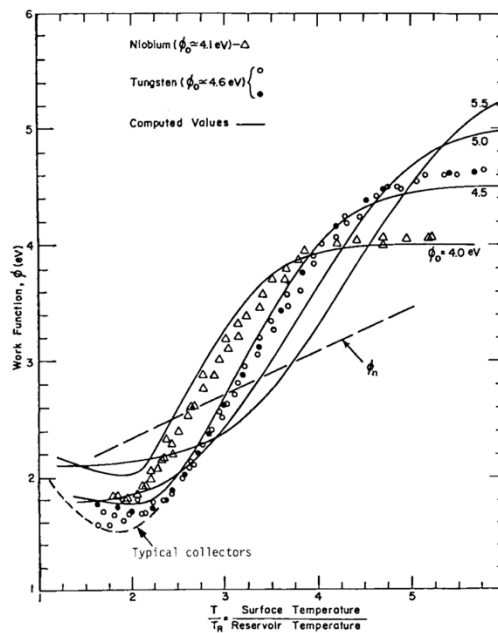
Figure 5.3 Work function – cesium reservoir temperature relation. Reproduced from [40].

   Lastly, The electron transport tubes of [14] were highly un-optimized for power production. Had more efforts been made to increase thermionic electron emission and lower the collector work function and temperature, these diodes may have achieved power outputs nearly an order of magnitude greater than obtained during the experiment for the chosen emitter temperature (1675K). Even higher performance can be achieved for higher T_E, P_{abs}, and A.

ETT4: Optimized vs. Experimental Power Output Curves
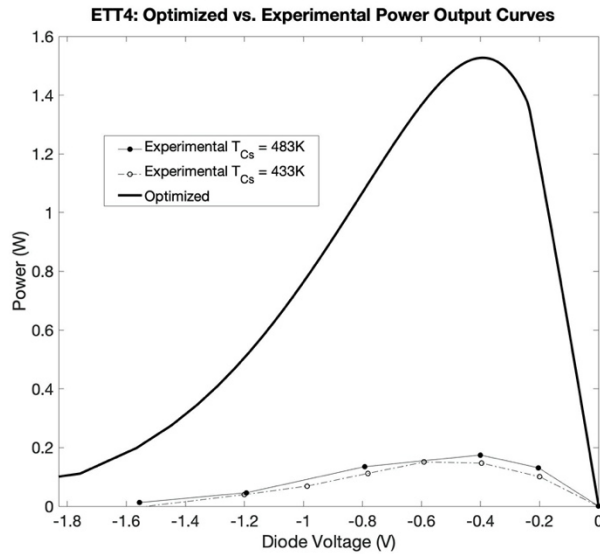
Figure 5.4 Calculated optimized conditions for ETT-4 in comparison with experimental conditions. It is seen that the important factors in raising the power output are raising the emission current (by lowering ϕ_E) and contact potential $\Delta\phi$ which essentially shifts the I-V curve leftward into the power producing quadrant.

5.3 Nuclear Reactor Model

5.3.1   Core Design

Having validated the HITEC model on in-core experimental data for single TEC cells, and with power optimization in mind, we may move forward in modeling the power characteristics of an in-core thermionic nuclear reactor based on fission excited plasma thermionic energy conversion. Here, we present a basic model of a heat-pipe nuclear reactor, designed in the well known MCNP code, with 271 coaxial thermionic fuel elements and expected thermal output of roughly 2.5 MW$_{th}$. The reactor's core emulates the extensively ground tested space nuclear reactor, TOPAZ II [56]: it is moderated by Zirconium Hydride (ZrH$_{1.85}$), beryllium reflected, and reactivity controlled by ^{10}BC$_4$ insets in rotatable beryllium drums. The reactor differs most noticeably in both its cooling and fuel element designs. To the former, cooling is achieved via passive Sodium-Haynes alloy heat pipes rather than actively pumped liquid NaK (for TOPAZ – II) for both operation simplicity and efficiency; to the latter, we discuss in the following section. The cross sectional views of the core and an individual fuel cell are shown in Figure 5.4. A more detailed SOLIDWORKS drawing of the fuel cell is also pictured to demonstrate the more complex features of the collector, whose geometry maximizes its surface area with respect to the emitter.

a)   b)
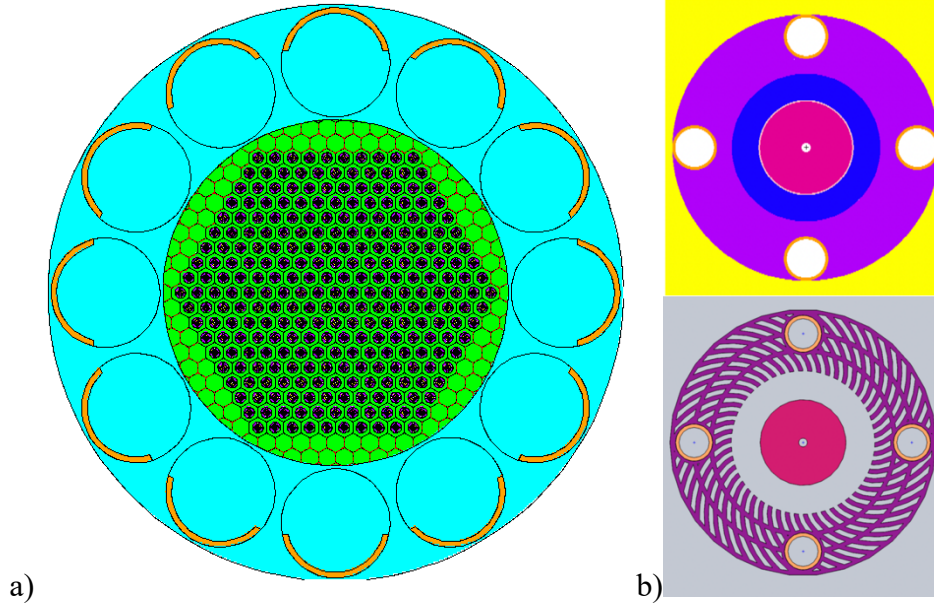
Figure 5.2 a) Reactor core with control drums configured for maximum reactivity and b) fuel element design in MCNP (top) and in SolidWorks (bottom).

5.3.2   Emitter

The emitter is comprised of a two layer, unclad fuel which serves to ionize a plasma via fission fragment ionization and produce heat for thermionic emission. $U(18.5)O_2$ was chosen to be the bulk material; to reduce the self shielding effect and maximize fission fragment emission at the surface, a 50μm $U(90)O_2$-W based ceramic-metallic (CERMET) layer, similar to [14] (without BaO) served as the outer layer given its previously demonstrated performance in cesiated environments and applications to adjacent fields in space nuclear power, such as nuclear thermal propulsion[57]. In a properly cesiated environment, the emitter's work function drops to approximately 2.7 eV: this corresponds to an emission current density of 2 – 20 A cm^{-2} in the temperature range 1600K – 1800K. The emitter diameter was chosen to be 6 mm with a central fuel void of 2.8mm. This fuel dimension is thick enough so that sufficient heating for thermionic emission is achieved, yet thin enough to compensate for the high thermal gradients that occur in the fuel meat. We show this by perform a heat balance, using equation (3.4), discounting joule heating:

$$Q_{tot} = Q_{em} + Q_{rad} + Q_{cond}$$

$$= \frac{I_{th}}{e}(\phi_E + 2kT_E) + \sigma\epsilon(A_E T_E^4 - A_C T_C^4) + \frac{kA_{Lm}(T_E - T_C)}{r_C - r_E}$$

where $A_{Lm} = \frac{2\pi L(r_C - r_E)}{\ln{r_C}/{r_E}}$ is the logarithmic mean area (cm^{-2}) and r_C and r_E are the radii of the collector and emitter (cm), respectively and k is the thermal conductivity of the argon gas at $T =$

$\frac{T_E + T_C}{2}$ [63]. Using $T_E = 1850$K, $T_C = 900$K, $\phi_E = 2.7$ eV, $\epsilon = 0.2$, $L = 100$ cm, $r_E = 0.315$ cm, $r_C = 0.5$ cm, and $k = 6.5$ x 10^{-4} W cm^{-1} K^{-1}. Obtaining $I_{th} = J_{th}A_E$ via the Richardson Dushman equation, we find that $J_{th} = 18$ A cm^{-2}, and calculation yields a power density requirement, $P_{fuel} = \frac{Q_{tot}}{V_E}$, where V_E is the fueled emitter volume (cm^{-3}) is equal to roughly 500 W cm^{-3}. Using equation (4.9) and $k_{fuel} \sim 0.05$ W cm^{-1}K^{-1}, we calculate $T_{cl} = 2075$K in the case of a voidless cylindrical fuel element, which is safely below its melting point ($T_m \sim 3100$K) the actual temperature would actually be significantly lower given the fuel void.

5.3.3   Collector

The collector is comprised of a material that fits the following desirable criteria. It will:

1. Minimally affect reactor core neutronics (i.e. low absorption cross section and sufficiently high mass number).
2. Electrically conductive so that it may couple to auxiliary power to provide additional plasma ionization at the collector surface not immediately exposed to emitter ionization.
3. Have a significantly larger surface area than that of the emitter.
4. Exhibit a significantly reduced work function in a cesiated environment.

To satisfy these four design objectives simultaneously, especially objectives 2 and 4, the we chose Zirconium coated with molybdenum (~10 μm), given zirconium's small thermal neutron capture cross section and molybdenum's high electrical conductivity and precedence as a collector surface for nuclear and non-nuclear TEC devices. To increase the apparent surface area of the collector, we chose an involute-type design as shown in Figure 5.2b; the wall and gap thickness between involutes are 0.3mm which allows for bulk properties to preside in the gap (sheath width is approximately 20 – 40 μm). Not pictured are microholes between plasma regions such that the collector plasma is electrically connected to the emitter plasma. These holes should be larger than the plasma sheath width by several factors (~50 μm) .

5.3.4   Interelectrode gap

The most important aspects of the interelectrode gap, i.e. the space between the emitter surface and the collector outer surface, are its width, gas composition and pressure. The width must be sufficiently small so that adequate power density, P_{abs} is achieved for plasma ionization, yet large enough to preclude physical contact between the emitter and collector due to irradiation swelling; this was a major design challenge for previous devices [10]. Considering these criteria, we chose a 2 mm gap width. We use an Ar:Cs penning mixture, given the previous successes in using Ar:Cs penning mixtures for fission plasmas and existing experimental data on which the HITEC model has been verified [14]. Given a desired current density on the order of $1 – 10$ A cm^{-2} and using the work function-cesium reservoir temperature relation[40] reproduced in Figure 5.3 we determined a cesium reservoir temperature of ~600K, which corresponds to a partial pressure of cesium to be approximately 3 torr via the relation [64]:

$$p_{Cs} = 2.45 \times 10^8 T_R^{-1/2} \exp\left(-\frac{8910}{T_R}\right)$$

where p_{Cs} is the pressure of Cs (torr) and T_R is the cesium reservoir temperature (K). As for the argon pressure, we chose 380 torr as this allows for adequate ionization while still allowing for an elevated electron temperature ~ 4000K.

5.3.5 Neutronics and Criticality

Given the reactor's general features, its core neutronics were modeled in MCNP. The results are shown in Figure 5.3.

a) b) c) d)
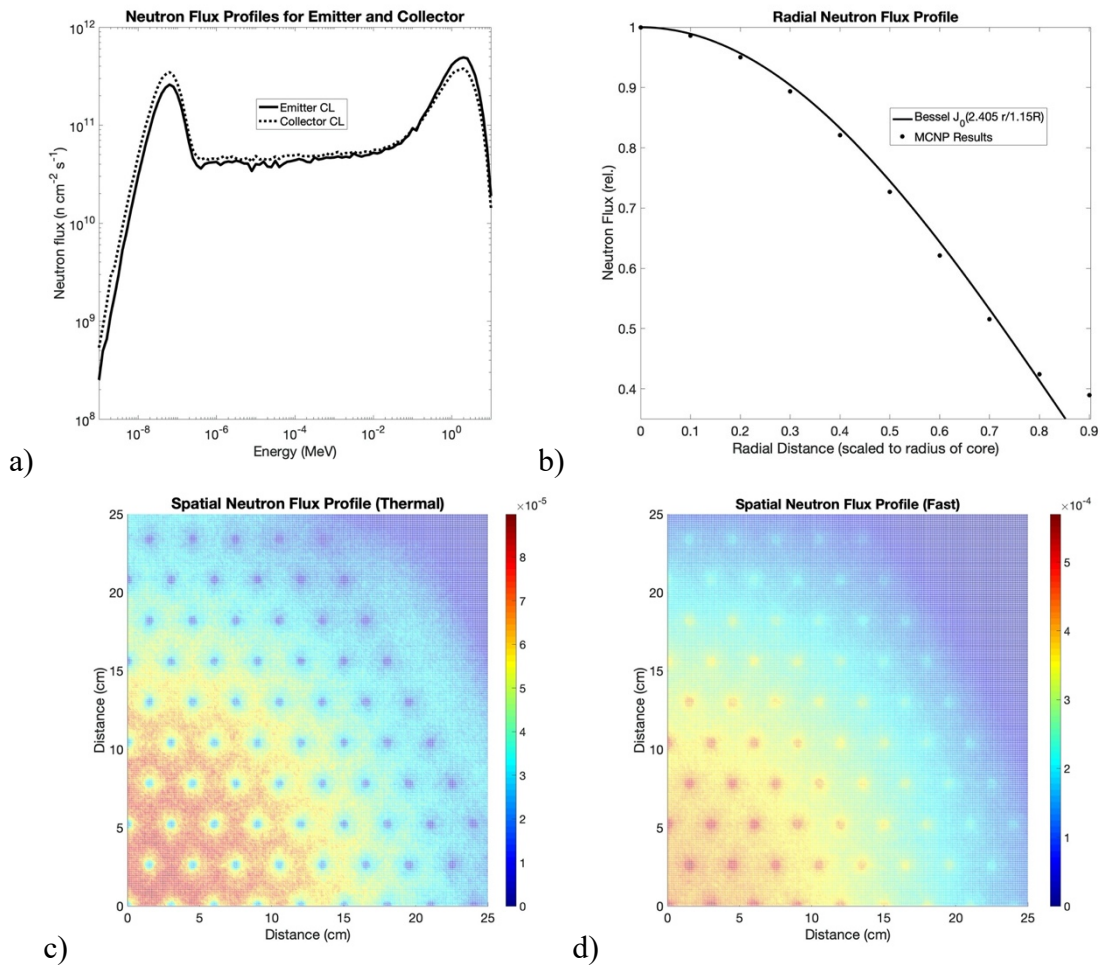
Figure 5.3 Reactor Core Neutronics. The epithermal neutron energy profile (a) There is a slight offset (in energy) due to the high energy fission neutrons generated in the emitter. The spatial profiles for both thermal (c) and fast (d) neutrons indicate a typical Bessel-like spatial profile in the radial coordinate (b).

The energy spectrum was found for both the emitter and collector of the centerline fuel element; it is essentially thermal for both collector and emitter, peaking at a temperature of 0.05eV. To obtain a visual spatial profile for both thermal and fast neutrons, we used the meshtal

feature, which overlays a mesh on the geometry and calculates the track length estimate of a particle flux, averaged over the mesh cell. Numerically, we determined the spatial neutron flux profile to be Bessel-like (as expected) by tallying the total fission heating of all the fuel elements, plotting the relative fission rates (to the maximum fission rate at the center) across the radial coordinate, then fitting a zero order Bessel function of the form $J_0(\frac{2.405r}{\tilde{R}})$ to these points, where r is the radial distance from center and $\tilde{R}$ is the extrapolated radius for a reflected core. $\tilde{R}$ was found to be 35 cm ($R = 30$ cm).

To verify the reactor's ability to be taken critical and subcritical and total reactivity insertion by the control drums, criticality (k_{eff}) tests were performed under the following conditions: where the $^{10}BC_4$ inserts were all rotated to face inward toward the core at room temperature (i.e. cold shutdown) and at operating temperatures (e.g. emergency shutdown or hot standby); outward from the core at operating temperatures. For the former shutdown scenarios, $k_{eff} = 0.99229\pm0.00009$ for the fuel and moderator at room temperature ($T_{fuel} = T_{mod} = 300K$) and $k_{eff} = 1.03019\pm0.00019$ at operating temperatures $T_{fuel} = 1900K$ and $T_{mod} = 1000K$; $k_{eff} = 1.04656\pm0.00019$ for control drums all rotated outward at $T_{fuel} = 1900K$ and $T_{mod} = 1000K$. Thus, the reactor may insert 5399 – 5455pcm from cold shut down conditions to operational temperature conditions and 1599 – 1675pcm while maintaining operation temperature conditions. Though this would not be enough to restart the reactor immediately after in the event of an unexpected shutdown casualty, it still demonstrates the reactor ability to be taken critical and subcritical. Future design iterations should explore other means of reactivity control (i.e. control rods rods).

5.4 Results: Reactor Power Output Calculation

To calculate reactor power output, we use the methods outlined in sections 4.4.1 and 4.5.1, beginning with the following assumptions:

1. A radially constant temperature profile amongst fuel elements. As temperature varies widely with heat removal methods, use of central fuel voids, enrichment, etc. we leave such design assessments to future work which will make use of more advanced thermal modeling methods beyond the scope of this thesis.
2. An axial emitter temperature (T_E) profile for all fuel elements according to Figure 5.3 adapted from [51]. This temperature profile is used to calculate local ϕ_E and I_{th} values.
3. A constant P_{aux} for fuel elements and constant coupling efficiency of 80%. Coupling methods and corresponding efficiencies of P_{aux} will have a wide range of implementation, e.g. capacitively (CCP) or inductively (ICP) coupled Radio Frequency (RF), Microwave, Electron Cyclotron Resonance (ECR), etc.) depending on the application. The chosen 80% efficiency is relatively a conservative: [65] reports an ICP source coupling efficiency of 97% for an argon plasma at 1 torr with $P_{aux} \approx 1$ W cm^{-3} and this efficiency tends to increase with increasing power input.
4. The axial power distribution behaves as a typical reflected core, where $P_{fuel} \propto P_{abs} \propto P_i \cos\frac{\pi z}{\tilde{H}}$ where $\tilde{H}$ is the extrapolated height (cm) and P_i is the power density of the ith fuel element for $z = 0$ (W cm^{-3}), and z is the axial coordinate (cm) where $-\tilde{H}/2 \leq z \leq \tilde{H}/2$.

5. The system mass of HITEC scales proportionally to TOPAZ-II. That is, the ratio of the reactor core mass to the system mass is constant. This assumption is made to give an intentionally conservative specific power estimate. Namely, the reactor shielding does not scale linearly with reactor core size.

Beginning with the first part of the HITEC model, which calculates fission fragment power deposition into the gas (P_{abs}), we must know the fission rate near the surface of the fuel element. As this value changes throughout the reactor core, it is easiest to proceed by assuming some maximum fission heating rate ($P_{fuel,max}$) in a particular fuel element, then scale the other fuel element heating rates (both volumetric and surface) to this maximum value. In MCNP, this is accomplished by using the fission heating tally F7 for two distinct zones in each fuel element: the "bulk" which encompasses the all the UO$_2$ and the "surface" which is the remaining 50 μm of UO$_2$-W. For this particular reactor, the assigned $P_{fuel,max} = 750$ W cm^{-3}. Thus, a corresponding $P_{abs,max}$ may be calculated by taking the ratio of the relative fission rates given by the F7 tally. These calculations are represented in Figure 5.4. The surface-to-bulk fission rate ratios do not vary more than 2%; to simplify the calculation, we assume a constant surface-to-bulk fission rate ratio of 3.65. The increased number of fuel elements for decreased values of relative fission heating is representative of a radially decreasing power profile (Bessel-like as in figure 5.3b), where the number of fuel elements in radial groups increases for increasing radius.
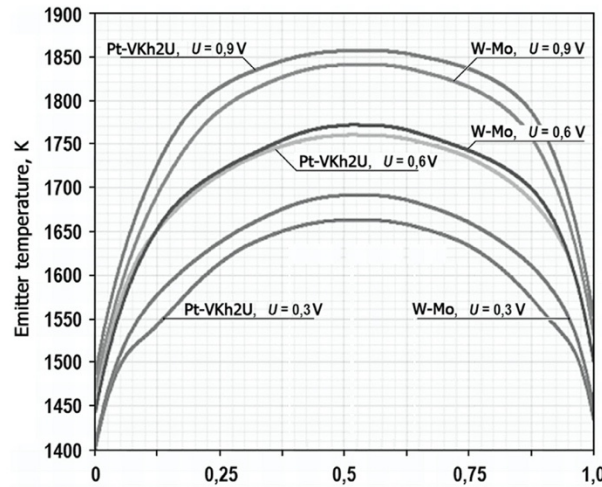
Figure 5.3. Thermionic fuel element temperature profile adapted [51]. For the reactor under consideration, we scale the top curve to a peak temperature of 1900K.

To determine the axial power distribution, we must know $\widetilde{H}$; then we may scale according to assumption 4. $\widetilde{H}$ is found by tallying the relative neutron flux via point detectors, or the F5 tally, placed at the center of the core and at the top of core (since the core composition is homogeneous in the axial coordinate). We found the relative flux at the top to be attenuated to 43% of maximum of that at the center. Thus, from assumption 4, $\widetilde{H} = \frac{50\pi}{\cos^{-1}(0.43)} = 139.5$ cm and is assumed constant throughout the core's radial profile.

Now, with a complete spatial profile for P_{fuel}, correlation between P_{fuel} and P_{abs}, and temperature profile assumptions, we may adequately model the core's heat production, plasma ionization and electrical output. We begin by running the charged particle stopping portion of the

HITEC model for $P_{abs,max}$ (in the coaxial configuration). Next, the plasma model calculates a P_{abs} vs. T_e curve for the gas composition and temperature given. With this curve, $P_{abs,max}$ and all other relative axial P_{abs} values of a single fuel element are iterated through to determine the spatially dependent T_e and n_e. To make a single fuel element power output calculation, each set of local T_e and n_e values is combined with the local I_{th} (determined by T_E and ϕ_e.), then P_{out} is found via methods of 4.4.1. This process is repeated for the other fuel elements in a straightforward manner in order to obtain the total P_{out}, P_{th} and $\eta_T = \frac{P_{out}}{P_{th}}$ of the reactor.

We consider four distinct cases for the HITEC reactor design under consideration which highlight the effects of implementing an increased collector – emitter surface area ratio, A and auxiliary power, P_{aux}:

1. Where $P_{aux} = 0$ W cm^{-3} and $A = 2$: plasma ionization occurs by charged particle energy deposition via unclad emitter only and only the collector surface immediately facing the emitter is considered for electrical power output.
2. Where $P_{aux} = 0$ W cm^{-3} and $A = 6$: plasma ionization occurs by charged particle energy deposition via unclad emitter. The increased surface area of the collector is made possible by advanced surfacing techniques, e.g. plasma or chemical etching.
3. Where $P_{aux} = 75$ W cm^{-3} and $A = 20$: plasma ionization at emitter occurs by charged particle energy deposition via unclad emitter; ionization at the collector is provided by an auxiliary power source. This allows for increased n_e and T_e at the collector surface.
4. Where $P_{aux} = 75$ W cm^{-3} and $A = 60$: plasma ionization at emitter occurs by charged particle energy deposition via unclad emitter; ionization at the collector is provided by an auxiliary power source. The increased surface area of the collector is made possible by advanced surfacing techniques, e.g. plasma or chemical etching. In combination, both auxiliary power and advanced surfacing techniques allow for increased n_e, A_C, and T_e at the collector surface.

a) b)
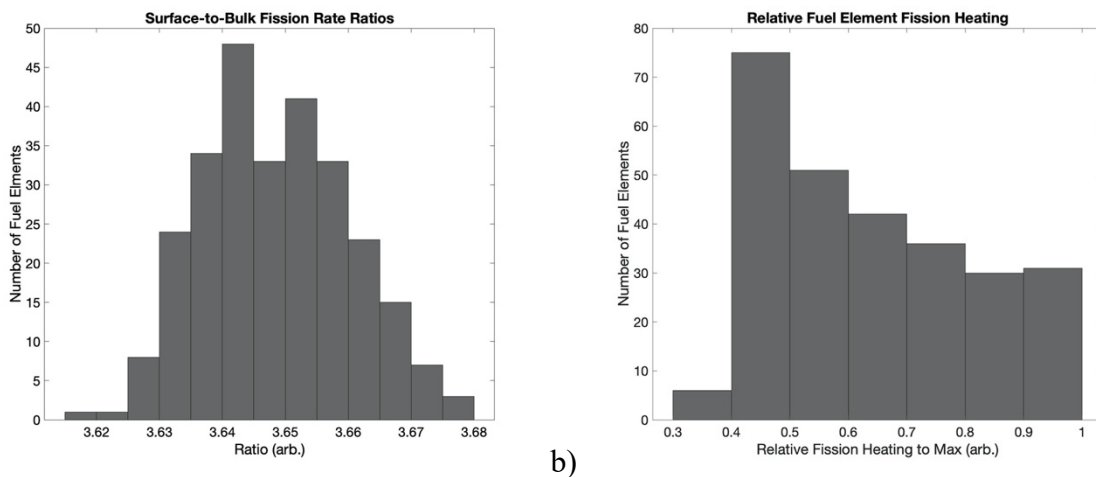
Figure 5.4. Fuel element distribution of a) relative surface to bulk fission rate ratios and b) fuel element fission heating.

Cases 1 and 2 represent operational modes where auxiliary power has either not been engineered into the system (first generation HITEC reactors) or is currently offline due to some type of casualty circumstance. Cases 3 and 4 represent a HITEC based reactor with auxiliary power performing at full power. Here, we calculate P_{aux} by inserting equation 2.18 into 2.19, then solve for T_e. Choosing $P_{aux} = 75$ W cm^{-3} (arbitrarily), we then insert the corresponding T_e back into equation 2.18 and obtain n_e. We note another possible scenario not mentioned previously where the collector may be coated with thin layers (<50 μm) of neutron reactive material (e.g. ^{242m}Am^{10}B$_6$ or others) so that additional plasma ionization is achieved through charged particle energy deposition via the collector. In general, these plasmas will be of similar temperature and density to that of the emitter and we see efficiency gains of factors of 3 or more ($\eta_T > 0.3$) for $A > 20$. This scenario is not formally included in the reactor analysis since the addition of neutron reactive materials into the core would change the reactor core's neutronics. Given a complex collector geometry such as the one in Figure 5.2b, we leave this potentially tedious modelling to work to a future study. Table 5.6 summarizes the main design parameters and performance metrics of the HITEC reactor.

For cases 1 and 2, where only charged particle deposition from the unclad emitter is used for plasma ionization, the HITEC reactor achieves an 11 – 18% thermal efficiency: a factor of 2 to 3 greater than TOPAZ – II. This performance is close to traditional TECs in the laboratory setting. More notably, the emitter-collector gap distance in HITEC is 2mm compared to the < 0.5mm gap in traditional laboratory devices, where irradiation swelling is not a factor. The combined performance gain and relaxed gap distance constraint offered by charged particle ionization alone highlights the inherent advantage of the HITEC energy conversion scheme as compared to traditional thermionics.

Cases 3 and 4 show the potential benefits of implementing auxiliary power into collector plasma ionization, which is an example of adding non-thermal energy into the system. It should not be surprising to the reader that, at sufficient n_e, T_e, and A_C at the collector surface, greater than 100% thermal efficiency is attainable – this concept was discussed in section 3.3.5. Analogous to break-even fusion reactors, where the power harnessed from fusion plasmas must exceed the power input to maintain their plasmas, the electrical power harnessed from HITEC must exceed the input power into sustaining the collector plasma. For instance, if $P_{aux} = 75$ W cm^{-3} and $A = 2$ in the reactor under consideration, the total auxiliary power, ~ 2 MW$_e$ would exceed the total power output of the reactor, which is only ~ 1MW$_e$. Thus, break-even conditions for HITEC reactor plasmas with auxiliary power are not only a function of P_{aux} but also A and I_{th}. Of course, it would be narrowminded to consider auxiliary power only to envisage a HITEC reactor's increased thermal efficiency at steady state; it has not escaped our notice that this power may potentially be pumped into the reactor core plasma in a pulsed fashion to generate both coherent and incoherent electromagnetic wave phenomena. However, further analysis into this subject would be beyond the scope of this thesis and the student's security clearance but should be considered in future work.

In all cases, the HITEC reactor shows marked performance improvement and loosened design constraints to its traditional TEC predecessor, TOPAZ-II. Not only does this demonstrate the reactor design's feasibility and capability as a power producing nuclear reactor, but also solidifies its applicability to high powered missions in space. Referring back to the NASA technology roadmaps (summarized in Chapter 1), which demand > 60 W$_e$/kg for output power in the 1-10MW$_e$ range and > 200 W$_e$/kg for output power > 10MW$_e$, the HITEC reactor's conservatively estimated specific power output may well exceed NASA's specific power

guidelines for both power output ranges. Thus, HITEC reactors offer an undeniably attractive static energy conversion alternative to the favored dynamic Brayton cycle for nuclear reactors that produce electrical power in excess of 1MW$_e$.

Table 5.6 Comparison of HITEC reactor design features to TOPAZ-II. For HITEC, four separate performance cases are assessed in comparison to TOPAZ-II.

	HITEC	TOPAZ - II
Core:		
Moderator	ZrH$_{1.85}$	ZrH$_{1.85}$
Radial Reflector/Diameter/Height (cm)	Be/100/100	Be/40.8/48
Axial Reflector/Diameter/Height (cm)	Be/100/10	Be/26/5.5
Reactivity Control	12 Be drums with ^{10}B$_4$C inserts	12 Be drums with ^{10}B$_4$C inserts
Height (cm)	120	
Reactor Diameter (cm)	60	26
Fuel loading (kg)	66	27
Fuel Enrichment	20%, 90% at emitter surface	96%
Reactor Mass (kg)	2560	290
Neutron Spectrum	Thermal	Thermal
Fuel elements	271 TFE	37 TFE
Emitter:		
Active Length	100cm	37.5
Material	U(90)O$_2$-W CERMET	Monocrystal Mo with 3% Nb
Coating	none	^{184}W
Inner Diameter (mm)	5.9	19.5
Outer Diameter	6	21
Collector:		
Material	Zr	Monocrystal Mo
Coating	Mo	none
Inner Diameter (mm)	10	23.5
Outer Diameter (mm)	19	25
Gap Width (mm)	2	0.6
System:		

P_{aux} (W cm^{-3})	A (unitless)								0	1
		0	2	0	6	75	20	75	60	0	1

	HITEC				TOPAZ - II
Electrical Power (MW$_e$)	0.26	0.43	1.98	3.26	0.004 – 0.006
Thermal Power	2.35	2.35	2.35	2.35	0.115 – 0.135
Thermal Efficiency (%)	.11	0.18	.84	1.39	~0.04 – 0.06
Specific Power (no PMAD) (W$_e$/kg)	28	72	211	348	5
Mass factor	3.66				3.66
Cs Reservoir Temperature (K)	600				580
T_E(max), T_C (K)	1900, 800				1875, 850

5.5 Conclusions and Future Work

In this work, we have successfully developed an electrical power model, from first principles, that accurately calculates the electrical performance of TEC devices whose interelectrode gap plasmas are ionized via charged particles – from both fission fragments and their subsequent beta decay. We tested the HITEC model by simulating conditions of experiments [52] and [14]: the only existing experimental data for such a device. Through comparing our HITEC model to this data, we revealed that the most important parameters affecting device power output curves (P-V curves) are the emitter and collector work functions (ϕ_E and ϕ_C). In the case of thermionic emission, the peak output power varies slightly less than linearly with thermionic emission; a similar trend is seen when varying ϕ_C, but its variance also broadens the P-V curve. This broadening is due to a direct shift of the I-V characteristic by some $\Delta\phi$ which translates into both a larger peak power output and wider voltage range in the power producing quadrant. Notable is that although thermionic emission is very sensitive to both ϕ_E ($\propto \exp(-\phi_E)$) and T_E ($\propto T_E^2 \exp(-1/T_E)$) T_E is more readily measured and controlled under reactor conditions than ϕ_E which is physically more complex. Similar arguments can be made for ϕ_C.

To our surprise, a single species recombination plasma model is sufficient to reflect penning gas plasma parameters under reactor conditions. We believe this is due to, in part, the significantly reduced dissociative recombination experienced by ions at higher temperatures. It is interesting to compare the theoretical k_{dr} values of Ar_2^+ to that of cesium seeded atmospheric argon plasmas in thermal equilibrium ($T_a = T_e$) [66]. [65] finds recombination values of roughly 1 x 10^{-8} cm^3 s^{-1} in the 1500-2500K temperature range. From [32], $k_{dr,Ar_2^+}(T_a, T_e) = 3$ x 10^{-8} cm^3 s^{-1} for T_a =2000K and $T_e = 3500$K. Even though these values differ by a factor of three, this leads to a difference in calculated n_e by less than a factor of two. And, as is evident in Figure 5.2d, the P-V (especially the peak power value) not strongly affected by the plasma conditions at the emitter.

We used the HITEC model to predict the electrical power output of a power producing nuclear reactor based on this energy conversion scheme. Modeling four cases for a specific core design (similar in configuration to TOPAZ – II) we found that in three of the four instances, the HITEC reactor exceeded NASA's specific power limits for the 1-10 MW$_e$ power output range (> 60W$_e$). In two cases, where auxiliary power was implemented for additional collector plasma ionization, NASA's specific power limit for reactor power outputs in excess of 10MW$_e$ (>200 W$_e$/kg) was exceeded: for the 2.5MW$_{th}$ reactor under consideration, the maximum specific power attained was 348 W$_e$/kg. Thus, this design study demonstrates HITEC reactors' undeniable potential for high power space mission applications. Furthermore, this reactor design offers an attractive static energy conversion alternative to the lone dynamic energy conversion Brayton cycle, currently the only energy conversion method that has an active funding stream for space nuclear power in excess of 1MW$_e$.

To realistically validate the HITEC model on any in-core system, one must have a body of pertinent experimental data. Currently, the only body of such data draws from [14] which consisted of a single fuel type and penning gas. In order to validate and refine theoretical models further to encompass other fuel types and gases, we recommend experimental research avenues in the following areas:

77

1. ϕ_E and ϕ_C measurements of unclad nuclear fuel elements (emitter) and collector materials in-core. This will quantify contact potential, $\Delta\phi$ and emission current I_{th} under irradiated environments.
2. High energy Compton and Photelectric electron production by reactor generated gamma photons in fuel cell system.
3. Low energy Auger electron emission (from fuel element) from fission fragment decay near the surface of fueled element.
4. β^- energy deposition at low energy (<10keV) at the solid-gaseous boundary where the continuous-slowing-down-approximation (CSDA) assumption fails. This is where the energy deposition of electrons is the greatest.
5. Simultaneous determination of plasma parameters (n_e, T_e) for both noble gases and penning gases at high gas temperatures $(T_a > 500K)$ where electrons are not in thermal equilibrium with the gas.
6. Auxiliary power plasma coupling methods under reactor conditions, e.g. RF (capacitive and inductive), Microwave, ECR etc. at low power density ($P_{aux} < 100$ W cm^{-3}) for CW operation and high power density ($P_{aux} > 100$ W cm^{-3}) for pulsed operation.

Little experimental data exists for these basic phenomena – even for out-of-core conditions. Research avenues 1-3 may be categorized as purely basic nuclear data and materials science, 4 falls under both nuclear data and plasma science, and 5-6 specifically pertain to low temperature plasma science. Gaining more experimental and technical basis in these core areas would not only improve our understanding of HITEC based systems, but also broaden and deepen our fundamental understanding of nuclear and low temperature plasma phenomena, both separately and in concert. This insight would undoubtedly spark further research avenues and give rise to new technology sets that benefit mankind.

The HITEC model is a multiphysics modeling code that couples charged particle energy deposition, neutronics, and low temperature plasma physics to simulate electrical performance in nuclear devices at assumed temperatures T_a, T_E, and T_C. The goal of this dissertation work was to validate the physics *coupling* between the individual physics "packages" which we have done to a high degree of confidence. Then, this code's global level of accuracy is limited only by the local accuracy of its individual constituents. Therefore, future work in theory and simulation should be carried out mainly on the *individual* level: i.e. in charged particle transport, neutronics, and low temperature plasma physics. Furthermore, we note that future iterations of the HITEC modeling paradigm should include heat transfer so that more accurate spatial temperature profiles (T_a, T_E, and T_C) are incorporated. Luckily, all these areas in theory and simulation have existing funding streams and therefore do not require additional funding. Thus, to further HITEC modeling capabilities, we suggest a team (or individual) begin integrating the results of these efforts into an available multiphyics framework such as the open source Multiphysics Object Oriented Simulation Environment package (MOOSE) [67].

The cross-pollination of nuclear and plasma science at low density ($\sim 10^{-4} - 10^0$ g cm^{-3}) and temperature (below 1 keV or 10^7 K) up to present has been minimal. Besides a brief research effort in nuclear pumped lasers motivated by the strategic defense initiative that ended in the early 1990s, research avenues in density and temperature regimes less than 10^1 g cm^{-3} and 100 eV respectively are just beginning to gain visibility [68, 69]. Essentially, fusion plasmas for energy and nuclear weapons-based applications have been the only thriving amalgamations of nuclear and plasma physics: they consider these phenomena at relatively high pressures and

temperatures in excess of 10^0 g cm^{-3} and 10^1 eV, known as warm dense matter (WDM) and greater than 10^2 g cm^{-3} and 10^2 eV – high energy density physics regimes (HEDP). Though both these technical applications are vital to energy and national security, they both already have numerous theoretical and experimental facilities for their continued investigation, e.g. NIF, Z-Machine, D-III-D, etc.

Fission based plasmas have not gained the same level of interest (or even visibility) as their fusion counterparts in either the nuclear or plasma physics communities. Yet, these low density and temperature plasmas may offer crucial application to technical challenges humanity faces in the near future; this thesis highlights just one of those applications. Only through continued interest and investigation into nuclear excited, low temperature plasmas will we be able to uncover more uses. Given HITEC and its immediate utility to efficient and compact space/remote nuclear power, we hope this thesis provokes more discussion and general interest amongst the nuclear and plasma physics communities.

Appendix

The following appendices comprise the codes used to analyze the experimental data from the "GM Study" and model power characteristics for nuclear reactor scale devices. The fission fragment and beta particle stopping models, which outputs P_{abs}, P_{th}, and f^+ for a given set of material properties, is offered in both C++ (Appendix A) for faster runtimes and in MATLAB (Appendix B) for full power model calculations. Future generations of the code will likely be written fully in C++.

A: Fission Fragment Stopping Model: C++

```cpp
#include <iostream>
#include <fstream>
#include <vector>
#include <string>
#include <cmath>
#include <cstdlib>
#include <stdio.h>
#include <stdlib.h>
#include <ctime>
using std::cerr;
using std::cout;
using std::endl;
using std::ifstream;

//Define constants
//Physical constants
double me = 9.11e-31; //kg
double mne = 3.35e-26;//kg
double mar = 6.63e-26;//kg
double mkr = 1.39e-25;//kg
double mxe = 2.18e-25;//kg
double c = 299792458; //m s^-1
double hbar = 1.0545718e-34;// J s
double Vo = 2.188275e6; // m*s^-1
double ao = 0.529e-10; //m, Bohr radius
double kboltz = 1.380648e-23; //m^2 kg s^-2 K^-1
```

```cpp
double eV = 1.602e-19; //J
double eps = 8.85e-12; //permittivity
double nav = 6.022e23; //Avogadro's #
double pi = 3.1415926; //Pi
//Stopping power variables
double density; //g*cm^-3
double Z; //atomic number of heaviest component in fuel or gas
double A; //atomic mass of heaviest component in fuel or gas
double r = 3; //mm inner radius (emitter)
double R = 5; //mm outer radius (collector)
double rhoel; //m^-3
double Vf; //m*s^-1
double massisotope; //atomic mass of ff
double Zff; //atomic number of ff
double Eff; // energy of ff (MeV)
//Energy deposition variables. Some of these variables are defined in the
program (near the bottom).
double E_abs; // energy absorbed in gas (MeV)
int total_particles; //total number of particles that make it into the gas
int particles_per_layer = 10000; //number of events
int total_layers = 30; //number of layers. particles_per_layer = 10000 and
total_layers = 30 yields a run time of about 10 seconds.
double delta = 0.25*1e-3; //width of layer.

int main(){
//time_req = clock();

srand (time(NULL));

double pressure; //torr
int T_emitter; //K
int T_collector; //K

std::cout << "\nEnter Pressure: \n";
std::cin >> pressure;

double ratio = pressure / 760;
/*
std::cout << "\nEnter Emitter Temperature: \n";
std::cin >> T_emitter;

std::cout << "\nEnter Collector Temperature: \n";
std::cin >> T_collector;*/

//First, we sample a random fission fragment of mass massisotope, Energy Eff,
and charg Zff.
//With these values, we calculate the fission fragment's range in a material.

//Import FREYA and (SRIM) hydrogen stopping data into vectors. ALL SRIM DATA
SHOULD BE IN UNITS OF MeV (energy) and MeV/mm (stopping power)
   ifstream indata1;
   ifstream indata2;
   ifstream indata3;
   double num1;
   double num2;
   double num3;
   std::vector<double> x;
   std::vector<double> y;
```

```cpp
    std::vector<double> z;
    std::vector<double> Edepbg_total;
    std::vector<double> Edepig_total;
    std::vector<double> Edepag_total;
    std::vector<double> makes_it_total;



indata1.open("events100k"); // opens the file
    if(!indata1) { // file couldn't be opened

        cerr << "Error: file could not be opened" << endl;
        exit(1);


    }
indata1 >> num1;
    while ( !indata1.eof() ) { // keep reading until end-of-file

            x.push_back(num1);
        indata1 >> num1; // sets EOF flag if no value found


    }

    indata1.close();
    std::cout << "End-of-file reached.." << endl;

indata2.open("HinU"); // opens the file
    if(!indata2) { // file couldn't be opened

        cerr << "Error: file could not be opened" << endl;
        exit(1);


    }
indata2 >> num2;
    while ( !indata2.eof() ) { // keep reading until end-of-file

            y.push_back(num2);
        indata2 >> num2; // sets EOF flag if no value found


    }

    indata2.close();
    std::cout << "End-of-file reached.." << endl;

indata3.open("HinAr"); // opens the file
    if(!indata3) { // file couldn't be opened

        cerr << "Error: file could not be opened" << endl;
        exit(1);


    }
indata3 >> num3;
    while ( !indata3.eof() ) { // keep reading until end-of-file

            z.push_back(num3);
        indata3 >> num3; // sets EOF flag if no value found


    }
```

```
    indata3.close();
    std::cout << "End-of-file reached.." << endl;

double lightZ[100000] = { };
double lightA[100000] = { };
double lightE[100000] = { };
double heavyZ[100000] = { };
double heavyA[100000] = { };
double heavyE[100000] = { };

//Writes vector information into separate arrays for light/heavy ff (Z, A,
KE).
for(int i = 0; i < x.size() / 20; i++){

        lightZ[i] = x[i*20 + 1];
        lightA[i] = x[i*20 + 2];
        lightE[i] = x[i*20 + 6];
        heavyZ[i] = x[i*20 + 11];
        heavyA[i] = x[i*20 + 12];
        heavyE[i] = x[i*20 + 16];

}
double HinUE[70] = { }; // MeV
double HinUdEdx[70] = { };// MeV/mm

   for(int i = 0; i < y.size() / 2; i++){

        HinUE[i] = y[i*2];
        HinUdEdx[i] = y[i*2 + 1];

}
double HinArE[70] = { }; // MeV
double HinArdEdx[70] = { }; // MeV/mm

   for(int i = 0; i < z.size() / 2; i++){

        HinArE[i] = z[i*2];
        HinArdEdx[i] = z[i*2 + 1];

}

for(int k = 0; k < total_layers; k++){

int makes_it = 0; //number of particles in the layer that make it to the gas
int stops_before_gas = 0; // '' stop before the gas
int stops_in_gas = 0; // '' stop before the gas. Usually not useful
int stops_after_gas = 0; // '' stop before the gas. Useful to calculate
additional heat dissipated by the other electrode
double Edepbg = 0; //energy equivalent of stops_before_gas
double Edepig = 0; // '' stops_in_gas
double Edepag = 0; // '' stops_after_gas

for(int j = 0; j < particles_per_layer; j++){

 int index = rand() % 100000;
 int lh = rand() % 2 + 1; //decides if the emitted fragment is light or heavy
//pick random Zff, Eff, energy from FREYA for fissioning material
```

```
 if(lh == 1){

 massisotope = lightA[index] ;
 Zff = lightZ[index];
 Eff = lightE[index];

 }

 else{

 massisotope = heavyA[index] ;
 Zff = heavyZ[index];
 Eff = heavyE[index];

 }

       double energy[70] = { }; // 70 = number of elements from SRIM files.
 Since these are arrays, the number of elements is fixed.
     for(int i = 0; i < 70; i++){

       energy[i] = HinUE[i]*massisotope; //scales the hydrogen energy to the
 fission fragment MeV/amu.

     }

       double ereduced[70];
     double stoppingnuclearU[70] = { };
     double stoppingelectronicU[70] = { };
     double stoppingnuclearAr[70] = { };
     double stoppingelectronicAr[70] = { };
     double yr[70] = { };
     double range[70] = { };
     double a = ao/sqrt(pow(Zff,0.6667)+pow(Z,0.6667)); //Lindhard screening
 function
     double mu = A/massisotope; //reduced mass

   //Calculate nuclear and electronic stopping in solid
   //Material properties:
    density = 10.22; //g*cm^-3
    Z = 92;
    A = 235;
    rhoel = Z/A*nav*density*1e6; //m^-3
    Vf = (hbar/me)*pow((3*pow(pi,2)*rhoel),0.3333); //m*s^-1

     double Vrel; //relative valocity between the ff and conduction electron of
 the material, assuming conduction electrons are a "free electron gas."
     double beta[70] = { };
     double alpha[70] = { };
     double V1[70] = { };
     double Cf;

   //Nuclear
     for(int i = 69; i >= 0; i--){

       Vf = (hbar/me)*pow((3*pow(pi,2)*rhoel),0.3333); //m*s^-1
       V1[i] = c*sqrt(2*energy[i]/(931.5*massisotope)); //m*s^-1
```

```
        if(V1[i] >= Vf){

               Vrel = V1[i]*(1+pow(Vf,2)/(5*pow(V1[i],2)));

        }

        else{

               Vrel = 3*Vf/4*(1+2*pow(V1[i],2)/(3*pow(Vf,2))-
(1/15*pow(V1[i]/Vf,4)));

        }

        ereduced[i] =
32.53*A*energy[i]*1e3/(Z*Zff*(A+massisotope)*(pow(Zff,0.23)+pow(Z,0.23)));

        if(ereduced[i] <= 30){

               stoppingnuclearU[i] = rhoel/Z*1e-13*(8.462*1e-
15*Zff*Z*massisotope/((massisotope+A)*(pow(Zff,0.23)+pow(Z,0.23))))*log(1+1.1
383*ereduced[i])/(2*(ereduced[i]+0.01321*pow(ereduced[i],0.21226)+0.19593*pow
(ereduced[i],0.5)));

        }

        else{
               stoppingnuclearU[i] = rhoel/Z*1e-13*(8.462*1e-
15*Zff*Z*massisotope/((massisotope+A)*(pow(Zff,0.23)+pow(Z,0.23))))*log(eredu
ced[i])/(2*ereduced[i]);

        }

 //Electronic
        yr[i] = Vrel/(Vo*pow(Zff,0.6667));

        if (yr[i] < 0.13) {

                 stoppingelectronicU[i] =
stoppingelectronicU[i+1]*sqrt(energy[i]/energy[i+1]);

        }
        else {

        beta[i] = 0.886 * sqrt(energy[i] * 1e3 / (25 * massisotope)) /
pow(Zff,0.6667);
        alpha[i] = beta[i] + 0.0378 * sin(pi * beta[i] / 2);
        Cf = 1.13; //1 for Gases, 1.13 for U
        stoppingelectronicU[i] = HinUdEdx[i] * pow(Cf*Zff,2) * pow((1 - exp(-
alpha[i])*(1.034-0.1777*exp(-0.8114*Zff))),2);
        //std::cout << energy[i] << " "<< ereduced[i] << " " <<
stoppingelectronicU[i] << " " << stoppingnuclearU[i] << "\n";
        }
        }

    for(int i = 0; i < 70; i++){

        range[0] = 0;
```

```cpp
        range[i+1] = range[i] + (energy[i+1]-
energy[i])/(stoppingnuclearU[i]+stoppingelectronicU[i]) * (1-
mu*stoppingnuclearU[i]*range[i]/(2*energy[i]));
            //std::cout << energy[i] << " " <<range[i]  << "\n";
            }
//Match the projectile's initial energy with the corresponding energy index
double ediff[70] = { };
int min_index = 0;

    for(int i = 0; i < 70; i++){

      ediff[i] = abs(Eff-energy[i]);
      //std::cout << energy[i] << " " << ediff[i] << "\n";
    }

    for(int i = 0; i < 70; i++){

      if(ediff[i+1] < ediff[i]){

            min_index++;

      }
    }
    //std::cout << range[min_index] << "\n";
    //std::cout << min_index <<  "  " << energy[min_index]<<  "    " <<
ediff[min_index] << "\n";

double d = (k+((double) rand()/RAND_MAX)) * delta; //choses a particle
distance within the layer
double phi = ((double) rand()/RAND_MAX) * pi / 2; //random angle between 0
and pi/2, phi.
double theta = ((double) rand()/RAND_MAX) * pi / 2; //random angle between 0
and pi/2, theta. should be between 0 and pi for electrons
//double l = 1/sin(phi)*((d-r) * cos(theta) + sqrt(0.5 * (r * (r + 2 * d) -
pow(d,2) + pow(d - r, 2) * cos(2 * theta)))); //use for electrons
double l = d/cos(phi); //for fission fragments using infinite plane
approximation.
double Enew; // new energy of ff when it makes it to the surface of the fuel.

if(l <= range[min_index] && l >= 0){

        Enew = Eff*pow(1-l/range[min_index],2);
        makes_it++;

//repeat process for gas. Z, A, and rhoel change, the rest stays constant.
This should just be turned into a function later on; probably of Z and A.

Z = 18;
A = 40;
density = 0.00178 * ratio;
rhoel = Z/A*nav*density*1e6;

//rewrite energy vector for gas data.
for(int i = 0; i < 70; i++){

    energy[i] = HinArE[i]*massisotope;

    }
```

85

```
//Nuclear
    for(int i = 69; i >= 0; i--){

      Vf = (hbar/me)*pow((3*pow(pi,2)*rhoel),0.3333); //m*s^-1
      V1[i] = c*sqrt(2*energy[i]/(931.5*massisotope)); //m*s^-1

        if(V1[i] >= Vf){

            Vrel = V1[i]*(1+pow(Vf,2)/(5*pow(V1[i],2)));

        }

        else{

            Vrel = 3*Vf/4*(1+2*pow(V1[i],2)/(3*pow(Vf,2))-
(1/15*pow(V1[i]/Vf,4)));

        }

        ereduced[i] =
32.53*A*energy[i]*1e3/(Z*Zff*(A+massisotope)*(pow(Zff,0.23)+pow(Z,0.23)));

        if(ereduced[i] <= 30){

            stoppingnuclearAr[i] = rhoel/Z*1e-13*(8.462*1e-
15*Zff*Z*massisotope/((massisotope+A)*(pow(Zff,0.23)+pow(Z,0.23))))*log(1+1.1
383*ereduced[i])/(2*(ereduced[i]+0.01321*pow(ereduced[i],0.21226)+0.19593*pow
(ereduced[i],0.5)));

        }

        else{

            stoppingnuclearAr[i] = rhoel/Z*1e-13*(8.462*1e-
15*Zff*Z*massisotope/((massisotope+A)*(pow(Zff,0.23)+pow(Z,0.23))))*log(eredu
ced[i])/(2*ereduced[i]);

        }

 //Electronic
        yr[i] = Vrel/(Vo*pow(Zff,0.6667));

        if (yr[i] < 0.13) {

                stoppingelectronicAr[i] =
stoppingelectronicU[i+1]*sqrt(energy[i]/energy[i+1]);

        }

        else {

        beta[i] = 0.886 * sqrt(energy[i] * 1e3 / (25 * massisotope)) /
pow(Zff,0.6667);
        alpha[i] = beta[i] + 0.0378 * sin(pi * beta[i] / 2);
        Cf = 1.0; //1 for Gases, 1.13 for U
        stoppingelectronicAr[i] = HinArdEdx[i] * pow(Cf*Zff,2) * pow((1 -
exp(-alpha[i])*(1.034-0.1777*exp(-0.8114*Zff))),2);
```

```cpp
            //std::cout << energy[i] << " "<< ereduced[i] << " " <<
stoppingelectronicAr[i] << " " << stoppingnuclearAr[i] << "\n";
            }
            }

    for(int i = 0; i < 70; i++){

        range[0] = 0;
          range[i+1] = range[i] + (energy[i+1]-
energy[i])/(stoppingnuclearAr[i]+stoppingelectronicAr[i]) * (1-
mu*stoppingnuclearAr[i]*range[i]/(2*energy[i]));
            //std::cout << energy[i] << " " << range[i]  << "\n";
            }

    min_index = 0;

    for(int i = 0; i < 70; i++){

      ediff[i] = abs(Eff-energy[i]);
      //std::cout << energy[i] << " " << ediff[i] << "\n";
    }

    for(int i = 0; i < 70; i++){

      if(ediff[i+1] < ediff[i]){
            min_index++;

      }
    }

            double D = R - r; //gap distance between emitter and collector.
            double L = 1/sin(phi)*((D-R) * cos(theta) + sqrt(0.5 * (R * (R +
2 * D) - pow(D,2) + pow(D - R, 2) * cos(2 * theta))));

        if(L > range[min_index]){ //means particle will fully deposit in gas

            Edepbg += Eff - Enew;
            Edepig += Enew;
            stops_in_gas++;

        }
        else{

                Edepbg += Eff - Enew;
            Edepig += Enew*(1-pow((1-L/range[min_index]),2));
            Edepag += Enew*(pow((1-L/range[min_index]),2));
            stops_after_gas++;

        }
    }
            else{

        Edepbg += Eff;
        stops_before_gas++;


        }
```

```
}
            Edepbg_total.push_back(Edepbg);
            Edepig_total.push_back(Edepig);
            Edepag_total.push_back(Edepag);
            makes_it_total.push_back(makes_it);
//std::cout << Edepbg << "      " << Edepig << "   " << Edepag << "   " <<
makes_it << "\n";
}

int dummy; //keeps track of layers that don't contribute to plasma ionization

for(int i = 0; i < Edepig_total.size(); i++){

      E_abs += Edepig_total[i];
      total_particles += makes_it_total[i];

      if(Edepig_total[i] == 0){

            dummy++;

      }

      std::cout << E_abs << "    " << Edepig_total[i] << "    " <<
total_particles << "    " << makes_it_total[i] << "\n";
}
//Output Parameters, P_th and Pabs_max. The latter may be scaled by specific
reactor spatial profiles obtained via netronics codes.
double G = (total_layers - dummy) * delta * 2 * r/ (pow(R,2) - pow(r,2));
double reaction_rate = 2.5e13;
double P_th = reaction_rate * 167 * 1.602 * 1e-13;
double Pabs_max = reaction_rate * G * E_abs * 1.602 * 1e-13 /
total_particles;

std::cout << "P_abs = " << Pabs_max << " W cm^-3" << " and " << "P_th = " <<
P_th << " W cm^-3\n";

}
```

B: Beta stopping model; C++

```cpp
#include <iostream>
#include <fstream>
#include <vector>
#include <string>
#include <cmath>
#include <cstdlib>
#include <stdio.h>
#include <stdlib.h>
#include <ctime>
#include "HITEC_functions.hpp"
using std::cerr;
using std::cout;
using std::endl;
using std::ifstream;

double einUO2E[1103];
double einUO2dEdx[1103]; //Allows for calculating electron path length within
5%
```

```cpp
double einArE[1103];
double einArdEdx[1103];
double distance_traveled;
extern int min_index;
int min_index2;
double l_beta;
double range_beta_in_fuel;
double range_beta_in_gas;
double delta_beta = 0.01;
double ediff[1103] ;
double ediff2[1103];
std::vector<double> Edepbg_total;
std::vector<double> Edepig_total;
std::vector<double> Edepag_total;
std::vector<double> makes_it_total;


int main(){

srand (time(NULL));

      ifstream indata1;
      ifstream indata2;
      double num1;
      double num2;
      std::vector<double> x;
      std::vector<double> y;

double pressure; //torr
int T_emitter; //K
int T_collector; //K
double range_ff;

std::cout << "\nEnter Pressure: \n";
std::cin >> pressure;
      double ratio = pressure / 760;

indata1.open("einUO2.txt"); // opens the file
   if(!indata1) { // file couldn't be opened

      cerr << "Error: file could not be opened" << endl;
      exit(1);

   }
indata1 >> num1;
   while ( !indata1.eof() ) { // keep reading until end-of-file

            x.push_back(num1);
      indata1 >> num1; // sets EOF flag if no value found

   }

   indata1.close();
   std::cout << "End-of-file reached.." << x.size() << endl;

indata2.open("einAr.txt"); // opens the file
   if(!indata2) { // file couldn't be opened
```

```cpp
        cerr << "Error: file could not be opened" << endl;
        exit(1);

    }
indata2 >> num2;
    while ( !indata2.eof() ) { // keep reading until end-of-file

            y.push_back(num2);
        indata2 >> num2; // sets EOF flag if no value found

    }

    indata2.close();
    std::cout << "End-of-file reached.." <<y.size()<< endl;


for(int i = 0; i < 2206 / 2; i++){

        density = 10.22;
        einUO2E[i] = x[i * 2];
        einUO2dEdx[i] = x[(i * 2) + 1] * density * 0.1; // MeV/mm;

}

for(int i = 0; i < 2206 / 2; i++){

        density = 0.00178 * ratio;
        einArE[i] = y[i * 2];
        einArdEdx[i] = y[(i * 2) +1] * density * 0.1; // MeV/mm ;

}

x.clear();
y.clear();

int k;
int index;
double d;
double phi;
double theta;
double Edep_beta;
r = 3;
R = 5;
double Enew_beta;

for(int a = 0; a < total_layers_beta; a++){
        int makes_it = 0; //number of particles in the layer that make it to
the gas
        int stops_before_gas = 0; // '' stop before the gas
        int stops_in_gas = 0; // '' stop before the gas. Usually not useful
        int stops_after_gas = 0; // '' stop before the gas. Useful to calculate
additional heat dissipated by the other electrode
        double Edepbg = 0; //energy equivalent of stops_before_gas
        double Edepig = 0; // '' stops_in_gas
        double Edepag = 0; // '' stops_after_gas

for(int j = 0; j < particles_per_layer; j++){
```

```
Ebeta = ((double) rand()/RAND_MAX) * 5 +0.01;

          min_index = 0;

    for(int i = 0; i < 1103; i++){

      ediff[i] = abs(Ebeta-einUO2E[i]);

    }

    for(int i = 0; i < 1103; i++){

      if(ediff[i+1] < ediff[i]){

          min_index++;

      }
    }

range_beta_in_fuel = range_beta(einUO2E, einUO2dEdx, min_index);
d = (a + (double) rand()/RAND_MAX) * delta_beta ; //choses a particle
distance within the layer
 phi = ((double) rand()/RAND_MAX) * pi / 2; //random angle between 0 and
pi/2, phi.
theta = ((double) rand()/RAND_MAX) * pi / 2; //random angle between 0 and
pi/2, theta. should be between 0 and pi for electrons
l_beta = 1/sin(phi)*((d-r) * cos(theta) + sqrt(0.5 * (r * (r + 2 * d) -
pow(d,2) + pow(d - r, 2) * cos(2 * theta)))); //use for electrons


if (l_beta < range_beta_in_fuel) {

      makes_it++;
      distance_traveled = 0;
      k = 0;

      while(l_beta >= distance_traveled){

      k++;
      index = min_index - k;
      distance_traveled = 0;

      for(int m = index; m < min_index; m++){

      distance_traveled += 0.5 * (einUO2dEdx[m] +
einUO2dEdx[m+1])*(einUO2E[m+1]-einUO2E[m]);

}
}
      Enew_beta = Ebeta - (einUO2E[min_index]-einUO2E[index]);

          min_index2 = 0;

    for(int i = 0; i < 1103; i++){

      ediff2[i] = abs(Enew_beta-einArE[i]);
```

```
        }

    for(int i = 0; i < 1103; i++){

        if(ediff2[i+1] < ediff2[i]){

                min_index2++;

            }
        }
    range_beta_in_gas = range_beta(einArE, einArdEdx, min_index2);
    double stopping =  einArdEdx[min_index2];
    double L_beta = 1/sin(phi)*((r-R) * cos(theta) + sqrt(0.5 * (R * (R + 2 *
r) - pow(r,2) + pow(r - R, 2) * cos(2 * theta))));

if(range_beta_in_gas < L_beta){

        stops_in_gas++;
        Edepig+= Enew_beta;

}
else{

    Edepig+= L_beta * stopping;
    Edepag+= Enew_beta - Edepig;
    stops_after_gas++;
}

}

else{
        Edepbg += Ebeta;
        stops_before_gas++;

}

}
            Edepbg_total.push_back(Edepbg);
            Edepig_total.push_back(Edepig);
            Edepag_total.push_back(Edepag);
            makes_it_total.push_back(makes_it);
//std::cout << Edepbg << "     " << Edepig << "   " << Edepag << "   " <<
makes_it << "\n";
}

int dummy = 0; //keeps track of layers that don't contribute to plasma
ionization

for(int i = 0; i < Edepig_total.size(); i++){

    E_abs += Edepig_total[i];
    total_particles += makes_it_total[i];

    if(Edepig_total[i] == 0){

            dummy++;
```

```cpp
        }

        std::cout << E_abs << "    " << Edepig_total[i] << "    " <<
total_particles << "    " << makes_it_total[i] << "\n";
    }
    //Output Parameters, P_th and Pabs_max. The latter may be scaled by specific
    reactor spatial profiles obtained via netronics codes.
    double G = (total_layers_beta - dummy) * delta_beta * 2 * r/ (pow(R,2) -
pow(r,2));
    double reaction_rate = 2.5e13;
    double P_th = reaction_rate * 167 * 1.602 * 1e-13;
    double Pabs_max = reaction_rate * G * E_abs * 1.602 * 1e-13 /
total_particles;
    double f_plus = Pabs_max /(26.4 * 1.602 * 1e-19);
    double n_e = sqrt(f_plus / (2.5 * 1e-7 * pow(5,-1.3)));

    std::cout << total_particles << "\n";

    std::cout << "P_abs = " << Pabs_max << " W cm^-3\n";
    std::cout << "Source Rate Densithy = " << f_plus << " ionizations s^-1 cm^-
3\n";
    std::cout << "P_th = " << P_th << " W cm^-3\n";
    std::cout << "n_e = " << n_e << " cm^-3\n";


}
```

C: Header File; C++

```cpp
//Physical constants
extern double me;//kg
extern double mne;//kg
extern double mar;//kg
extern double mkr;//kg
extern double mxe;//kg
extern double c; //m s^-1
extern double hbar;// J s
extern double Vo; // m*s^-1
extern double V1;
extern double Vrel;
extern double ao; //m, Bohr radius
extern double kboltz; //m^2 kg s^-2 K^-1
extern double eV ; //J
extern double eps; //permittivity
extern double nav; //Avogadro's #
extern double pi; //Pi
extern double sig_steffboltz;
//Stopping power variables
extern double density; //g*cm^-3
extern double Z; //atomic number of heaviest component in fuel or gas
extern double A; //atomic mass of heaviest component in fuel or gas
extern double Zg;
extern double Ag;
extern double density_g;
extern double r; //mm inner radius (emitter)
extern double R; //mm outer radius (collector)
extern double h;
extern double rhoel; //m^-3
```

```
extern double Vf; //m*s^-1
extern double massisotope; //atomic mass of ff
extern double Zff; //atomic number of ff
extern double Eff; // energy of ff (MeV)
extern double E_abs; // energy absorbed in gas (MeV)
extern int total_particles; //total number of particles that make it into the
gas
extern int particles_per_layer; //number of events
extern int total_layers; //number of layers. particles_per_layer = 10000 and
total_layers = 30 yields a run time of about 10 seconds.
extern int total_layers_beta;
extern double delta; //width of layer.
extern double Ebeta;
extern double elasticv[246];
extern double elasticxs[246];
extern double Im;
extern double M;
extern double n_a;
extern double T_a;
extern double P_abs;
extern double T_e;
extern double n_e;
extern double wi;
extern double alpha;
extern double xi;
extern double eta;
extern double P_th;
extern double T_emitter;
extern double T_collector;
extern double phi_emitter;
extern double emissivity;
extern double thermal_conductivity;
extern double Q_tot;
extern double I_th;
extern double Vmax;
extern double Imax;
extern double Pmax;


double range_calculator(double Cf, double energy[], double HdEdx[]);
double range_beta(double energy_beta[], double edEdx[], int min_index);
void plasma_params(double P_abs, double elasticv[], double elasticxs[],
double Im, double wi, double alpha, double xi, double eta, double M, double
n_a, double T_a, double& T_e, double& n_e);
void thermionic_current(double P_th, double h, double& T_emitter, double
T_collector, double phi_emitter, double emissivity, double
thermal_conductivity, double& I_th, double& Q_tot);
void TEC_output(double I_th, double n_e_emitter, double n_e_collector, double
T_e_emitter, double T_e_collector, double T_emitter, double& Vmax, double&
Imax, double& Pmax);
```

D: HITEC model; MATLAB

```
%Constants
me = 9.11*10^-31; %kg
mhe = 6.64*10^-27; %kg
mne = 3.35*10^-26; %kg
mar = 6.63*10^-26; %kg
```

```matlab
mkr = 1.39*10^-25; %kg
mxe = 2.18*10^-25; %kg
c = 299792458; %m*s^-1
hbar = (6.626*10^-34)/(2*pi);
Vo = hbar/(me*5.29*10^-11); %m*s^-1
ao = 0.529*10^-10; %m
kboltz = 1.380648*10^-23;
eV = 1.602*10^-19;
eps = 8.85*10^-12;
nav = 6.022*10^23;
pressure = 380;%torr
Temitter = 1900;
Tcollector = 800;
RR = 1 * 10^14; %SIG_fiss*flux. Can back calculate by
ng = 133.32*pressure/(kboltz*300); %m^-3
Im = 15.76*0.75; %eV
stop_before_gas = 0;
toward_emitter=0;
toward_collector=0;
stop_in_emitter = 0;
stop_in_collector=0;
stop_in_gas = 0;
for k = 1:28
for j = 1:10000
    clear range
    density = 10.22; %g*cm^-3
    Z = 92;
    A = 235;
    rhoel = Z/A*nav*density*10^6; %m^-3
    Vf = (hbar/me)*(3*pi^2*rhoel)^(1/3); %m*s^-1
    x = round((length(events100k)-1)*rand);
    if mod(x,2) == 0
      x = x + 1;
    else
    end
    massisotope = events100k(x,3);
    Zff = events100k(x,2);
    Eff = events100k(x+1,1);
    energy = HinU(1:62,1)*massisotope;
    a = ao/(Zff^(2/3)+Z^(2/3))^1/2;
    mu=A/massisotope;
    for i=length(energy):-1:1
        V1 = c*sqrt(2*energy(i,1)/(931.5*massisotope));
        if V1 >= Vf
            Vrel = V1*(1+Vf^2/(5*V1^2));
        else
            Vrel = 3*Vf/4*(1+(2*V1^2/(3*Vf^2))-(1/15*(V1/Vf)^4));
        end
        ereduced(i,1) =
32.53*A*energy(i,1)*10^3/(Z*Zff*(A+massisotope)*(Zff^0.23+Z^0.23));
        if ereduced(i,1)<= 30
            stoppingnuclearU(i,1) = rhoel/Z*10^-13*(8.462*10^-
15*Zff*Z*massisotope/((massisotope+A)*(Zff^0.23+Z^0.23)))*log(1+1.1383*ereduc
ed(i,1))/(2*(ereduced(i,1)+0.01321*ereduced(i,1).^0.21226+0.19593*ereduced(i,
1).^0.5));
        else
```

```matlab
            stoppingnuclearU(i,1) = rhoel/Z*10^-13*(8.462*10^-
15*Zff*Z*massisotope/((massisotope+A)*(Zff^0.23+Z^0.23)))*log(ereduced(i,1))/
(2*ereduced(i,1));
        end
        yr(i,1)= Vrel/(Vo*Zff^(2/3));
        if yr(i,1) < 0.13
            stoppingelectronicU(i,1) =
stoppingelectronicU(i+1,1)*sqrt(energy(i,1)/energy(i+1,1));
        else
        beta = 0.886 * (energy(i,1) * 10^3 / (25 * massisotope))^(1/2) /
Zff^(2/3);
        alpha = beta + 0.0378 * sin(pi * beta / 2);
        Cf = 1.13; %1 for Gases, 1.13 for U
        stoppingelectronicU(i,1) = HinU(i,2) * (Cf * Zff)^2 * (1 - exp(-
alpha)*(1.034-0.1777*exp(-0.8114*Zff)))^2;
        yr(i,1)= Vrel/(Vo*Zff^(2/3));
        end
    end
    for i = 1:length(energy)-1
        range(1,1) = 0;
        range(i+1,1) = range(i,1)+(1-
mu*stoppingnuclearU(i,1).*range(i,1)./(2*energy(i,1)))*(energy(i+1,1)-
energy(i,1))./(stoppingnuclearU(i,1)+stoppingelectronicU(i,1));
    end
    ediff = abs(Eff-energy);
    erange = find(ediff == min(ediff));
    if length(erange) > 1
        erange = erange(1);
    else
    end
range = range(erange);
ratio = pressure/760;
density = 0.00178 * ratio ; %g*cm^-3
Z = 18;
A = 40;
rhoel = Z/A*nav*density*10^6;
delta = 0.25*10^-3;
    R = 5;%mm
    r = 3;%mm
    d=(k-1+rand)*delta; %mm
    phi = pi/2*rand;
    theta = pi/2*rand;
    l=1/sin(phi)*((d-r)*cos(theta)+sqrt(1/2*(r*(r+2*d)-d^2+(d-
r)^2*cos(2*theta))));
    if l < range && l > 0
        Enew = Eff*(1-l/range)^2;
        Edepc(j) = Eff - Enew;
        for i=length(energy):-1:1
            V1 = c*sqrt(2*energy(i,1)/(931.5*massisotope));
                if V1 >= Vf
                    Vrel = V1*(1+Vf^2/(5*V1^2));
                else
                    Vrel = 3*Vf/4*(1+(2*V1^2/(3*Vf^2))-(1/15*(V1/Vf)^4));
                end
            ereduced(i,1) =
32.53*A*energy(i,1)*10^3/(Z*Zff*(A+massisotope)*(Zff^0.23+Z^0.23));
                if ereduced(i,1)<= 30
```

```
                stoppingnuclearAr(i,1) = rhoel/Z*10^-13*(8.462*10^-
15*Zff*Z*massisotope/((massisotope+A)*(Zff^0.23+Z^0.23)))*log(1+1.1383*ereduc
ed(i,1))/(2*(ereduced(i,1)+0.01321*ereduced(i,1).^0.21226+0.19593*ereduced(i,
1).^0.5));
            else
                stoppingnuclearAr(i,1) = rhoel/Z*10^-13*(8.462*10^-
15*Zff*Z*massisotope/((massisotope+A)*(Zff^0.23+Z^0.23)))*log(ereduced(i,1))/
(2*ereduced(i,1));
            end
            yr(i,1)= Vrel/(Vo*Zff^(2/3));
            if yr(i,1) < 0.13
                stoppingelectronicAr(i,1) =
stoppingelectronicAr(i+1,1)*sqrt(energy(i,1)/energy(i+1,1));
            else
            beta = 0.886 * (energy(i,1) * 10^3 / (25 * massisotope))^(1/2) /
Zff^(2/3);
            alpha = beta + 0.0378 * sin(pi * beta / 2);
            Cf = 1.0; %1 for Gases, 1.13 for U
            stoppingelectronicAr(i,1) = ratio * HinAr(i,2) * (Cf * Zff)^2 *
(1 - exp(-alpha)*(1.034-0.1777*exp(-0.8114*Zff)))^2;
            yr(i,1)= Vrel/(Vo*Zff^(2/3));
            end
        end
        clear range
    for i = 1:length(energy)-1
        range(1,1) = 0;
        range(i+1,1) = range(i,1)+(1-
mu*stoppingnuclearAr(i,1).*range(i,1)./(2*energy(i,1)))*(energy(i+1,1)-
energy(i,1))./(stoppingnuclearAr(i,1)+stoppingelectronicAr(i,1));
    end
    ediff = abs(Enew-energy);
    erange = find(ediff == min(ediff));
    if length(erange) > 1
        erange = erange(1);
    else
    end
    range = range(erange);
D = R-r+d;
L=1/sin(phi)*((D-R)*cos(theta)+sqrt(1/2*(R*(R+2*D)-D^2+(D-
R)^2*cos(2*theta))))-l;
        if L > range %means particle will fully deposit in gas
            Edepg(j) = Enew;
            stop_in_gas = stop_in_gas + 1;
        else
            Edepg(j) = Enew*(1-L/range)^2;
            if (theta >= 0) & (theta < asin(r/R))
                stop_in_emitter = stop_in_emitter + 1;
                Edepe(j) = Enew - Edepg(j);
            else
                stop_in_collector = stop_in_collector + 1;
                Edepc(j) = Enew - Edepg(j);
            end
        end
    else
        stop_before_gas = stop_before_gas + 1;
        Edepc(j) = Eff;
        Edepg(j) = 0;
    end
```

```
end
Edepg(Edepg<=0) = [];
Edepc(Edepc<=0) = [];
Edepe(Edepe<=0) = [];
Edepg_length(k) = length(Edepg);
Edepg_total(k) = sum(Edepg);
Edepc_total(k) = sum(Edepc);
Edepe_total(k) = sum(Edepe);
end
G = (2*R*delta)/(R^2-r^2);
Pabs_max = RR * G * sum(Edepg_total) * 1.602*10^-13 * (j*k)^-1;
Pth_max = RR/3.5 * 167 * 1.602 * 10^-13;


%%This section creates an axial power distribution from the center to the
%%top of the reactor whose height is H (i.e. 0 to H/2) in order to scale
%%the total ionization rate seen in the core. This is necessary to obtain
%%more accurate electrical power output values, as both the temperature and
%%work function (and therefore thermionic emission current, Ith) of the
%%emitter changes throughout the length of the fuel element.
%%Correspondingly, there will be an axially dependent emission current
%%vector such that the power output values can be iterated through all the
%%elements.

for i=1:length(P_axial)-1
    Pav_el(i) = Pabs_max * (P_axial(i,2) + P_axial(i+1,2))/2*(P_axial(i+1,1)
- P_axial(i,1));%Power density in plasma W cm^-3
    Pav_th(i) = Pth_max * (P_axial(i,2) + P_axial(i+1,2))/2*(P_axial(i+1,1) -
P_axial(i,1)) * 0.221; %Total power in fuel W
    Iav(i) = (Jth_axial(i,2)+Jth_axial(i,2))/2*(Jth_axial(i+1,1) -
Jth_axial(i,1)) * 0.6 * pi;
    phiav(i) = (Jth_axial(i,3)+Jth_axial(i,3))/2;
    T_emitter_av(i) = (axial_temperature(i,2)+axial_temperature(i,2))/2;
    A_emitter(i) = (Jth_axial(i+1,1) - Jth_axial(i,1)) * 0.6 * pi;

end


%%This section should include the gas properties of noble gasses
%%(Ne,Ar,Kr,Xe) so that ne can be calculated from the plasma deposition.
%%Currently, Penning gases haven't been calculated, so single gases will
%%be used. For single gases, Te is determined.

tgas = (Temitter + Tcollector)/2;
for t = 1:10^4 %create temperature vector
    te(t) = tgas + 20*t;
end
for k = 1:length(te)
for v = 1:length(argonxsv) %create distribution function f which is
differentiable in v
        f(k,v) = (me/(2*pi*kboltz*te(k)))^(3/2)*(exp(-
0.5*me*argonxsv(v,1).^2/(kboltz*te(k)))-exp(-Im*eV/(kboltz*te(k))));
end
    c = trapz(argonxsv(6:79,1),4*pi*argonxsv(6:79,1).^2.*f(k,6:79)');
    f(k,:) = f(k,:)/c;
end
for k = 1:length(te)
```

```matlab
    elastic(k) =
2*pi*ng*me^2/mar*(argonxsv(6,1).^6.*argonxsv(6,2).*f(k,6)'+2*trapz(argonxsv(6
:79,1),argonxsv(6:79,1).^5.*argonxsv(6:79,2).*f(k,6:79)'));
    inelastic(k) = 4*6*exp(-
Im*eV/(kboltz*te(k)))*(Im*eV/(kboltz*te(k)))^1.5*sqrt(2*pi/(me*Im*eV))*(eV^2/
(4*pi*eps))^2;
    conventional(k) =
4*pi*ng*me^2/mar*trapz(argonxsv(6:79,1),argonxsv(6:79,1).^5.*argonxsv(6:79,2)
.*f(k,6:79)');
    kdr(k) = ((8.1*10^-7)*(tgas/300)^-.86*(te(k)/300).^-0.64);
    Power_cp(k) = wiar*eV./kdr(k).*(elastic(k)*(1-tgas./te(k))/(Im*eV-
te(k).*kboltz)).^2;%(8.1.*10^-7)*(tgas/300).^0.86.*(te(k)/300)^0.64%
    nu = 10^-7; %gives ne at collector ~ 10^12 cm^-3
    Power_aux(k) = 10^-6*ng^2*10^-7*(elastic(k)/ng + 2.34 * 10^-
14*(te(k)/11603).^0.59 * exp(-17.44/te(k)*11603) * 15.76*eV + 2.48 * 10^-14 *
(te(k)/11603).^0.33 * exp(-12.78/te(k)*11603) * 12.14 * eV);%gives power
density vs. Te from other electromagnetic source
end
for m =1:length(Pfuel_factor)
    Pav_el_element = Pav_el * Pfuel_factor(m);
    Pav_th_element = Pav_th * Pfuel_factor(m);
for i = 1:length(Pav_el_element)
    ediff = abs(Pav_el_element(i)-Power_cp);
    te_Pav = find(ediff == min(ediff));
    if length(te_Pav) > 1
       te_Pav = te_Pav(1);
    else
    end
    %%with Te and ne at the emitter, we can calculate the power output of a
    %%single cell. The code will default to a constant temperature and
    %%density at the collector. However, you can modify this by using the
    %%Paux variable at a given ionization fraction (therefore you know ne at
the
    %%collector)
A_E = 2 * A_emitter(i);
A_C = A_E * 2;
phi_E = phiav(i);
phi_C = 1.7;
delta_phi = phi_E-phi_C;
TE = T_emitter_av(i)/11603;
TC = Tcollector/11603;
Ith = 2 * Iav(i);
Iback = A_C * 120 * (TC * 11603)^2 * exp(-phi_C/TC);
neE = sqrt(Pav_el_element(i)/(kdr(te_Pav)*wiar*eV));
neC = 5 * 10^12 * sqrt(Pfuel_factor(m));
TeE = te(te_Pav)/11603;
TeC = 13350/11603;
IeE = A_E * eV * neE * sqrt(TeE * kboltz * 11603/(2 * pi * me)) * 100;
Ratio = IeE/Ith;
IeC = A_C * eV * neC * sqrt(TeC * kboltz * 11603/(2 * pi * me)) * 100;
mu = 150;
IiE = IeE/mu;
IiC = IeC/mu;
if Ith>IiE
    x=0:0.01*Ith:Ith;
else
    x =0:0.01*IiE:IiE;
end
```

```
for j =1:length(x)
    if x(j) > Ith+IiE-IeE
        vE(j) = TeE*log((Ith+IiE-x(j))./IeE);
    else
        vE(j) = TE*log((Ith+IiE)./(x(j)+IeE));
    end
        vC(j) = TeC*log(IeC./(x(j)+IiE));
        vout(j) = vE(j)+vC(j)+delta_phi;
    end
P_nominal(i,:) = x.*vout;
Pmax(i) = max(P_nominal(i,:));
plot(vout,x.*vout)
hold on
end
Pout(m) = sum(Pmax);
Pth(m) = sum(Pav_th_element) * 2;
efficiency(m) = Pout(m)/Pth(m);
end
Pout_total = sum(Pout)
Pth_total = sum(Pth)
efficiency_total = Pout_total/Pth_total
```

E: MCNP Reactor model

```
HITEC Space Reactor
c ---- Cell ----
1    0               -1                     u=3              imp:n=1
70   1    -10.28      1 -80                       u=3         imp:n=1
9    1    -10.28      80 -9                    u=3         imp:n=1
2    9    -5          2 -3                     u=3      imp:n=1
92   9    -5          3 -4                   u=3         imp:n=1
3    2    -10.97      9 -42                     u=3         imp:n=1
76   3    -1.78e-3    42 -2                     u=3         imp:n=1
4    9    -5          4 -81 70 71 72 73      u=3          imp:n=1
71   8    -8.97       -70 74                    u=3         imp:n=1
72   8    -8.97       -71 75                    u=3          imp:n=1
73   8    -8.97       -72 76                    u=3          imp:n=1
74   8    -8.97       -73 77                    u=3          imp:n=1
81   0               -74                     u=3          imp:n=1
82   0               -75                     u=3          imp:n=1
83   0               -76                     u=3          imp:n=1
84   0               -77                     u=3          imp:n=1
75   4    -6.56       70 71 72 73 81          u=3          imp:n=1
8    4    -6.56       -6                      u=2          imp:n=1
5    0               -6              lat=2    u=1          imp:n=1
                 fill=-12:12 -12:12 0:0
     2 2 2 2 2 2 2 2 2 2 2 2 2 2 2 2 2 2 2 2 2 2 2 2 2
      2 2 2 2 2 2 2 2 2 2 2 2 2 2 2 2 2 2 2 2 2 2 2 2 2
       2 2 2 2 2 2 2 2 2 2 2 2 2 2 2 2 2 2 2 2 2 2 2 2 2
        2 2 2 2 2 2 2 2 2 2 2 2 3 3 3 3 3 3 3 3 3 2 2 2
         2 2 2 2 2 2 2 2 2 2 2 3 3 3 3 3 3 3 3 3 3 2 2 2
          2 2 2 2 2 2 2 2 2 2 3 3 3 3 3 3 3 3 3 3 3 2 2 2
           2 2 2 2 2 2 2 2 2 3 3 3 3 3 3 3 3 3 3 3 3 2 2 2
            2 2 2 2 2 2 2 2 3 3 3 3 3 3 3 3 3 3 3 3 3 2 2 2
             2 2 2 2 2 2 2 3 3 3 3 3 3 3 3 3 3 3 3 3 3 2 2 2
              2 2 2 2 2 2 3 3 3 3 3 3 3 3 3 3 3 3 3 3 3 2 2 2
               2 2 2 2 2 3 3 3 3 3 3 3 3 3 3 3 3 3 3 3 3 2 2 2
```

```
                 2 2 2 2 3 3 3 3 3 3 3 3 3 3 3 3 3 3 3 3 3 3 3 3 3 3 2 2 2
                2 2 2 3 3 3 3 3 3 3 3 3 3 3 3 3 3 3 3 3 3 3 3 3 3 3 3 2 2 2
               2 2 2 3 3 3 3 3 3 3 3 3 3 3 3 3 3 3 3 3 3 3 3 3 3 3 2 2 2 2
              2 2 2 3 3 3 3 3 3 3 3 3 3 3 3 3 3 3 3 3 3 3 3 3 3 2 2 2 2 2
             2 2 2 3 3 3 3 3 3 3 3 3 3 3 3 3 3 3 3 3 3 3 3 3 2 2 2 2 2 2
            2 2 2 3 3 3 3 3 3 3 3 3 3 3 3 3 3 3 3 3 3 3 3 2 2 2 2 2 2 2
           2 2 2 3 3 3 3 3 3 3 3 3 3 3 3 3 3 3 3 3 3 3 2 2 2 2 2 2 2 2
          2 2 2 3 3 3 3 3 3 3 3 3 3 3 3 3 3 3 3 3 3 2 2 2 2 2 2 2 2 2
         2 2 2 3 3 3 3 3 3 3 3 3 3 3 3 3 3 3 3 3 2 2 2 2 2 2 2 2 2 2
        2 2 2 3 3 3 3 3 3 3 3 3 3 3 3 3 3 3 3 2 2 2 2 2 2 2 2 2 2 2
       2 2 2 3 3 3 3 3 3 3 3 3 3 3 3 3 3 3 2 2 2 2 2 2 2 2 2 2 2 2
      2 2 2 2 2 2 2 2 2 2 2 2 2 2 2 2 2 2 2 2 2 2 2 2 2 2 2 2 2 2
     2 2 2 2 2 2 2 2 2 2 2 2 2 2 2 2 2 2 2 2 2 2 2 2 2 2 2 2 2 2 2
    2 2 2 2 2 2 2 2 2 2 2 2 2 2 2 2 2 2 2 2 2 2 2 2 2 2 2 2 2 2 2 2
2
6    0                   -7     fill=1                    imp:n=1
10   5     -1.85    (91 -5)((30 -10 52):-30)          imp:n=1
50   6     -2.52    (91 -5)(30 -10 -52)           imp:n=1
11   5     -1.85    (91 -5)((31 -11 -53):-31)         imp:n=1
51   6     -2.52    (91 -5)(31 -11 53)            imp:n=1
12   5     -1.85    (91 -5)((32 -12 50):-32)          imp:n=1
52   6     -2.52    (91 -5)(32 -12 -50)           imp:n=1
13   5     -1.85    (91 -5)((33 -13 -51):-33)         imp:n=1
53   6     -2.52    (91 -5)(33 -13 51)            imp:n=1
14   5     -1.85    (91 -5)((34 -14 54):-34)          imp:n=1
54   6     -2.52    (91 -5)(34 -14 -54)           imp:n=1
15   5     -1.85    (91 -5)((35 -15 -55):-35)         imp:n=1
55   6     -2.52    (91 -5)(35 -15 55)            imp:n=1
16   5     -1.85    (91 -5)((36 -16 56):-36)          imp:n=1
56   6     -2.52    (91 -5)(36 -16 -56)           imp:n=1
17   5     -1.85    (91 -5)((37 -17 57):-37)          imp:n=1
57   6     -2.52    (91 -5)(37 -17 -57)       imp:n=1
18   5     -1.85    (91 -5)((38 -18 58):-38)          imp:n=1
58   6     -2.52    (91 -5)(38 -18 -58)       imp:n=1
19   5     -1.85    (91 -5)((39 -19 59):-39)          imp:n=1
59   6     -2.52    (91 -5)(39 -19 -59)           imp:n=1
20   5     -1.85    (91 -5)((40 -20 -60):-40)     imp:n=1
60   6     -2.52    (91 -5)(40 -20 60)        imp:n=1
21   5     -1.85    (91 -5)((41 -21 -61):-41)         imp:n=1
61   6     -2.52    (91 -5)(41 -21 61)                          imp:n=1
7    5     -1.85    (91 -5 7 -8 10 11 12 13 14 15 16 17 18 19 20 21):(-91 62 -
8):(-63 5 -8)
                                                 imp:n=1
99   0              8:-62:63                              imp:n=0

c ---- Fuel/Gas/Reflector -----
1    cz    0.14
80   cz    0.29
9    cz    0.295
42   cz    0.30
2    cz    0.5
3    cz    0.51
4    cz    0.55
81   cz    0.95
8    cz    50
c ---- Drum Outer Cylinders ----
10   c/z    0 40 9.5
11   c/z    0 -40 9.5
```

101

```
12     c/z      40 0 9.5
13     c/z     -40 0 9.5
14     c/z      34.64 20 9.5
15     c/z      34.64 -20 9.5
16     c/z     -34.64 20 9.5
17     c/z     -34.64 -20 9.5
18     c/z      20 34.64 9.5
19     c/z      20 -34.64 9.5
20     c/z     -20 34.64 9.5
21     c/z     -20 -34.64 9.5
c ---- inner cylinders ----
30     c/z      0 40 8.5
31     c/z      0 -40 8.5
32     c/z      40 0 8.5
33     c/z     -40 0 8.5
34     c/z      34.64 20 8.5
35     c/z      34.64 -20 8.5
36     c/z     -34.64 20 8.5
37     c/z     -34.64 -20 8.5
38     c/z      20 34.64 8.5
39     c/z      20 -34.64 8.5
40     c/z     -20 34.64 8.5
41     c/z     -20 -34.64 8.5
c ---- Planes ----
50     px      38
51     px     -38
52     py      38
53     py     -38
54     p       1.732 1 0 76
55     p      -1.732 1 0 -76
56     p      -1.732 1 0 76
57     p      -1.732 -1 0 76
58     p       1 1.732 0 76
59     p       1 -1.732  0 76
60     p       1 -1.732 0 -76
61     p       1 1.732  0 -76
62     pz     -70
63     pz      70
c ---- Heat Pipes ----
70     c/z      0     0.75    0.15
71     c/z      0    -0.75    0.15
72     c/z      0.75   0      0.15
73     c/z     -0.75   0      0.15
74     c/z      0     0.75    0.13
75     c/z      0    -0.75    0.13
76     c/z      0.75   0      0.13
77     c/z     -0.75   0      0.13
c ---- Axial Limit ----
91      pz     -50
5       pz      50
c ---- Hex Macrobody ----
6      rhp     0 0 -50  0 0 100  1.5 0 0
7      rcc     0 0 -50  0 0 100  30

c ---- Materials ----
m1     92235.65c    0.185
       92238.65c    0.815
       16000        2
```

102

```
m2      92235.65c       0.9
        92238.65c       0.1
        16000           2
        74000.21c       1
m3      18000           0.5
        55133           1e-3
m4      40000           1
        1001.24c        1.85
m5      4009.21c        1
m6      5010.42c        4
        6000.24c        1
m7      74000.21c       1
m8      28000.42c       -0.57
        74000.21c       -0.14
        24000.42c       -0.22
m9      40000.42c       1
m10     42000.42c       1
c ---- Tallies ----
c f7:n    (9 2<u=3)
c tmp1  1.7e-7
c thtme 0
c fmesh4:n  origin= 0 0 0            imesh=40   iints=400
c                                    jmesh=40   jints=400
c                                    kmesh=1    kints=1
c                                    emesh=1e-7 2
c                                    eints=4 1
c f14:n (9 2<u=3)
c e14    1.00000000e-10 1.25892541e-10 1.58489319e-10 1.99526231e-10
c        2.51188643e-10 3.16227766e-10 3.98107171e-10 5.01187234e-10
c        6.30957344e-10 7.94328235e-10 1.00000000e-09 1.25892541e-09
c        1.58489319e-09 1.99526231e-09 2.51188643e-09 3.16227766e-09
c        3.98107171e-09 5.01187234e-09 6.30957344e-09 7.94328235e-09
c        1.00000000e-08 1.25892541e-08 1.58489319e-08 1.99526231e-08
c        2.51188643e-08 3.16227766e-08 3.98107171e-08 5.01187234e-08
c        6.30957344e-08 7.94328235e-08 1.00000000e-07 1.25892541e-07
c        1.58489319e-07 1.99526231e-07 2.51188643e-07 3.16227766e-07
c        3.98107171e-07 5.01187234e-07 6.30957344e-07 7.94328235e-07
c        1.00000000e-06 1.25892541e-06 1.58489319e-06 1.99526231e-06
c        2.51188643e-06 3.16227766e-06 3.98107171e-06 5.01187234e-06
c        6.30957344e-06 7.94328235e-06 1.00000000e-05 1.25892541e-05
c        1.58489319e-05 1.99526231e-05 2.51188643e-05 3.16227766e-05
c        3.98107171e-05 5.01187234e-05 6.30957344e-05 7.94328235e-05
c        1.00000000e-04 1.25892541e-04 1.58489319e-04 1.99526231e-04
c        2.51188643e-04 3.16227766e-04 3.98107171e-04 5.01187234e-04
c        6.30957344e-04 7.94328235e-04 1.00000000e-03 1.25892541e-03
c        1.58489319e-03 1.99526231e-03 2.51188643e-03 3.16227766e-03
c        3.98107171e-03 5.01187234e-03 6.30957344e-03 7.94328235e-03
c        1.00000000e-02 1.25892541e-02 1.58489319e-02 1.99526231e-02
c        2.51188643e-02 3.16227766e-02 3.98107171e-02 5.01187234e-02
c        6.30957344e-02 7.94328235e-02 1.00000000e-01 1.25892541e-01
c        1.58489319e-01 1.99526231e-01 2.51188643e-01 3.16227766e-01
c        3.98107171e-01 5.01187234e-01 6.30957344e-01 7.94328235e-01
c        1.00000000e+00 1.25892541e+00 1.58489319e+00 1.99526231e+00
c        2.51188643e+00 3.16227766e+00 3.98107171e+00 5.01187234e+00
c        6.30957344e+00 7.94328235e+00 1.00000000e+01 1.25892541e+01
c        1.58489319e+01 1.99526231e+01 2.51188643e+01 3.16227766e+01
c        3.98107171e+01 5.01187234e+01 6.30957344e+01 7.94328235e+01
c f24:n 7
```

103

```
c e24 1.00000000e-10 1.25892541e-10 1.58489319e-10 1.99526231e-10
c        2.51188643e-10 3.16227766e-10 3.98107171e-10 5.01187234e-10
c        6.30957344e-10 7.94328235e-10 1.00000000e-09 1.25892541e-09
c        1.58489319e-09 1.99526231e-09 2.51188643e-09 3.16227766e-09
c        3.98107171e-09 5.01187234e-09 6.30957344e-09 7.94328235e-09
c        1.00000000e-08 1.25892541e-08 1.58489319e-08 1.99526231e-08
c        2.51188643e-08 3.16227766e-08 3.98107171e-08 5.01187234e-08
c        6.30957344e-08 7.94328235e-08 1.00000000e-07 1.25892541e-07
c        1.58489319e-07 1.99526231e-07 2.51188643e-07 3.16227766e-07
c        3.98107171e-07 5.01187234e-07 6.30957344e-07 7.94328235e-07
c        1.00000000e-06 1.25892541e-06 1.58489319e-06 1.99526231e-06
c        2.51188643e-06 3.16227766e-06 3.98107171e-06 5.01187234e-06
c        6.30957344e-06 7.94328235e-06 1.00000000e-05 1.25892541e-05
c        1.58489319e-05 1.99526231e-05 2.51188643e-05 3.16227766e-05
c        3.98107171e-05 5.01187234e-05 6.30957344e-05 7.94328235e-05
c        1.00000000e-04 1.25892541e-04 1.58489319e-04 1.99526231e-04
c        2.51188643e-04 3.16227766e-04 3.98107171e-04 5.01187234e-04
c        6.30957344e-04 7.94328235e-04 1.00000000e-03 1.25892541e-03
c        1.58489319e-03 1.99526231e-03 2.51188643e-03 3.16227766e-03
c        3.98107171e-03 5.01187234e-03 6.30957344e-03 7.94328235e-03
c        1.00000000e-02 1.25892541e-02 1.58489319e-02 1.99526231e-02
c        2.51188643e-02 3.16227766e-02 3.98107171e-02 5.01187234e-02
c        6.30957344e-02 7.94328235e-02 1.00000000e-01 1.25892541e-01
c        1.58489319e-01 1.99526231e-01 2.51188643e-01 3.16227766e-01
c        3.98107171e-01 5.01187234e-01 6.30957344e-01 7.94328235e-01
c        1.00000000e+00 1.25892541e+00 1.58489319e+00 1.99526231e+00
c        2.51188643e+00 3.16227766e+00 3.98107171e+00 5.01187234e+00
c        6.30957344e+00 7.94328235e+00 1.00000000e+01 1.25892541e+01
c        1.58489319e+01 1.99526231e+01 2.51188643e+01 3.16227766e+01
c        3.98107171e+01 5.01187234e+01 6.30957344e+01 7.94328235e+01
kcode    1e3  1   50   5e4
ksrc     10.1  0.5    0
         10.1  8.5    0
         10.1  16.5   0
         10.1  24.5   0
         10.1  32.5   0
         10.1  40.5   0
         10.1  48.5   0
         10.1  56.5   0
         10.1  64.5   0
         10.1  72.5   0
         10.1  79.5   0
         30.1  10.5   0
         30.1  18.5   0
         30.1  26.5   0
         30.1  34.5   0
         30.1  42.5   0
         30.1  50.5   0
         30.1  58.5   0
         30.1  66.5   0
         30.1  74.5   0
         30.1  78.5   0
         50.1  1.5    0
         50.1  9.5    0
         50.1  17.5   0
         50.1  25.5   0
         50.1  33.5   0
         50.1  41.5   0
```

```
50.1  49.5  0
50.1  57.5  0
50.1  65.5  0
50.1  73.5  0
70.1  3.5   0
70.1  11.5  0
70.1  19.5  0
70.1  27.5  0
70.1  35.5  0
70.1  43.5  0
70.1  51.5  0
70.1  59.5  0
70.1  67.5  0
70.1  75.5  0
print
mode n
```

References

1. Gibson, M. A., Poston, D. I., Mcclure, P., Godfroy, T., Sanzi, J., & Briggs, M. H. (2018). The Kilopower Reactor Using Stirling TechnologY (KRUSTY) Nuclear Ground Test Results and Lessons Learned. *2018 International Energy Conversion Engineering Conference*. doi: 10.2514/6.2018-4973

2. NASA Technology Roadmaps TA 3: Space Power and Energy Storage. (2015).

3. Nuclear Thermal Propulsion. (n.d.). Retrieved from https://www.sbir.gov/sbirsearch/detail/1547743.

4. BWX Technologies, Inc.: People Strong, Innovation Driven. (n.d.). Retrieved from https://www.bwxt.com/what-we-do/nuclear-thermal-propulsion-ntp.

5. NASA Technology Roadmaps TA 2: In-Space Propulsion Technologies. (2015)

6. Morrison, C. G. (2019). Temperature and Power Specific Mass Scaling for LEU Closed-Cycle Brayton Systems for Space Surface Power and Nuclear Electric Propulsion. *Nuclear and Emerging Technologies for Space, American Nuclear Society Topical Meeting*.

7. Mason, L. S. (2001). A comparison of Brayton and Stirling space nuclear power systems for power levels from 1 kilowatt to 10 megawatts. *AIP Conference Proceedings*. doi: 10.1063/1.1358045

8. Ceramic matrix composites take flight in LEAP jet engine. (2017, January 3). Retrieved from https://www.ornl.gov/news/ceramic-matrix-composites-take-flight-leap-jet-engine.

9. TYPE-CERTIFICATE DATA SHEET No. E.110 for Engine LEAP-1A & LEAP-1C series engines. (n.d.). Retrieved from https://www.easa.europa.eu/sites/default/files/dfu/EASA E 110 TCDS Issue 2 LEAP-1A_1C_20161103_1.0.pdf.

10. Idaho National Laboratory. (2015). *Atomic power in space Ii: a history of space nuclear power and propulsion in the United States*. Idaho Falls, Idaho?

11. Bennett, G. (n.d.). A look at the Soviet space nuclear power program. *Proceedings of the 24th Intersociety Energy Conversion Engineering Conference*. doi: 10.1109/iecec.1989.74620

12. Thermionics Quo Vadis? (2001). doi: 10.17226/10254

13. Baksht, F. G., Dyuzhev, G. A., Martsinovsky, A. M., & Hansen, L. K. (1978). *Thermionic converters and low-temperature plasma*. Springfield: NTIS.

14. F. JAMERSON, "Investigations on the Direct Energy Conversion of Nuclear Fission Energy to Electrical Energy in a Plasma Diode," Nonr-3109(00), Office of Naval Research (1967).

15. G.A. Batyrbekov et al., Properties of the inert-gas plasma formed by uranium-fission fragments in a nuclear reactor, Zh. Tekh. Fiz. **46**, 2318-2320, 1976

16. Melnikov, S. P. (2016). *Lasers with nuclear pumping*. Place of publication not identified: Springer International Pu.

17. Larsson, M., & Orel, A. E. (2012). Diatomic Ions. In *Dissociative recombination of molecular ions*. Cambridge: Cambridge Univ. Press.

18. Kaganovich, I. D., Startsev, E., & Davidson, R. C. (2003). Scaling Cross Sections for Ion-atom Impact Ionization. doi:10.2172/814022

19. Ziegler, J. F., Biersack, J. P., & Ziegler, M. D. (2015). *SRIM, the stopping and range of ions in matter*. Chester, MD: SRIM.

20. Ziegler, J., & Biersack, J. (1985). The Stopping and Range of Ions in Matter. In *Treatise on heavy-ion science*. New York: Plenum.

21. Hajnrych, J. G., Filliatre, P., & Geslot, B. (2018). Penetration of gases by fission fragments—Comparison between selected models and the data. *Nuclear Instruments and Methods in Physics Research Section A: Accelerators, Spectrometers, Detectors and Associated Equipment, 911*, 15-18. doi:10.1016/j.nima.2018.09.118

22. Brandt, W., & Kitagawa, M. (1982). Effective stopping-power charges of swift ions in condensed matter. *Physical Review B, 25*(5631). doi:https://doi.org/10.1103/PhysRevB.25.5631

23. Introduction of ESTAR, PSTAR, and ASTAR. (n.d.). Retrieved September 04, 2020, from https://physics.nist.gov/PhysRefData/Star/Text/intro.html

24. Platzman, R. (1961). Total ionization in gases by high-energy particles: An appraisal of our understanding. *The International Journal of Applied Radiation and Isotopes, 10*(2-3), 116-127. doi:10.1016/0020-708x(61)90108-9

25. Fowler, R. H. (1921). Contributions to the theory of the motion of alpha-particles through matter. *Proceedings of the Cambridge Philosophical Society, 21*(5).

26. Spencer, L. V., & Fano, U. (1954). Energy Spectrum Resulting from Electron Slowing Down. *Physical Review, 93*(6), 1172-1181. doi:10.1103/physrev.93.1172

27. Spencer, L. V. (1984). On the Theory of Ionization and Excitation Yields. *Radiation Research, 97*(2), 219. doi:10.2307/3576274

28. Platzman, R. L. (1955). Subexcitation Electrons. *Radiation Research, 2*(1), 1. doi:10.2307/3570224

29. Jesse, W. P., & Sadaukis, J. (1957). Absolute Energy to Produce an Ion Pair by Beta Particles from S-35. *Physical Review,107*(3).

30. Schmitt, H. W., & Leachman, R. B. (1956). IonizationvsEnergy Relation for Fission Fragments. *Physical Review, 102*(1), 183-185. doi:10.1103/physrev.102.183

31. Mikuš, O., Lukáč, P., Morva, I., Zábudlá, Z., Trnovec, J., & Morvová, M. (2009). Electron and gas temperature dependences of the dissociative recombination coefficient of molecular ions Ne_2^+ with electrons. *Plasma Sources Science and Technology, 18*(2), 025031. doi:10.1088/0963-0252/18/2/025031

32. Lukáč, P., Mikuš, O., Morva, I., Zábudlá, Z., Trnovec, J., & Morvová, M. (2011). Electron and gas temperature dependences of the dissociative recombination coefficient

of molecular ions Ar_2^+ with electrons. *Plasma Sources Science and Technology, 20*(5), 055012. doi:10.1088/0963-0252/20/5/055012

33. Lukáč, P., Mikuš, O., Morva, I., Zábudlá, Z., Trnovec, J., Morvová, M., & Hensel, K. (2012). Dependence of the dissociative recombination coefficient of molecular ions Kr_2^+ with electrons on the electron and gas temperatures. *Plasma Sources Science and Technology, 21*(6), 065002. doi:10.1088/0963-0252/21/6/065002

34. Smirnov, B. (2011). *Fundamentals of Ionized Gases: Basic Topics in Plasma Physics*. Erscheinungsort nicht ermittelbar: WILEY-VCH.

35. V.A. Ivanov, Dissociative recombination of molecular ions in an rare gas plasma (Dissotsiativnaya rekombinatsiya molekulyarnykh ionov v plazme inertnykh gazov). Uspekhi fizicheskikh nauk 162(1), 35–70 (1992)

36. Cross sections extracted from PROGRAM MAGBOLTZ, VERSION 7.1 JUNE 2004

37. Lieberman, M. A., & Lichtenberg, A. J. (1994). *Principles of plasma discharges and materials processing*. New York: Wiley.

38. Hatsopoulos, G. N., & Gyftopoulos, E. P. (1973). *Thermionic Energy Conversion Volume I: Processes and Devices*. Maple Press.

39. Baksht, F. G., Hansen, L. K., Pikus, G. E., & Mojžes, B. J. (1978). *Thermionic converters and low-temperature plasma*. Springfield - Va.

40. Rasor, N. (1991). Thermionic energy conversion plasmas. *IEEE Transactions on Plasma Science, 19*(6), 1191-1208. doi:10.1109/27.125041

41. Child, C. D. (1911). Discharge From Hot CaO. *Physical Review (Series I), 32*(5), 492-511. doi:10.1103/physrevseriesi.32.492

42. Go, D. B., Haase, J. R., & George, J. (2017). Thermionic energy Conversion in the Twenty-first Century: Advances and Opportunities for Space and Terrestrial Applications. *Frontiers in Mechanical Engineering, 3*(13). doi:10.3389/fmech.2017.00013

43. Waymouth, J. F. (1962). Electrical energy from high-temperature plasmas. *Journal of the Institution of Electrical Engineers, 8*(92), 380-383. doi:10.1049/jiee-3.1962.0216

44. Paramonov, D. V., & El-Genk, M. S. (1996). A review of cesium thermionic converters with developed emitter surfaces. *AIP Conference Proceedings*. doi:10.1063/1.49899

45. Geller, C., Murray, C., Riley, D., Desplat, J., Hansen, L., Hatch, G., . . . Rasor, N. (1996). High Efficiency Thermionics (HET-IV) and Converter Advancement (CAP) programs. Final reports. doi:10.2172/225989

46. Verbeke, J., Randrup, J., & Vogt, R. (2015). Fission Reaction Event Yield Algorithm, FREYA — For event-by-event simulation of fission. *Computer Physics Communications, 191*, 178-202. doi:10.1016/j.cpc.2015.02.002

47. Northcliffe, L., & Schilling, R. (1970). Range and stopping-power tables for heavy ions. *Atomic Data and Nuclear Data Tables, 7*(3-4), 233-463. doi:10.1016/s0092-640x(70)80016-x

48. Ziegler, J. (1980). Electronic Stopping of Ions. In *Handbook of Stopping Cross-Sections for Energetic Ions in All Elements* (pp. 11-12). New York, NY: Pergamon Press.

49. Nguyen, D. H., & Grossman, L. M. (1967). Ionization by Fission Fragments Escaping from a Source Medium. *Nuclear Science and Engineering, 30*(2), 233-241. doi:10.13182/nse67-a17334

50. J.W. Wilson, R.J. DeYoung, Power density in direct nuclear-pumped ^{3}He lasers. J. Appl. Phys. 49(3), 980–988 (1978)

51. Polous, M., Solovyev, D., & Yarygin, V. (2017). A code for 3D calculations of the output characteristics for a single-cell thermionic fuel element of thermionic nuclear power plants for different applications. *Nuclear Energy and Technology, 3*(3), 189-193. doi:10.1016/j.nucet.2017.08.004
    1. F. JAMERSON, "Investigations on the Direct Energy Conversion of Nuclear Fission Energy to Electrical Energy in a Plasma Diode," Report No. 4 of contract Nonr-3109(00), Office of Naval Research (1963).
52. Oskam, H. J., & Mittelstadt, V. R. (1963). Recombination Coefficient of Molecular Rare-Gas Ions. *Physical Review,132*(4), 1445-1454. doi:10.1103/physrev.132.1445
53. Schreckenbach, K., Faust, H. R., Von Feilitzch, F., & Hahn, A. A. (1981). Absolute measurement of the beta spectrum from U-235 fission as a basis for reactor antineutrino experiments. *Physics Letters, 99B*(3). doi:10.1016/0370-2693(81)91120-5
54. Voss, S. (n.d.). Topaz II System Description. *He 4th International Conference and Exposition on Engineering, Construction, and Operations in Space and The Conference and Exposition/Demonstration on Robotics for Challenging Environments*.
55. Tucker, D. S. (2019). CERMETS for Use in Nuclear Thermal Propulsion. *Advances in Composite Materials Development*. doi:10.5772/intechopen.85220
56. Lafferty, J. M. (1951). Boride Cathodes. *Journal of Applied Physics, 22*(3), 299-309. doi:10.1063/1.1699946
57. Ferdiman, G., & Karni, J. (2019). Sustainable thermionic emission in CO2, helium and argon surroundings. *Applied Surface Science, 471*, 803-812. doi:10.1016/j.apsusc.2018.11.186
58. Applied Physics Technologies. (n.d.). Retrieved October 04, 2020, from http://a-p-tech.com/cebix-cathodes.html
59. Kuzanyan, A. S., Harutyunyan, S. R., & Vardanyan, V. O. (2006). Deposition and investigation of lanthanum–cerium hexaboride thin films. *Journal of Solid State Chemistry*. doi:10.1016/j.jssc.2006.01.040
60. Cahill, J. T., & Graeve, O. A. (2019). Hexaborides: A review of structure, synthesis and processing. *Journal of Materials Research and Technology, 8*(6), 6321-6335. doi:10.1016/j.jmrt.2019.09.041
61. Chen, S., & Saxena, S. (1975). Thermal conductivity of argon in the temperature range 350 to 2500 K. *Molecular Physics,29*(2), 455-466. doi:10.1080/00268977500100391
62. Habedank, O. (1993). Analysis of TOPAZ II and SPACE-R space nuclear power plants using a modified thermionic model. doi:10.2172/307936
63. Godyak, V. A. (2011). Electrical and plasma parameters of ICP with high coupling efficiency. *Plasma Sources Science and Technology, 20*(2), 025004. doi:10.1088/0963-0252/20/2/025004
64. Harris, L. P. (1965). Ionization and Recombination in Cesium-Seeded Plasmas near Thermal Equilibrium. *Journal of Applied Physics, 36*(5), 1543-1553. doi:10.1063/1.1703084
65. HOME. (n.d.). Retrieved October 08, 2020, from https://www.mooseframework.org/
66. Falk, K. (2018). Experimental methods for warm dense matter research. *High Power Laser Science and Engineering, 6*. doi:10.1017/hpl.2018.53
67. Zylstra, A., Frenje, J., Grabowski, P., Li, C., Collins, G., Fitzsimmons, P., . . . Petrasso, R. (2015). Measurement of Charged-Particle Stopping in Warm Dense Plasma. *Physical Review Letters, 114*(21). doi:10.1103/physrevlett.114.215002

68. List of fusion experiments. (2020, October 06). Retrieved October 08, 2020, from https://en.wikipedia.org/wiki/List_of_fusion_experiments

69. Zhong, W., & Shouzhi, Z. (n.d.). A Review of Technology Development of Thermionic Energy Conversion for Space Application. *Journal of Committee of Deep Space Exploration Technology, Chinese Society of Astronautics(CDSET-CSA)*. doi:10.15982/j.issn.2095-7777.2020.20200114001